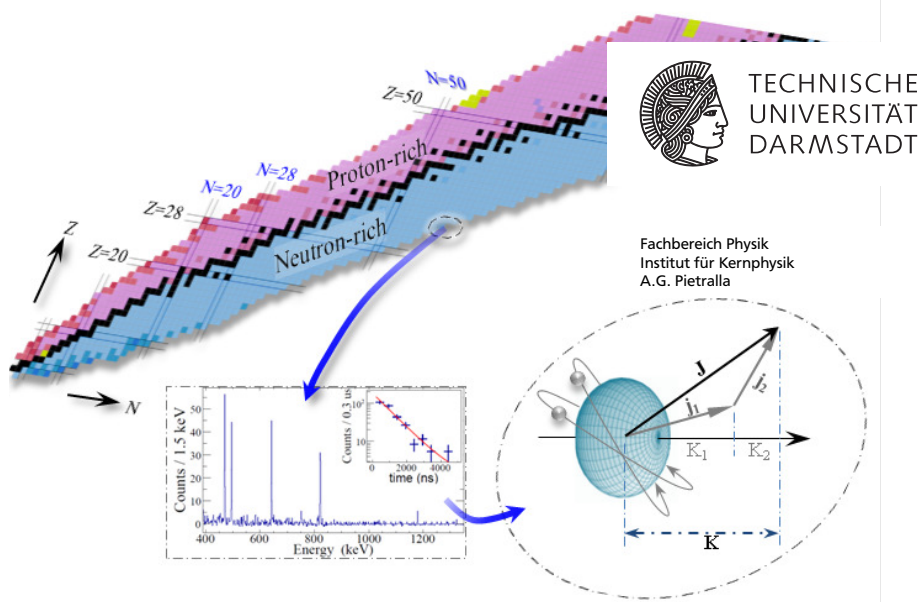


# $\gamma$ -ray spectroscopy of $^{92,94}\text{Se}$ isomeric decay

Zur Erlangung des Grades eines Doktors der Naturwissenschaften (Dr. rer. nat.)  
genehmigte Dissertation von Cesar Yesid Lizarazo Sabogal aus Bogotá,  
Colombia

Tag der Einreichung: 17.01.2018, Tag der Prüfung: 05.02.2018  
2018 Darmstadt – D 17

1. Gutachten: Prof. Dr. Dr.h.c. Norbert Pietralla
2. Gutachten: Prof. Dr. Joachim Enders



# $\gamma$ -ray spectroscopy of $^{92,94}\text{Se}$ isomeric decay

Genehmigte Dissertation von Cesar Yesid Lizarazo Sabogal aus Bogotá, Colombia

1. Gutachten: Prof. Dr. Dr.h.c. Norbert Pietralla
2. Gutachten: Prof. Dr. Joachim Enders

Tag der Einreichung: 17.01.2018

Tag der Prüfung: 05.02.2018

Darmstadt – D 17

Bitte zitieren Sie dieses Dokument als:

URN: urn:nbn:de:tuda-tuprints-72660

URL: <http://tuprints.ulb.tu-darmstadt.de/7266>

Dieses Dokument wird bereitgestellt von tuprints,  
E-Publishing-Service der TU Darmstadt  
<http://tuprints.ulb.tu-darmstadt.de>  
[tuprints@ulb.tu-darmstadt.de](mailto:tuprints@ulb.tu-darmstadt.de)



Die Veröffentlichung steht unter folgender Creative Commons Lizenz:  
Namensnennung – Keine kommerzielle Nutzung – Keine Bearbeitung 4.0 International  
<http://creativecommons.org/licenses/by-nc-nd/4.0/>

---

---

$\gamma$ -ray spectroscopy of  $^{92,94}\text{Se}$  isomeric decay

Vom Fachbereich Physik  
der Technischen Universität Darmstadt

zur Erlangung des Grades  
eines Doktors der Naturwissenschaften (Dr.rer.nat.)

genehmigte Dissertation von  
Magister en Ciencias - Física (M.Sc) Cesar Yesid Lizarazo Sabogal  
aus Bogotá - Kolumbien

Referenten: Prof. Dr. Dr. h.c. Norbert Pietralla  
Korreferenten: Prof. Dr. Joachim Enders

Tag der Einreichnung: 17.01.2018  
Tag der Prüfung: 05.02.2018

Darmstadt  
D17

---



---

# Erklärung zur Dissertation

Hiermit versichere ich, die vorliegende Dissertation ohne Hilfe Dritter nur mit den angegebenen Quellen und Hilfsmitteln angefertigt zu haben. Alle Stellen, die aus Quellen entnommen wurden, sind als solche kenntlich gemacht. Diese Arbeit hat in gleicher oder ähnlicher Form noch keiner Prüfungsbehörde vorgelegen.

Darmstadt, den 16.01.2018

---

(Cesar Yesid Lizarazo Sabogal)

---



*A mi padre, quien me dio la cabeza.  
A mi madre, quien me dio el corazón.*

---



---

## Acknowledgements

---

I would like to express my gratitude to each person and experience that helped on my way during these last four years.

All my gratitude to my supervisor, Professor Norbert Pietralla, for sharing his passion and talent towards physics almost on every occasion I met him. Thank you very much for your clear feedback on my research activities, which was of much help. Additionally, I must thank your always prompt help regarding all my *Ausländerbehörde* issues.

I am very grateful to Dr. Volker Werner for his contribution on the whole development of this work, and for the really nice explanations and discussions introducing me to interesting things of nuclear physics research.

Many thanks to Dr. Jürgen Gerl for giving me the opportunity to conduct this PhD and participating in different projects of a large scale facility such as GSI. Thanks for the positive mood and the interesting conversations about research and life in general.

I am very grateful to Dr. Pär-Anders Södeström (better known as P.-A.) for his help and contributions along the whole work, especially for his guidance and explanations on isomeric states. I enjoyed very much working together and learning from you.

I would like to thank Henning Schafnner for sharing his expertise on electronics and data adquisition that are so crucial for experimental research, and for giving me proper education über Deutschen Fußball und SV Darmstadt 98. Wir sind Darmstädter!.

I would like to thank Dr. GuangShun Li for his efficient and hands-on working style, I much like it and hope to grasp a bit of it.

I acknowledge to the A.G. Pietralla and the IKP secretaries for the finest working environment to conduct scientific research at IKP and TU Darmstadt.

I acknowledge to the Gamma Spectroscopy group at GSI for their help regarding my activities there.

I acknowledge to the HGS-Hire Graduate School for the lecture weeks and soft-skill courses, as well as the HIC for FAIR and the Bundesministerium für Bildung und Forschung for the finaniciation of this work.

I am very grateful to Marc, Tuğba, Waldemar, Pavlos, and Johannes for the countless talks and the feedback, thank you very much for your help and friendship during our PhD lives. Insbesondere, ich bedanke mich bei Herr Lettmann und Herr Witt für die Geduld und Freundlichkeit, die mich vertrauensvoll gegeben haben, auf deutsch zu reden.

I am grateful to the members of the SEASTAR collaboration for the very nice and collaborative environment that made it very successful.

---

---

I want to thank the friends I made these years for their support during though times and for all the nice memories, which is the reason why I regard this place as my second home. En particular a Lea y Tona por todo lo que han hecho por mí, gracias Blatzi por tus cuidados en el hospital y Tona, neta wey gracias por básicamente todo.

Cómo no agradecer infinitamente a mi familia y grandes amigos de Colombia que tanto apoyo y fuerzas me dan pese a la distancia y el tiempo, ésta no la habría coronado sin ustedes. Los llevo siempre conmigo y pensarlos siempre me ha dado fuerzas y motivación.

---

## Abstract

---

The isomeric decay of  $^{92,94}\text{Se}$  has been studied by means of  $\gamma$ -ray decay spectroscopy, in order to explore the nuclear structure of these very neutron-rich exotic nuclei far way from the ‘stability line’. The experiment was conducted in March 2015 at the Radioactive Ion Beam Factory of the RIKEN Nishina Center (RIBF-RIKEN) located in Japan. A radioactive beam of exotic nuclei was delivered by the BigRIPS fragment separator, tuned to select the desired products of the in-flight fission of a  $^{238}\text{U}$  primary beam on a  $^9\text{Be}$  target. This secondary beam impinged on a liquid Hydrogen ( $\text{LH}_2$ ) target, producing Selenium nuclei via different nucleon knock-out reactions. The final products passed through the ZeroDegree mass spectrometer, where they were identified on an event-by-event basis by means of determination of the proton number ( $Z$ ) and mass-to-charge ratio ( $A/Q$ ), and were finally implanted into a stack of silicon layers of the AIDA detector system. The existence and subsequent decay of isomeric excited states of these nuclei was studied with the EURICA  $\gamma$ -ray HPGe detector placed around the AIDA layers. New spectroscopic information has been obtained for both isotopes, leading to an extension of their level schemes. In particular, the isomeric state of  $^{94}\text{Se}$  has been observed for the first time. The possible causes of isomerism in these nuclei have been discussed and compared with the results, and it has been found that the presence of oblate-deformed quasiparticle states play an important role in the description of the isomerism phenomenon. The level schemes obtained have been compared with the predictions of different state-of-the-art beyond mean-field calculations, which propose all a prolate-to-oblate shape transition with increasing neutron number taking place between  $N=56$  and  $N=60$  ( $^{90,92,94}\text{Se}$ ). Based on the observed structure of the level schemes and the deformation character of the isomeric states, the idea of a shape transition into an oblate structure at  $N=60$  is supported.

---

## Zusammenfassung

---

Der isomere Zerfall der  $^{92,94}\text{Se}$  Kerne wurde durch  $\gamma$ -Zerfallsspektroskopie untersucht, um die Kernstruktur dieser neutronenreichen Isotope fernab des Tals der Stabilität zu erkunden. Das Experiment wurde im März 2015 in der Radioactive Ion Beam Factory des RIKEN Nishina Center (RIBF-RIKEN) in Japan durchgeführt.

Ein radiaktiver Strahl exotischer Kerne wurde vom BigRIPS Fragmentseparator zur Verfügung gestellt. Dieser Strahl wurde optimiert, um die gewünschten Produkte der Spaltung des primären  $^{238}\text{U}$  Strahls an einem  $^9\text{Be}$  Target im Flug zu selektieren.

Dieser sekundäre Strahl traf auf ein flüssiges Wasserstofftarget ( $\text{LH}_2$ ), um Selenkerne durch verschiedene Nukleonen-Knock-Out-Reaktionen zu erzeugen. Die Produkte durchliefen das ZeroDegree Massenspektrometer, in dem sie auf einer Event-by-Event-Basis, durch Bestimmung der Protonenzahl und des Masse-Ladungsverhältnisses, identifiziert und letztendlich in einer Silikonschicht des AIDA-Detektorsystems implantiert wurden. Die Existenz und der anschließende Zerfall der angeregten Isomerzustände dieser Kerne wurde mit dem EURICA HPGe-Detektorarray, der die AIDA-Schichten umgab, untersucht.

Es wurde neue spektroskopische Information für beide Isotope erhalten und dies ermöglichte eine Erweiterung des Levelschemas. Insbesondere wurde der Isomerzustand von  $^{94}\text{Se}$  zum ersten Mal beobachtet.

Die möglichen Ursachen der Isomerie dieser Kerne werden diskutiert und mit den Ergebnissen verglichen. Außerdem wurde beobachtet, dass die Anwesenheit von oblaten, deformierten Quasiteilchenzuständen eine wichtige Rolle in der Beschreibung des isomeren Phänomens spielt.

Die erhaltenen Levelschemata wurden mit Vorhersagen neuster Beyond Mean-Field Rechnungen verglichen, die einen Formübergang von prolat zu oblat mit zunehmender Neutronenzahl zwischen  $N = 56 - 60$  vorschlagen.

Basierend auf der Struktur der beobachteten Levelschemata und dem Deformationscharakter der unstersuchten isomeren Zustände, wird die Hypothese des Formübergangs in eine oblate Struktur bei  $N=60$  unterstützt.



---

## Contents

---

<b>1</b>	<b>Introduction</b>	<b>1</b>
1.1	Motivation . . . . .	5
<b>2</b>	<b>Fundamentals of Nuclear Theory</b>	<b>8</b>
2.1	The nuclear shell model . . . . .	8
2.1.1	Pairing interaction and quasi-particle excitations . . . . .	11
2.2	Nuclear deformation . . . . .	12
2.2.1	Quadrupolar Deformations . . . . .	13
2.3	The Collective model . . . . .	14
2.3.1	Axially symmetric rotors . . . . .	15
2.3.2	Excitations for axially-asymmetric deformations . . . . .	17
2.3.3	Vibrational excitations . . . . .	20
2.4	The Nilsson model . . . . .	21
<b>3</b>	<b>State-of-the-art Beyond-Mean-Field Calculations</b>	<b>24</b>
3.1	Gogny effective interaction . . . . .	25
3.2	Constrained Hartree-Fock Bogoliubov method (CHFB) . . . . .	25
3.3	Generator Coordinates method (GCM) . . . . .	26
3.4	Calculations for neutron-rich Selenium isotopes . . . . .	27
3.4.1	Symmetry-Conserving Configuration-Mixing (SCCM) method	27
3.4.2	5-Dimensional Collective Hamiltonian (5DCH) calculations .	28
3.4.3	Comparison of calculations . . . . .	29
	Potential energy surfaces (PES) . . . . .	29
	Nilsson diagrams . . . . .	29
<b>4</b>	<b>Fundamentals of <math>\gamma</math>-ray spectroscopy</b>	<b>33</b>
4.1	Half-life and branching ratio . . . . .	33
4.2	Electromagnetic decay of excited states . . . . .	34
4.2.1	Kinematics of $\gamma$ -ray emission . . . . .	34
4.2.2	Multipole expansion . . . . .	35
4.2.3	Decay rate and transition probability . . . . .	36
4.2.4	Weisskopf estimates . . . . .	38
4.2.5	Internal Conversion . . . . .	40
4.3	Nuclear Isomerism . . . . .	41
4.3.1	Spin-traps . . . . .	42
4.3.2	Shape isomers . . . . .	42
4.3.3	Seniority isomers . . . . .	42

4.3.4	<i>K</i> -traps	44
4.4	Interaction of $\gamma$ -rays with matter	47
<b>5</b>	<b>Experiment setup</b>	<b>50</b>
5.1	Production of radioactive ion beams (RIB)	52
5.1.1	RIKEN accelerator complex	52
5.1.2	In-flight fission of $^{238}\text{U}$	53
5.2	BigRIPS: Selection and identification of fission fragments	54
5.3	ZeroDegree spectrometer	56
5.4	Beam-line detectors for tracking and particle identification	57
5.5	DALI2 & MINOS: In-beam $\gamma$ -spectroscopy of knockout reactions	60
5.6	EURICA & AIDA: $\gamma$ -ray decay spectroscopy	61
<b>6</b>	<b>Data Analysis</b>	<b>64</b>
6.1	Zero Degree Particle identification	64
6.1.1	Atomic number determination	64
6.1.2	Mass-to-Charge ratio determination	65
6.1.3	Improvement of the Particle IDentification (PID)	67
6.2	Analysis of $\gamma$ -rays with EURICA	70
6.2.1	Energy calibration	70
6.2.2	Time-walk correction	74
6.2.3	Addback	74
6.2.4	Detection efficiency	75
6.2.5	Background and selection of isomeric $\gamma$ -rays	77
6.2.6	$\gamma\gamma$ coincidences	78
<b>7</b>	<b>Results</b>	<b>82</b>
7.1	Conditions for selection of delayed $\gamma$ -rays	82
7.2	$^{92}\text{Se}$	83
7.2.1	Preliminary identification of isomeric transitions	83
7.2.2	Spectra of $\gamma\gamma$ coincidences	85
7.2.3	Half-life measurement	88
7.2.4	Singles intensities	89
7.2.5	Level Scheme	94
7.3	$^{94}\text{Se}$	100
7.3.1	Identification of isomeric transitions	100
7.3.2	Spectra of $\gamma\gamma$ coincidences	100
7.3.3	Half-life measurement	102
7.3.4	Singles intensities	105
7.3.5	Level Scheme	107

---

---

<b>8 Discussion</b>	<b>111</b>
8.1 Origin of the isomeric states . . . . .	111
8.2 Comparison of excitation energies with BMF calculations . . . . .	114
8.3 Shape evolution around N=58 . . . . .	118
<b>9 Conclusions and remarks</b>	<b>121</b>
<b>A Error propagation of relevant quantities</b>	<b>I</b>
A.1 Error of singles intensities . . . . .	II
A.2 Error of relative intensities . . . . .	III
<b>B Results of in-beam spectroscopy of <math>^{92,94}\text{Se}</math> - SEASTAR 2015</b>	<b>IV</b>
<b>Bibliography</b>	<b>V</b>
<b>Scientific Production during Doctoral studies</b>	<b>XIV</b>
<b>Personal Information</b>	<b>XVI</b>



---

## 1 Introduction

---

The understanding of nature at scales much smaller than the typical atomic distances ( $< 10^{-12}\text{m}$ ) has shaped and challenged the human perception of the universe at all scales of space and time, from processes in the early universe to the astrophysical events that regulate abundance of the chemical elements in the observable universe. Simultaneously, countless applications have been derived from this scientific activity in varied fields such as medicine, energy, security or industry, pushing forward the technology and, ultimately, the quality of life of modern societies.

Subatomic physics, developed mainly in the last 130 years, started with the discovery of the electron by Thomson in 1887 [1]. Early in the twentieth century, the experiments of Rutherford, Chadwick, and others helped to clarify the existence of the *atomic nucleus* [2], a system inside the atom containing most of its mass and composed by two types of particles, protons and neutrons, confined in a scale of just about  $10^{-15}\text{ m}$ . It was understood sooner that the chemical elements, such as carbon, oxygen or hydrogen, are defined by the number of protons in their nuclei. Variants within each element, with a different number of neutrons, were also discovered and are nowadays known as isotopes. These nuclei of the same element have the same chemical properties but different masses and different nuclear properties [3].

A systematic representation of all the known nuclei is presented in the *nuclide chart*, a two-dimensional plot in which one axis corresponds to the number of neutrons ( $N$ ) and the other to the number of protons ( $Z$ ) in an atomic nucleus, see Figure 1.1. The stable isotopes, those which do not transmute into a nucleus with a different ( $N, Z$ ) combination, define the ‘valley of stability’, a group of 288 nuclides covering most of the chemical elements [4, 5]. The unstable nuclei are characterized by an unbalanced  $N/Z$  ratio, and are found by moving away from the valley of stability, defining the ‘proton-rich’ and ‘neutron-rich’ regions. Most of these nuclides do not exist on Earth, as they have half-lives in time scales often so short that in some hours (or much less) they have transmuted into stable nuclei.

The initial nuclear models -such as the liquid drop model proposed by Gamow in 1935 [6]- were created from empirical data to explain the general trends of nuclear properties such as the mass or binding energy of a large set of nuclei of different elements, but did not shed light on the internal nuclear dynamics and structure. Sooner, experimental evidence was collected of nuclei with some precise values of protons or neutrons presenting a particularly high nucleon separation energy (relative to the neighboring even-even isotope). Moreover, the systematics of other nuclear properties of nuclei accessible at that time (mainly excitation energies,

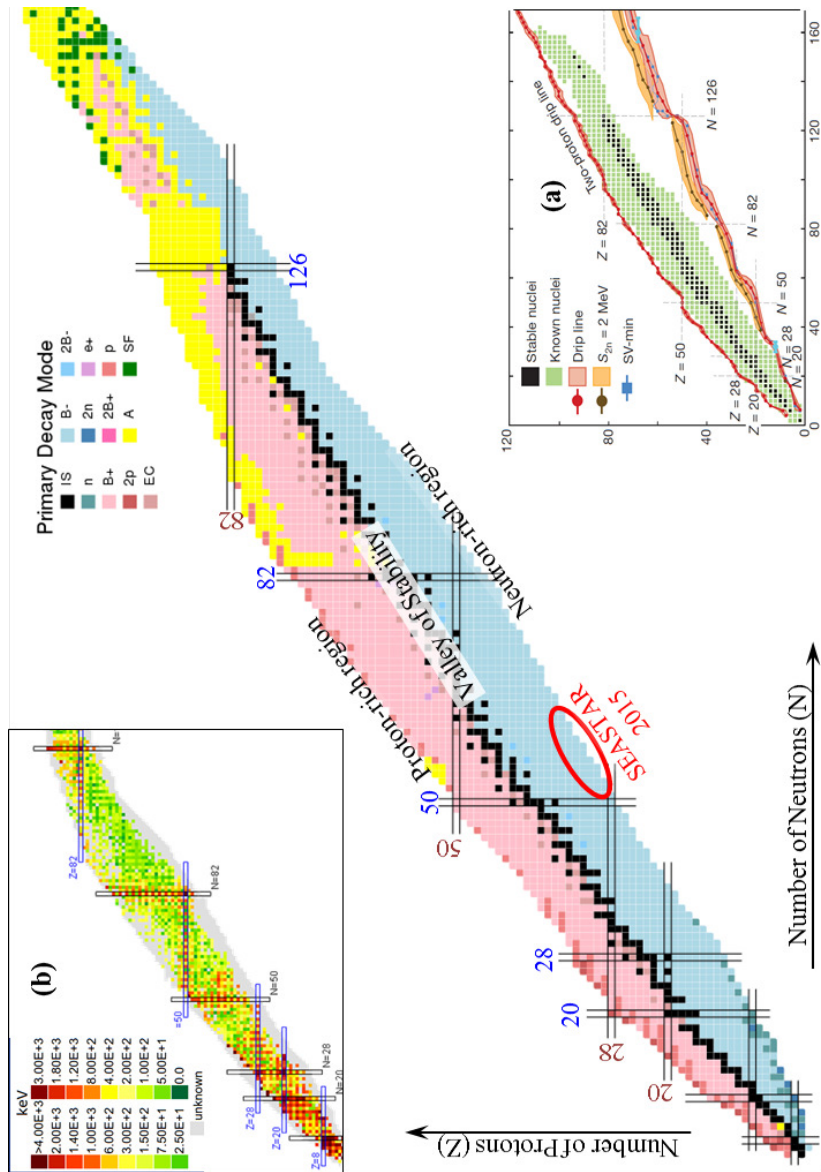


**Figure 1.1:** Chart of nuclides, depicted by the primary decay mode [7]. (a) Nuclear landscape up to 2012. Notice the vast amount of neutron-rich nuclei not yet studied. Source [5]. (b) Excitation energy of the first excited state. Notice the large values at  $(N, Z)$  positions close to magic numbers [4].

---

---

spin, magnetic moments,  $\beta$ -decay), also presented special behaviours for these specific numbers of nucleons (see Figure 1.1), so that all these observations gave rise to the idea of a nuclear shell structure [8], in analogy to the atomic physics case.

An adequate theoretical description was introduced in 1949 by Mayer, but also independently by Jensen and collaborators [9, 10], for which they received jointly the Nobel prize in 1963. Commonly referred as the *independent particle* shell model, it postulates that the nucleon-nucleon interaction can be replaced, to first order, by an effective (spherical) central potential in which the nucleons are immersed and move independently from each other. The inclusion of a spin-orbit interaction, combined with the Pauli exclusion principle, allowed to reproduce the large gaps of single-particle energies (SPE) for nuclei with 2,8,20,50, 82 and 126 proton or neutron numbers, and explaining much of the special properties observed for these nuclei with *magic numbers* of nucleons.

In the decade of the fifties, a new type of nuclear excitation was discovered where not one but several nucleons contribute coherently to the excitation. Different types of *collective motion* were found to be related to specific types of *nuclear deformation*, a term used to refer the deviation of the nuclear shape with respect to a spherical one. Maybe the most remarkable of these excitation modes observed were the harmonic-vibrator spectra of spherical nuclei (such as  $^{118}\text{Cd}$ ), as well as the rotational spectra of axially (symmetric and asymmetric) deformed nuclei (such as the Hf, Sm stable nuclides). Furthermore, it was realized that the deformation and collectivity were not exclusive of nuclei with random number of nucleons, but they develop more or less gradually as a function of the neutron or proton number: From non-deformed shapes for nuclei close to the shell closures to very deformed shapes for nuclei in mid-shell regions [11].

The very different behaviour of the single-particle and the collective motions made it difficult to relate to each other. However, in 1955 the model of Nilsson [12] of a single-particle in a deformed mean-field that can couple to intrinsic rotational states, paved a new perspective to understand nuclei from a microscopic/macroscopic point of view. The addition of pairing, fundamental to understand not only the extra-binding of even-even nuclei and their  $J = 0$  ground-state angular momentum, but also nuclear superfluidity, led to an ‘unified model’, an extensive work for which A. N. Bohr, Mottelson and Rainwater were awarded jointly the Nobel prize in 1975: “For the discovery of the connection between collective motion and particle motion in atomic nuclei and the development of theory of the structure of the atomic nucleus based on this connection”.

Despite the tremendous progress in understanding the nuclear dynamics, most of the available spectroscopic data were limited either to the stable nuclides or the unstable ones close to the valley of stability. The idea that the shell structure

-and so the magic numbers- remains static for very exotic nuclei, with a largely unbalanced  $N/Z$  ratio, was cast in doubt both from theoretical and experimental sides. On the one hand, it was pointed out that the accumulation of effects due to the ‘residual’ part of the nucleon-nucleon interaction can change the relative location of the single particle energies [13, 14], leading to a reduction of the gaps at the magic numbers. On the other hand, cases such as the ground-state spin of  $^{11}\text{Be}$  [15], or the appearance of deformed shapes in neutron-rich  $N = 20$  nuclei such as  $^{32}_{12}\text{Mg}_{20}$  [16] revealed a re-arrangement of the single particle orbitals as a function of the nucleon number. Naturally, the question of *how the nuclear structure evolves in the exotic regions of the nuclear chart* became one of the main pillars of nuclear structure research [8, 11, 13, 14].

The technological developments occurring steadily since the decade of the seventies allowed the production and exploitation of exotic nuclei in forms of Radioactive Ion Beams (RIB). A better comprehension of the reaction mechanisms that produce nuclei in specific regions of the nuclear chart inspired the design and construction of facilities with larger accelerators and powerful magnetic spectrometers allowing to synthesize and identify exotic nuclei with a production efficiency and mass-resolution good enough for the execution of spectroscopic experiments. Two RIB production methods were developed and are currently widely used, namely: the Isotope Separation On-Line technique (ISOL), and the in-flight fission technique [17]. They are employed by the large-scale facilities that have pioneered different aspects of the RIB research, such as ISOLDE at CERN (Switzerland), GSI (Germany), MSU (USA), GANIL (France), and RIKEN (Japan).

Simultaneous to the development in the production of exotic nuclei, the detectors used for spectroscopy improved tremendously increasing their sensitivity to the radiation emitted by the nuclei. Significant progress in the detection of  $\gamma$ -rays following nuclear reactions enabled extracting physical information of experiments with low-intensity beams [11]. In particular, the development of ‘large arrays’ of detectors with digital data acquisition covering a large fraction of the solid angle of the reaction point, improved critical properties such the efficiency, high-counting rates, and high-granularity to localize individual  $\gamma$ -rays. Besides, the advent of semiconductor detectors offering a high-energy resolution, such as the high-purity Germanium detectors, led to the construction of powerful arrays such as Gamma-sphere [18] or Euroball [19], that continue producing some of the most relevant nuclear structure physics results after 20 years of operation. The more recent detector break-through corresponds to the development of the AGATA and GRETA arrays in Europe and the USA, respectively, designed as  $4\pi$  spheres of germanium detectors employing the technique of  $\gamma$ -ray tracking [20] which allow to reconstruct the interaction point of the  $\gamma$ -ray inside the detector volume, opening new physics possibilities for the field.

---

## 1.1 Motivation

---

For the most neutron-rich isotopes -so far produced- of Ge ( $Z = 32$ ), Se ( $Z = 34$ ), and Kr ( $Z = 36$ ), few or no spectroscopy data had been measured before 2015. They are localized in the region of the nuclide chart defined by  $N \geq 50$  and  $28 \leq Z \leq 40$  (see Figure 1.2), which has been of interest during the last decades for the nuclear structure field since there it is unknown the evolution of the collectivity and deformation after the neutron shell closure at  $N=50$  and above the proton shell closure at  $Z=28$ . These mid-mass nuclei were the focus of the 2015 experimental campaign of the SEASTAR scientific program [21], a project consisting on the systematic search for new spectroscopy in the wide range of the neutron-rich nuclei accessible with the Radioactive Ion Beam Factory (RIBF) of the RIKEN Nishina center located in Japan [22], one of the world leading RIB facilities that currently produces the strongest beams on this exotic mass region. Some of the results from the campaign have been already published, see Refs. [23–26].

The systematics of the  $2_1^+$  excitations energies, the  $B(E2; 2_1^+ \rightarrow 0^+)$  decay strengths<sup>1</sup>, and the  $R_{4/2} = E(4_1^+)/E(2_1^+)$  ratios reported to date for the region are shown in Figure 1.2. The recent measurements of the  $2_1^+$  and the corresponding  $B(E2 \downarrow)$  strengths for the  $N=50$  isotones revealed that indeed a shell closure occurs -at least- down to  $^{80}_{30}\text{Zn}$  [28, 29]. Beyond the shell closure ( $N > 50$ ), the trends of the Sr ( $Z = 38$ ) and Zr ( $Z = 40$ ) isotopes present a strong decrease (increase) of the energy (decay strength) from  $N=56$  to  $N=60$ . The Zr isotopes have a spherical ground-state up to  $N=56$  and suddenly become highly deformed at  $N=60$ , as it can be seen on the  $R_{4/2}$  ratios. This systematic stands as one the most drastic ground-state shape transition observed so far within the span of just few nucleons [30, 31].

In 2016, the decay strengths between low-lying states of  $^{96}\text{Zr}$  were extracted by means of a model-independent approach in an experiment conducted at the S-DALINAC at T.U. Darmstadt [32]. The good quantitative agreement of that study with recent Large-scale Monte Carlo shell-modell calculations [33], provides evidence that observed shape transition is caused by the coexistence of two different structures (deformed and spherical) almost not interacting with each other. The calculations provide a microscopic description on the formation of both coexisting structures: For the isotopes with  $N \leq 58$  the deformed low-lying  $0_2^+$  state is caused by proton excitations from the  $fp$  (sub) shell promoted to the  $g_{9/2}$  orbital coupled to a neutron excitation from the  $d_{5/2}$  orbital promoted to orbitals of the  $sdg$  shell. The increase in the occupation of different orbitals enhances the effect of the monopole

---

<sup>1</sup> For  $^{98}\text{Zr}$ , the decay strength  $B(E2 \downarrow)$  is not known, but a maximum upper limit [27], which is used in this plot.

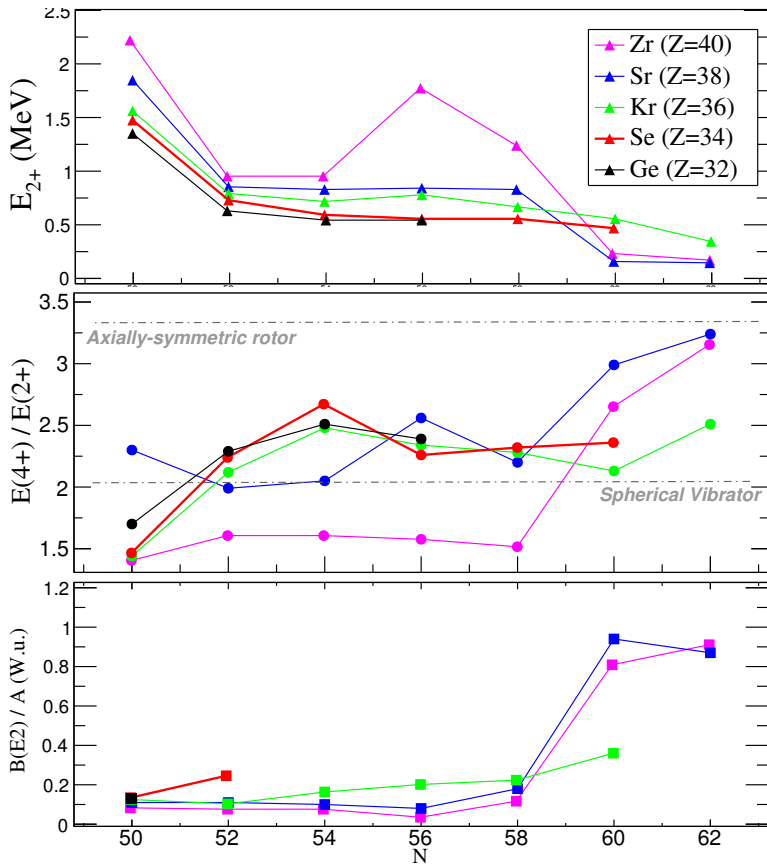


**Figure 1.2:** Systematics of  $E(2_1^+)$  excitation energy,  $R_{4/2} = E(4_1^+)/E(2_1^+)$  ratio, and  $B(E2; 2_1^+ \rightarrow 0^+)/A$  decay strength for the nuclei in the region of the nuclide chart defined by  $N \geq 50$  and  $28 \leq Z \leq 40$ , focus of the SEASTAR 2015 experimental campaign.

part of the *tensor force* [34] which re-arranges the relative positioning of the SPE levels, in a mechanism known as ‘Type-II shell evolution’.

In contrast, the  $2_1^+$  and  $R_{4/2}$  trends of  $Z \leq 36$  (Ge, Se and Kr isotopic chains) show a very different behaviour: The excitation energy decreases gradually up to  $N=60$ . The  $R_{4/2}$  ratios increase from values  $< 2$  at  $N=50$ , to  $\sim 2.5$  at  $N=54$ , and decrease smoothly afterwards up to  $N=60$  showing that the sub-shell closure around  $N=56$  plays little influence in these isotopes [23, 24, 35–37]. For  $^{86-92}\text{Se}_{52-58}$  and the neighbouring  $^{84-88}\text{Ge}_{52-56}$  the lowest non-yrast levels were also identified, and it was noticed that the proposed  $2_2^+$  states are rather lower than the  $4_1^+$ . This fact combined with the  $R_{4/2}$  values around 2.5 provide an experimental signature of

quadrupolar deformation in the  $\gamma$ -degree of freedom [11]. The data has been compared to the predictions obtained from different state-of-the-art Gogny beyond mean-field calculations [31, 38], revealing that the deformation in this region is characterized by ‘ $\gamma$ -softness’, so the deformation is not rigid with respect to axial-symmetric deformations, and even experimental evidence of triaxiality was found in the case of  $^{86}\text{Ge}$  [23]. From the shell model point of view, the fact that the strong shape transition at  $N = 60$  also occurs for Sr but not for Kr or Se, could result from a too small occupation of the  $\pi g_{9/2}$  orbital to trigger both the proton-neutron correlations and consequently the large deformation for  $Z \geq 38$  [37].

Additional calculations predict different shape transitions for  $Z=34$  around  $N \sim 60$  [24, 39–41]. All of them point interestingly to an oblate ground-state deformation for  $^{94}\text{Se}$  and a prolate-oblate shape-coexistence situation in the neighbouring even-even isotopes. However, the current experimental information (see Appendix B) is not sufficient to test the predictions since the  $R_{4/2} \sim 2.4$  corresponds to a transitional value between the spherical and rigid rotor limits, and a shape transition can undergo without a sharp change of  $R_{4/2}$  values, as it occurs in the well-known case of prolate-oblate shape coexistence in  $^{68,70,72}\text{Se}$  [42–45]. For this reason, more data is needed to clarify the evolution of the deformation, providing a consistent picture from  $Z=40$  up to  $Z=34$  along  $N \sim 60$  isotones, and from  $N=50$  to  $N \geq 60$  along the  $Z=34$  isotopes. This is the central motivation of the present thesis.

This document is organized as follows: In Chapter 2, the fundamental concepts of nuclear structure relevant for the discussion are introduced. In Chapter 3 is presented the description of the methods used in the state-of-the-art beyond-mean-field calculations on the nuclei analyzed. In Chapter 4, the fundamental concepts of the electromagnetic decay of the nucleus are discussed, with emphasis in  $\gamma$ -ray emission. Nuclear isomerism is also presented, since it is the experimental process studied in this thesis. In Chapter 5, the experimental setup and the techniques used to study  $^{92,94}\text{Se}$  are discussed. In Chapter 6, the general steps of the data analysis conducted to identify the nuclei and their associated deexcitation radiation are described. The results obtained are presented in Chapter 7, and discussed afterwards in Chapter 8. Finally, the conclusions and remarks of the present work are mentioned in Chapter 9.

---

## 2 Fundamentals of Nuclear Theory

---

The theoretical description of the nucleus is a many-body problem of a finite system of fermions interacting via the Coulomb and Nuclear Force. While the former is very well known, the latter is an interaction whose universal expression valid across the whole nuclide chart has not yet been developed due to its inherent complexity.

The most fundamental solution of the atomic nucleus would be to use the quantum-chromodynamics to model the strong interaction of the most basic degrees of freedom in the nucleus: quark and gluons. This description is still far to be applied for the most of the nuclei, however, there are very good progress in describing light and mid-mass nuclei with internucleon forces that are inspired by QCD symmetries constrained to experimental data [46]. These ab-initio calculations are still far from the exotic mass region of the present thesis.

Currently, calculations of the nuclear dynamics under an unique theoretical model are possible only for partial regions along the nuclide chart. A description valid over a wide range of nuclei is very challenging not only because of the high computing power rapidly increasing with the number of nucleons, but also because it has to consider the many peculiarities of the nuclear dynamics that manifest in different mass regimes. For instance, the characteristic nuclear excitation modes change drastically for different specific  $(Z, N)$  combination of nucleons, and are not easily reproduced by an unique framework. Moreover, nuclear observables such as the excitation energy spectrum, the binding energy, or nuclear mass, have very different energy scales, from few keV to hundreds of MeV. Hence, a model representing fairly enough the interactions as well as very accurate calculation methods are both needed to have trustworthy predictive power over such different regimes.

Despite the complexities stressed above, the systematics of much of the experimental data measured so far can be understood with rather clear physical concepts, some of them already introduced in Chapter 1. In this chapter, the general ideas behind the single particle and collective models of the nuclei are discussed, as well as the concept of nuclear deformation (Sections 2.1-2.3). The Nilsson model, a single-particle model for deformed nuclei that also allows collective excitations is discussed afterwards, (Section 2.4).

---

### 2.1 The nuclear shell model

---

In a very general manner, the Hamiltonian of a nucleus with  $A$  particles can be expressed as

$$H = T + V = \sum_{i=1}^A \frac{\vec{p}_i^2}{2m_i} + \sum_{i>k=1}^A V_{ik}(\vec{r}_i - \vec{r}_k), \quad (1)$$

where the interaction  $V_{ik}$  is -in a first approximation- considered as a two-body nucleon-nucleon potential. An exact solution of this problem is cumbersome not only due to the complexity of the interaction involved but also due to the large amount of degrees of freedom involved. Instead, a mean-field approach is adopted, so that the interaction is replaced by an average potential  $U(\vec{r})$  caused by the nucleons themselves, so the Hamiltonian can be re-expressed as

$$H = \underbrace{\sum_{i=1}^A \left( \frac{\vec{p}_i^2}{2m_i} + U_i(\vec{r}) \right)}_{\equiv H_0} + \underbrace{\left\{ \sum_{i>k=1}^A V_{ik}(\vec{r}_i - \vec{r}_k) - \sum_{i=1}^A U_i(\vec{r}) \right\}}_{\equiv H_{res}}, \quad (2)$$

with  $H_0$  the single-particle Hamiltonian, and  $H_{res}$  the residual effects of the interaction. Though  $H_{res}$  is not necessarily small, especially in very deformed nuclei, it can be solved through perturbative methods using the solutions of  $H_0$ . The idea of a nuclear shell model based on a spherical mean-field potential already existed around 1920 but the first one to be really successful was the *independent particle model* of Mayer and Jensen and collaborators [8–10]. They proposed to modify the potential as a surface-corrected isotropic harmonic oscillator plus a strong attractive spin-orbit interaction,

$$U(\vec{r}) = \frac{1}{2} \hbar \omega r^2 + D \vec{l}^2 - C \vec{l} \cdot \vec{s}, \quad (3)$$

together with a small residual  $H_{res}$  term so that the particles move almost independent of each other, except for the Pauli exclusion of fermions. In this manner, the wave function of the nuclear ground state corresponds to the product of the Slater determinant for the protons and the one for neutrons, obtained by filling the lowest energy levels (known as *orbits*). As a consequence of the central character of the potential, the wave function is separable in the angular and radial coordinates, with the former given by the Spherical Harmonics, which have defined orbital angular momentum  $l$  and magnetic sub-states  $m$ . The effective potential given by a harmonic oscillator corrected by a ‘surf’ term proportional to  $\vec{l}^2$  (the correction term bounds more the high- $l$  orbitals, which are in average closer to the surface), is a better description of the approximate constant character of a realistic potential inside the nuclear volume compared to a bare harmonic oscillator, and also breaks the degeneracy of the major shell number  $N = 2(n-1) + l$  into sub-levels of defined orbital angular momentum and principal quantum number;  $l, n$ , respectively. The total angular momentum number is given by the coupling  $\vec{j} = \vec{l} + \vec{s}$ , so that the corresponding quantum number  $j = l \pm 1/2$ . The proposed spin-orbit interaction favours the parallel alignment  $l + 1/2$  over the  $l - 1/2$ , breaking in this way the degeneracy of the orbital-angular momentum levels, resulting into final single

particle energies characterized by  $n$ ,  $l$ , and  $j$ . The single particle energies of this potential are shown in Figure 2.1.

Notice that the parity  $\pi = (-1)^l$  of the orbitals in a shell tend to be the same, with the exception of one level with opposite parity lying high in the shell, namely, the  $1g_{9/2}$  in the 28-50 shell, or the  $1h_{11/2}$  in the 50-82 shell. Also, a subshell at nucleon numbers 40, 56, or 64 may appear depending on the specific values of the parameters. These subshells are indeed important: For example, as it was mentioned in the motivation, the Zr isotopic chain ( $Z=40$ ) behaves as a shell closure from  $N=50$  to  $N=56$  with  $^{96}_{40}\text{Zr}_{56}$ , or  $^{146}_{64}\text{Gd}_{82}$  exhibiting features of doubly magic nuclei.

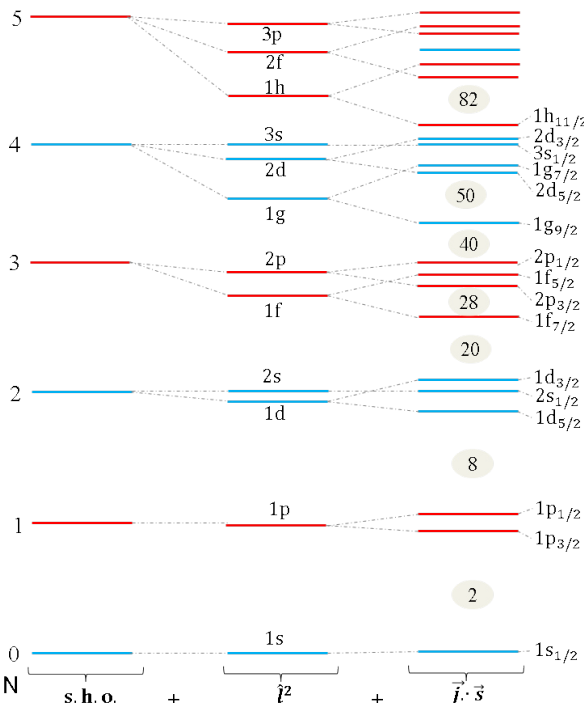


**Figure 2.1:** From Source [11]. Single-particle energies for a harmonic oscillator (left), plus a  $\vec{l}^2$  correction (middle), and a potential considering spin-orbit interaction (right). The maximum number of particles in certain level is given by  $2j + 1$ , a consequence of the Pauli exclusion. For some values of a total number of particles (shown in circles), the energy gap with the immediate next high level is considerable large, giving rise to the shell structure and the magic numbers. Levels with positive (negative) parity are indicated in blue (red).

The strict validity of this model may be limited to closed shells (and single-particle -or hole- states built on them), but it provides a framework for more complex situations mainly because of two reasons: First, its solutions are often used as the basis of more complex calculations since the harmonic-oscillators solution offer a basis with good quantum numbers well defined. Second, the eigenfunctions of a many-body problem are represented as a linear combination of the single particle solutions [8].

### 2.1.1 Pairing interaction and quasi-particle excitations

The pairing interaction is one of the most important ‘residual’ interactions in all the models considered so far. The most clear evidence of its existence corresponds to the behaviour of the nucleon separation energies along an isotopic chain: For even masses it is considerably higher than the adjacent odd ones [4]. Moreover, in even-even nuclei not only this extra-binding energy is the highest, but also the ground state is always  $J^\pi=0$ . This suggests that there must be an interaction that favours the coupling of nucleons in pairs, with the peculiarity that for two identical nucleons in the same  $j$ -orbit, the favoured coupling is  $\vec{j}_1 + \vec{j}_2 = 0$ . Formally, the interaction is defined by [11]:

$$\langle j_1 j_2 J | V_{pair} | j_3 j_4 J' \rangle = -G \sqrt{(j_1 + \frac{1}{2})(j_3 + \frac{1}{2})} \delta_{j_1 j_2} \delta_{j_3 j_4} \delta_{J0J'0}, \quad (4)$$

where  $G$  is the strength of the pairing force. The effect is quite clear: only pairs of identical particles in the same orbital  $j_1 = j_2$  and coupled to  $J=0$  are affected by this interaction (e.g. antiparallel coupling). The ‘scattering’ of the coupled pair to a different orbit is possible, as long as it still satisfies  $\vec{j}_3 + \vec{j}_4 = J' = 0$ .

In the discussion of pairing, the so called gap parameter is defined in terms of a sum over orbits  $i, j$  as

$$\Delta = G \sum_{i,j} U_i V_j, \quad (5)$$

with  $U_i$  ( $V_j$ ) the occupation (emptiness) factors of the orbits, so  $V_k^2 + U_k^2 = 1$ . The effect of the Pairing interaction is to generate a smooth distribution of occupancy in the orbitals near the nucleus Fermi surface  $\epsilon_F$ , over an energy range  $\Delta$  [11]. Without pairing, the Fermi surface would be simply the last orbital / level filled, and  $\epsilon_i - \epsilon_F$  would be the energy needed to excite one of the last nucleons into the orbit  $\epsilon_i$  above the Fermi level. Due to Pairing, the excitation energy of a *quasi-particle* in the level  $i$  is given by

$$E_i = \sqrt{(\epsilon_i - \epsilon_F)^2 + \Delta^2}. \quad (6)$$

For the cases when  $\epsilon_i \sim \epsilon_F$  then  $E_i \sim \Delta$ , establishing a minimum value for  $E_i$ . However, that is not the minimum energy of an excited state. The pairing causes

the occupation to be distributed over several levels, above and below the Fermi surface so the excitation can come from any of the quasiparticles in this partially occupied levels, with energy  $\epsilon_0$ . Thus, in odd mass nuclei the lowest quasiparticle excitation energy is obtained subtracting the quasi-particle energy of the ground state to the quasi-particle energy the level  $i$  on top:

$$E_{exc}^i = E_i - E_s = \sqrt{(\epsilon_i - \epsilon_F)^2 + \Delta^2} - \sqrt{(\epsilon_0 - \epsilon_F)^2 + \Delta^2}, \quad (7)$$

where  $E_0$  is the quasi-particle energy of the closest level ( $\epsilon_0$ ) to the Fermi surface ( $\epsilon_F$ ). Therefore  $E_{exc}^i$  can be very small, considering that both  $E_i$  and  $E_0 \sim \Delta$  for levels sufficiently close to the Fermi level, such that  $\epsilon_i - \epsilon_F \ll \Delta$ .

In contrast, for even mass nuclei the pairing establishes a minimum value for quasi-particle excitations. To create such an excitation, a pair must be broken, so that the lowest quasiparticle excitation energy is

$$E_{exc}^{ij} = E_i - E_s = \sqrt{(\epsilon_i - \epsilon_F)^2 + \Delta^2} + \sqrt{(\epsilon_j - \epsilon_F)^2 + \Delta^2}, \quad (8)$$

where  $i$  and  $j$  correspond to the orbits of the two quasi-particles involved. The minimum value is  $E_{exc}^{ij} = 2\Delta$ , giving the ‘pairing gap’ a minimum limit  $\sim 1\text{-}2$  MeV.

## 2.2 Nuclear deformation

The deformation of the nuclear shape is a fundamental property of the atomic nucleus. To understand its connection with the collective nuclear motion, consider the multipole expansion of the nuclear surface in the  $(\theta, \phi)$  direction at the time  $t$  [47],

$$R(\theta, \phi, t) = R_0 \left\{ 1 + \sum_{l=0}^{\infty} \sum_{m=-l}^l \alpha_{l,m}(t) Y_{l,m}(\theta, \phi) \right\}, \quad (9)$$

where  $R_0 = 1.2 \cdot A^{1/3}$  fm, corresponds to the mean value of the nuclear radius.

The case  $\alpha_{l,m}(t) = 0 \forall (l, m)$  represents an static spherical or ‘non-deformed’ shape. In deformed nuclei, the  $\alpha_{l,m}(t)$  coefficients provide the amplitude of the nuclear shape at the multipole order  $(l, m)$ . Hence, they act as the collective coordinates of the nucleus, being the  $Y_{l,m}(\theta, \phi)$  the directional vectors. In principle, deformations at all multipole orders ( $l \in [0, \infty)$ ) are possible. However, there is no evidence of pure deformations for  $l \geq 4$  [47], so here only the lowest multipole orders are described, see Figure 2.2.

The monopole deformation,  $l = 0$ , corresponds to an oscillation of the nuclear radius of spherical shape. A large amount of energy is needed for such a compression of nuclear matter, so this mode is far too high in energy ( $\sim 20$  MeV) [47] in comparison to the low-energy spectra around few MeV studied here.

The dipole deformations,  $l = 1$ , correspond to displacements of the nuclear center of mass. The characteristic excitations are the Giant Dipole Resonance (GDR), interpreted as a resonance due to the oscillation of the proton distribution and neutron distribution against each other. The displacement of much of the nuclear

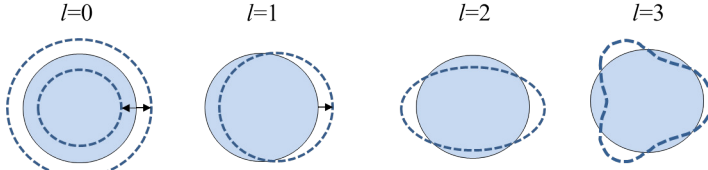


**Figure 2.2:** Schematics of low-order multipolar deformations. For simplicity, only the axially symmetric shapes are shown: The  $m=0$  pear-like shape of the octupolar order ( $l=3$ ), and the  $m=0$  prolate ellipsoidal shape of the quadrupolar order ( $l=2$ ).

matter demands considerable excitation energy, so this mode is typically around  $\sim 8\text{--}20$  MeV. Pigmy resonances, starting around 5 MeV and below the nucleon separation threshold, have also been found [48]. There is; however, a low-lying magnetic dipole excitation<sup>2</sup> occurring in heavy deformed nuclei at roughly 3 MeV and corresponds to the vibration of the proton and neutron distributions against each other, each one conserving their shape, and oscillating in a scissors type of motion, different to the linear vibrations of GDR [11, 50].

The octupolar deformation,  $l = 3$ , has a bigger influence in the non-axially symmetric deformed shapes associated with negative parity collective states. The  $m=0$  component, with an axially symmetric pear-like deformation, was recently found only for heavy nuclei ( $A\sim 220$ ) [51].

### 2.2.1 Quadrupolar Deformations

The quadrupolar order  $l = 2$ , describes the most common nuclear deformations associated to low-lying collective excitations. It is convenient here to consider also the expression of the collective coordinates  $\alpha_{2\mu}$  in terms of the three Euler angles and two intrinsic variables  $(\beta, \gamma)$ :

$$\alpha_{20} = \beta_2 \cos \gamma, \quad \alpha_{22} = \alpha_{2-2} = \frac{1}{\sqrt{2}} \beta_2 \sin \gamma. \quad (10)$$

As a convention  $\beta_2 \equiv \beta$  and  $0^\circ \leq \gamma \leq 60^\circ$ . In the cases when  $\gamma=0, 60^\circ$ , the simplest possible deformations occur, which corresponds to an axially-symmetric ellipsoid. Its shape is given by

$$R(\theta) = R_0 [1 + \beta Y_{20}(\theta)], \quad (11)$$

where the *quadrupole deformation parameter*  $\beta$  is related to the length difference between the major and minor axis of the ellipsoid  $\delta R$ , by

$$\beta = \pm \frac{4}{3} \sqrt{\frac{\pi}{5}} \frac{\delta R}{R_0}. \quad (12)$$

<sup>2</sup> Discovered with electron-scattering experiments in 1983 at T.U. Darmstadt [49].

The  $+(-)$  case occurs when  $\gamma=0^\circ(60^\circ)$ , so the major-axis of the ellipsoid is parallel (perpendicular) to the symmetry axis. Each case is known as prolate (oblate), respectively. Experimentally, oblate nuclear shapes are much less common than prolate ones [4]. A larger  $\beta$  represents a more deformed nucleus, and  $\beta=0$  is the spherical shape. When the elongation of the ellipsoid is different in the three axis, the nuclear deformation is axially asymmetric, also known as triaxial. In such a case the shape is expressed by Equations 10, in particular  $0^\circ < \gamma < 60^\circ$ . A convenient representation of the quadrupolar shapes is given by the  $(\beta, \gamma)$  plane, see Figure 2.3.

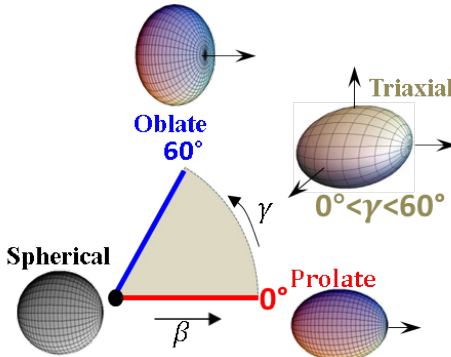


**Figure 2.3:**  $(\beta, \gamma)$  plane or *triaxial map* of all possible quadrupolar deformations. For  $\beta > 0$ , the limit cases  $\gamma = 0^\circ$  and  $\gamma = 60^\circ$  correspond to the prolate and oblate deformations. For  $\beta = 0$ , the spherical shape. For the intermediate values  $\beta > 0$ ,  $0^\circ < \gamma < 60^\circ$ , axially-asymmetric triaxial shapes.

### 2.3 The Collective model

Bohr and Mottelson introduced a nuclear model where the amplitude of the different multipolar deformations played the role of the nuclear coordinates, instead of the positions of individual nucleons. Restricting the discussion to quadrupolar deformations, the *five-dimensional collective Hamiltonian* is given by [52]

$$H_{coll} = T_{vib} + T_{rot} + V(\beta, \gamma), \quad (13)$$

$$T_{vib} = \frac{1}{2} D_{\beta\beta} \dot{\beta}^2 + D_{\beta\gamma} \dot{\beta} \dot{\gamma} + \frac{1}{2} D_{\gamma\gamma} \dot{\gamma}^2, \quad (14)$$

$$T_{rot} = \frac{1}{2} \sum_{k=1}^3 \mathfrak{J}_k \dot{\varphi}_k^2 = \frac{1}{2} \sum_{k=1}^3 I_k^2. \quad (15)$$

The quadrupole deformation parameters  $(\beta, \gamma)$  and the Euler angles  $\varphi_k$  are treated as the dynamical variables; the quantities  $D_{ij}$  in the vibrational kinetic

energy part,  $T_{vib}$ , represent *inertial masses* for the vibrational motion and are functions of  $(\beta, \gamma)$ ; and the  $\mathfrak{J}_k$  and  $I_k$  terms in the rotational kinetic energy part,  $T_{rot}$ , correspond to the moments of inertia and angular momenta components with respect to each axis of the intrinsic body-frame axis, respectively.  $V(\beta, \gamma)$  corresponds to the potential energy as a function of the quadrupolar deformation.

The Hamiltonian  $H_{coll}$  is a general form of collective possible excitations at a quadrupolar deformation level. It is better understood considering the important specific cases of pure rotational and vibrational modes.

---

### 2.3.1 Axially symmetric rotors

---

Around the decade of the 50's, quantized rotational motion had been already identified as a standard excitation mode in molecules, so it was somehow expected that nuclear rotational motion would either be a property of all nuclei or none, and if so, it would have an associated moment of inertia close to the rigid body value, the same way as in the molecular case [53]. The data, however, soon proved that the real situation was less simple: For even-even nuclei far from the shell closures, the lowest-lying transitions were found to have a strength around 100 of times stronger than the Weisskopf estimates<sup>3</sup>, and the excitation energy of the levels followed a characteristic sequence  $I(I+1)$ , with  $I$  the angular momentum of the level. See, for example, the mid-shell regions around  $Z \sim 66$  (Dy),  $A \sim 170$ ; or  $Z \sim 40$  (Zr),  $A \sim 100$ .

The explanation of this type of spectrum is one of the biggest successes of the Collective model. Consider the rotation of a nucleus with the simplest possible deformation, e.g. an axially symmetric quadrupolar shape, such that the corresponding angular momentum forms some angle with respect to the symmetry axis. The component of the rotation parallel to the symmetry axis has no physical changes on the state of a quantum mechanical system due to the rotational invariance, so only the perpendicular component can exist (that is the reason why spherical nuclei do not have ground-state rotational bands). The rotation can be represented by the quantized Hamiltonian of a rotating body with fixed axis, obtained from Equation (13) for  $T_{vib}=0$ , as well as  $I_3=0$ ,  $I_1=I_2=I$ , so the Hamiltonian reduces to:

$$H_{rot} = \frac{\hat{I}^2}{2\mathfrak{J}} ; \quad E_I = \frac{\hbar^2 I(I+1)}{2\mathfrak{J}}. \quad (16)$$

with  $\mathfrak{J}$  the nuclear moment of inertia. In a spherical nucleus all  $2I+1$  intrinsic magnetic substates are degenerate in energy, however, it is not the case for a deformed nucleus (see Section 2.4). Instead, the projection  $K$  of the angular momentum on the symmetry axis defines the energy level, remaining a degeneracy for the levels

---

<sup>3</sup> e.g. a transition caused by a single nucleon, see Section 4.2.4

with projection values  $K$  and  $-K$ . The nuclear wave function must reflect this, so it is represented by [11]

$$\Psi_{IM} = \sum_{K \geq 0} a_K |IK\rangle; \quad (17)$$

$$|IK\rangle = \sqrt{\frac{2I+1}{16\pi^2}} (D_{M,K}^I \chi_K + (-1)^{J-K} D_{M,-K}^I \chi_{-K}). \quad (18)$$

When  $K=0$ , The wave function collapses for odd values of  $I$ , so only the even values  $I=0^+, 2^+, 4^+, \dots$ , are allowed for even-even nuclei. This set of states with similar  $K$  is said to define a rotational band. Given the quantum nature of the nucleus, the comparison of  $\mathfrak{J}$  with a classical rigid rotor is of interest. From Equation (16), the moment of inertia in the transition between two consecutive states is

$$E_I - E_{I-2} = \frac{\hbar^2}{2\mathfrak{J}} (4I - 2) \Rightarrow \mathfrak{J}_{exp} = \frac{2I-1}{E_I - E_{I-2}} \hbar^2, \quad (19)$$

this expression allows obtaining  $\mathfrak{J}$  from experimental data since the energy difference between the states involved in the  $I \rightarrow I-2$  transition corresponds to the energy of the  $\gamma$ -ray emitted by the nucleus (Section 4.2.1). For most of the  $I^\pi = 2_1^+$  states of deformed nuclei, the  $\gamma$ -ray energy of the decay to the ground state is around 80-500 keV [4]; for instance,  $E(2_1^+) = 221$  keV for  $^{100}\text{Zr}$ , leading to  $\mathfrak{J}_{exp} \sim 13.5 \hbar^2 / \text{MeV}$ .

On the other hand, for a rigid ellipsoid rotating perpendicularly to the symmetry axis, the classical moment of inertia is given by [54]

$$\mathfrak{J}_{rigid} = \mathfrak{J}_{sph.} \left( 1 + (\sqrt{45/16\pi})\beta/3 \right) \approx 2MR_0^2(1 + 0.314\beta)/5, \quad (20)$$

Evaluating for  $^{100}\text{Zr}$ ,  $A=100$  and  $\beta_2=0.343$ . Besides,  $M=m_0A$ ,  $m_0=937 \text{ MeV}/c^2$ , and  $\hbar c=197 \text{ MeV}\cdot\text{fm}$ , so

$$\begin{aligned} \mathfrak{J}_{rigid} &= (2/5)(937 \text{ MeV}/c^2 \cdot A)(1.2A^{1/3} \text{ fm})^2 (1 + 0.314\beta) \hbar^2/\text{MeV} \\ &\approx 33.2\hbar^2/\text{MeV} \geq \mathfrak{J}_{exp}. \end{aligned}$$

This feature is characteristic of the nuclear rotational movement, so it is not entirely equivalent to the molecular case.  $\mathfrak{J}$  can change along the states of a rotational band since it is not known whether or not the positions of the nucleons with respect to each other remain independent of the excitation energy. For constant  $\mathfrak{J}$ , the energy ratio of the lowest rotational states,  $E(4_1^+)$  and  $E(2_1^+)$ , is given by

$$R_{4/2} = \frac{E(4_1^+)}{E(2_1^+)} = \frac{4(4+1)}{2(2+1)} = \frac{20}{6} = 3.33. \quad (21)$$

This value is one of the most used signatures to identify rigid axially symmetric deformed states of even-even nuclei. Naturally, the strong simplifications assumed in this treatment do not necessarily remain valid in many real situations. The shape

deformation can have small non-axially symmetric contributions so the deformation is not rigid but soft, leading to lower  $R_{4/2}$  values [47].

### 2.3.2 Excitations for axially-asymmetric deformations

The next simplest deformation beyond axially symmetric ellipsoids, corresponds to the quadrupolar deformations where the axial-symmetry is actually not preserved, so the elongation of the nuclear shape (ellipsoid) along the three principal axis is different, see Figure 2.3. In terms of the parametrization used so far, these kind of deformations correspond to non-zero values of  $(\beta, \gamma)$ .

The ideal case of a *rigid axially asymmetric* nucleus was first studied by Davydov and Filippov [55]. It has a Hamiltonian given by

$$H_{triax} = \sum_{i=1}^3 \frac{\hat{I}_i^2}{2\mathfrak{J}_i}, \quad \mathfrak{J}_i = 4B\beta^2 \sin^2 \left\{ \gamma - \frac{2\pi}{3}i \right\}, \quad (22)$$

with  $\hat{I}_i$  the angular momentum projector operators, and  $\mathfrak{J}_i$  the moment of inertia along the axis  $i=1,2,3$  of the body-fixed coordinate system, respectively. Though the stationary states for this Hamiltonian have a defined angular momentum, the projections along the different axis do not have defined values. Hence, the energy levels cannot be specified by  $K$ , and each value of angular momentum leads to  $2I+1$  energy levels.

The energies for the lowest-lying rotational levels have in fact analytical expressions, their derivation can be seen in detail in Ref. [56]. Particularly important are the two lowest levels with angular momentum  $I = 2$ , labeled as  $2_1^+$  and  $2_2^+$ . Their energies as a function of the  $(\beta, \gamma)$  parameters are given by

$$\begin{aligned} E(2_1^+) &= \frac{9(1 - \sqrt{8 \sin^2(3\gamma)/9})}{\sin^2(3\gamma)}, \\ E(2_2^+) &= \frac{9(1 + \sqrt{8 \sin^2(3\gamma)/9})}{\sin^2(3\gamma)}, \\ R_{2/2} &= \frac{E(2_1^+)}{E(2_2^+)} = \frac{3 + \sqrt{9 - 8 \sin^2(3\gamma)}}{3 - \sqrt{9 - 8 \sin^2(3\gamma)}}, \end{aligned} \quad (23)$$

where the energies are expressed in units of  $\hbar^2/4B\beta^2$ . Additionally, it is also satisfied that  $E(3_1^+) = E(2_1^+) + E(2_2^+)$ . The ratio  $R_{2/2}$  can be very useful since it allows to estimate the degree of triaxiality directly from the spectroscopy information, its behaviour is shown in Figure 2.5.

The behaviour of the lowest excited levels as a function of  $\gamma$  is shown in Figure 2.4. In the limit of  $\gamma \rightarrow 0^\circ$  the rotational band of the ground-state corresponds to the spectra of the axially-symmetric rotor. For increasing  $\gamma$ , the set of states  $2_2^+, 3_1^+, 4_2^+, 5_1^+$  (which are sometimes labeled with 'γ') go drastically down in energy. After

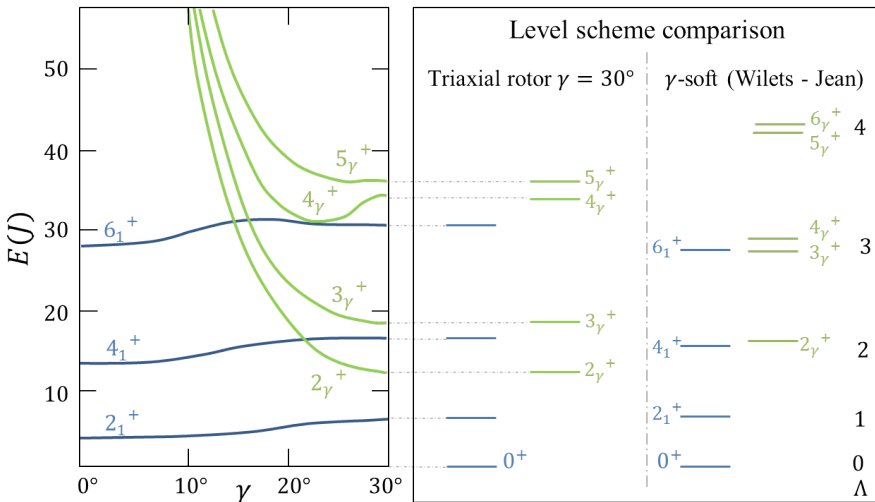


**Figure 2.4:** (Left) Energy levels as a function of  $\gamma$  for the rigid triaxial rotor model. (Right) Comparison of the level schemes obtained for the triaxial rotor at  $\gamma=30^\circ$  and the  $\gamma$ -soft model of Wilets-Jean. The levels of the so-called  $\gamma$ -band correspond to  $2_\gamma^+=2_2^+$ ,  $3_\gamma^+=3_1^+$ ,  $4_\gamma^+=4_2^+$ ,  $5_\gamma^+=5_1^+$  and so on. Based on [57].

$\gamma \geq 22^\circ$  it occurs that  $E(2_2^+) < E(4_1^+)$  and  $E(3_1^+) < E(4_1^+)$ , which is a useful signature that can be directly evaluated from spectroscopy data. The maximum degree of axial asymmetry (e.g. the degree of triaxiality) is reached when  $\gamma=30^\circ$ ; afterwards, the behaviour is symmetric for the intervals  $0^\circ \leq \gamma \leq 30^\circ$  and  $30^\circ \leq \gamma \leq 60^\circ$ . Therefore, the relative positioning of the levels cannot offer insights to distinguish between prolate and oblate *rigid* deformations. The Davydov model also provides analytic formulas for the reduced quadrupole transition probability between two states with the assumption that the *intrinsic shape does not change* for different states,

$$B(E2; 2_1^+ \rightarrow 0_1^+) + B(E2; 2_2^+ \rightarrow 0_1^+) = 1$$

$$B(E2; 2_1^+ \rightarrow 0_1^+) = \frac{1}{2} \left( 1 + \frac{3 - 2 \sin^2(3\gamma)}{\sqrt{9 - 8 \sin^2(3\gamma)}} \right),$$

$$B(E2; 2_2^+ \rightarrow 0_1^+) = \frac{1}{2} \left( 1 - \frac{3 - 2 \sin^2(3\gamma)}{\sqrt{9 - 8 \sin^2(3\gamma)}} \right),$$

with the  $B(E2)$  values normalized to  $e^2 Q_0^2 / 16\pi$ , and  $Q_0 = 3ZR^2\beta / \sqrt{5\pi}$  the intrinsic electric quadrupole moment of a nucleus only with axial deformation  $\beta$ . The behaviour of the ratios of these quantities as a function of the triaxiality is shown in Figure 2.5. The transition  $2_2^+ \rightarrow 2_1^+$  is much stronger than the transition  $2_2^+ \rightarrow 0_1^+$

for all values of triaxiality, which is a useful signature since it can be compared to experimental branching ratios. The ratio of the decay strength for the transitions  $2_1^+ \rightarrow 0_1^+$  and  $2_2^+ \rightarrow 0_1^+$  increases from 1.43 at  $\gamma=0$  towards infinity in the limit of  $\gamma = 30^\circ$ . In contrast, the ratio of the decay strength between the  $2_2^+ \rightarrow 2_1^+$  and  $2_1^+ \rightarrow 0_1^+$  transitions is much lower, with a peak around  $\gamma = 22^\circ$ , and vanishing for  $\gamma = 0$  and  $30^\circ$ .

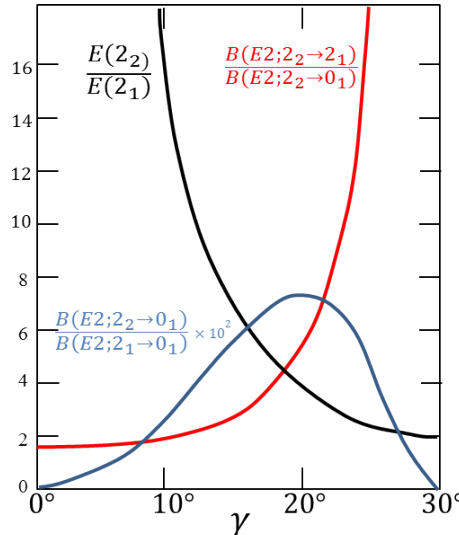


**Figure 2.5:** Predictions of the Davydov model for several observables:  $R_{2/2}$ , the energy ratio of the first  $2^+$  states; the decay strength ratio for the transitions  $2_2^+ \rightarrow 2_1^+$  and  $2_2^+ \rightarrow 0_1^+$ ; and the decay strength ratio for the transitions  $2_2^+ \rightarrow 0_1^+$  and  $2_1^+ \rightarrow 0_1^+$ . Based on [11].

The Wilets and Jean model [58] represents another important limit case of the Collective Hamiltonian known as  $\gamma$ -soft. It considers the case when the nucleus is not rigid but free to vibrate in the  $\gamma$  degree of freedom, condition known as ‘ $\gamma$ -instability’. In this situation the potential is totally independent of  $\gamma$ , so the Hamiltonian becomes separable in these two coordinates since the potential is of the form  $V(\beta, \gamma) = f(\beta)$ . Furthermore, when  $V$  is harmonic in  $\beta$  around a non-zero  $\beta_0$  value,

$$V(\beta) = \frac{1}{2}C(\beta - \beta_0)^2 = \frac{1}{2}C \sum_{\mu=-2}^2 |\alpha_\mu - \alpha_\mu(0)|^2,$$

then the energy of each state is given by [11, 58]

$$E_{W-J}(\Lambda) = \vartheta \Lambda(\Lambda + 3); \quad \Lambda = 0, 1, 2, 3, \dots,$$

where  $\vartheta$  is analogous to  $\hbar^2/2\mathfrak{J}$  and the quantum number  $\Lambda$  keeps the degeneracy relation with the angular momentum shown in Table 1.

$\Lambda$	$J$
0	0
1	2
2	2,4
3	0,3,4,6

**Table 1:** Degeneracy between  $\Lambda$  and  $J$  values in the Wilets-Jean model.

The band structure representation of the lowest levels is shown in Figure 2.4. In particular, the yrast levels follow the relation  $J = 2\lambda(\lambda + 3)$ , and they have very similar energies to the case of the triaxial rigid rotor at  $\gamma=30^\circ$ . The  $R_{4/2}$  ratio is given by

$$R_{4/2} = \frac{E(4_1^+)}{E(2_1^+)} = 2.5. \quad (24)$$

The signatures to distinguish between both models are related to the characteristics of their  $\gamma$ -bands. In the first place, the  $R_{2/2}$  ratios are given by

$$R_{2/2}^{W-J} = 2.5, \quad R_{2/2}^{D-F}(\gamma = 30^\circ) = 2.0. \quad (25)$$

Also, for the triaxial rotor the states group as  $(2_\gamma^+, 3_\gamma^+)$ ,  $(4_\gamma^+, 5_\gamma^+)$ , ..., while for the Wilets-Jean case they group as  $(2_\gamma^+)$ ,  $(3_\gamma^+, 4_\gamma^+)$ ,  $(5_\gamma^+, 6_\gamma^+)$ . This feature induces the definition of a signature to distinguish both cases, known as *staggering* [57],

$$S(4) = \frac{(E_{4_\gamma^+} - E_{3_\gamma^+}) - (E_{3_\gamma^+} - E_{2_\gamma^+})}{E_{2_\gamma^+}), \quad (26)$$

the values for the ideal models considered so far are:

$$\begin{aligned} S(4) &= 1/3 & (\text{symmetric rotor}), \\ S(4) &= 5/3 & (\gamma\text{-rigid} - 30^\circ), \\ S(4) &= -2 & (\gamma\text{-soft}). \end{aligned} \quad (27)$$

### 2.3.3 Vibrational excitations

For some near-spherical nuclei close to the shell closures (such as the  $Z=48$  Cd isotopes) neither the independent particle model nor the collective rotations explained the low-lying spectra. The origin comes from vibrations around the spherical shape at some multipole order  $l$  of the nuclear deformation. The harmonic oscillations of the  $\alpha_{l,m}(t)$  coordinates around the equilibrium values can be expressed in a collective Hamiltonian [59]

$$H = \sum_{l,m} H_{l,m} = \frac{1}{2} \sum_{l,m} \{B_l |\alpha_{l,m}^i|^2 + C_l |\alpha_{l,m}^e|^2\}. \quad (28)$$

After a quantization process for the  $\alpha_{l,m}$  and their associated conjugate momenta  $\pi_{l,m} = \partial L / \partial \dot{\alpha}_{l,m} = B_l \dot{\alpha}_{l,m}^*(t)$ , the introduction of the standard creation-annihilation operators  $O_{l,m}^\dagger$ , and  $O_{l,m}$  is straightforward; so the Hamiltonian becomes

$$H = \sum_{l,m} H_{l,m} = \sum_{l,m} \hbar\omega_l \{O_{l,m}^\dagger O_{l,m} + 1/2\}; \quad [O_{l,m}^\dagger, O_{l,m}] = \mathbb{I}. \quad (29)$$

The vibrational collective states can be understood as combinations of excitations between the different  $(l, m)$  oscillators in Equation (29). For the lowest non-trivial multipole deformations with  $l = 2$  the Hamiltonian becomes

$$H \approx \sum_{m=-2}^2 \hbar\omega \{O_{2,m}^\dagger O_{2,m} + 1/2\} \approx \hbar\omega \{\hat{N} + 5/2\}; \quad \hat{N} = \sum_{m=-2}^2 O_{2,m}^\dagger O_{2,m}. \quad (30)$$

$\hat{N}$  corresponds to the number of quadrupole phonons present. This expression represents five harmonic oscillators, each with a value  $m$ . The eigenstates have the general form  $|N, l, m\rangle$ , with  $l$  the angular momentum, and its projection  $m$ . The first excited states of this system can be deduced by means of successive applications of the creation operators  $O_{2,m}^\dagger$  to the ground state [47]:

- Ground state,  $|N = 0, l = 0, m = 0\rangle$ . It has zero phonons ( $N=0$ ), energy  $\frac{5}{2}\hbar\omega$ , and nuclear angular momentum  $l=0$ .
- First excited state,  $O_{2,m}^\dagger |0, 0, 0\rangle = |N = 1, l = 2, m\rangle$ . Characterized by one phonon ( $N=1$ ), energy  $\frac{7}{2}\hbar\omega$ , and nuclear angular momentum  $l=2^+$ . Its degeneracy is given by  $-l \leq m \leq l$ .
- Second excited state,  $O_{2,m}^\dagger |1, 2, m\rangle = |N = 2, l, m'\rangle$ . Characterized by two phonons ( $N=2$ ), and energy  $\frac{9}{2}\hbar\omega$ . Its degeneracy is given by  $l=0^+, 2^+, 4^+$ ; and  $-l \leq m \leq l$ , for each  $l$ .

The ratio between the excitation energies of the two lowest transitions is given by

$$R_{4/2} = \frac{E(4_1^+)}{E(2_1^+)} = \frac{(9-5)\hbar\omega/2}{(7-5)\hbar\omega/2} = 2. \quad (31)$$

and the decay strength ratio between the  $N = 2$  and  $N = 1$  states:

$$B_{2n/2} = \frac{B(E2; 0_2^+, 2_2^+, 4_1^+ \rightarrow 2_1^+)}{B(E2; 2_1^+ \rightarrow 0_1^+)} = 2. \quad (32)$$

## 2.4 The Nilsson model

The single-particle model with an effective mean-field potential which is not spherical *but deformed* was proposed by S. G. Nilsson in 1955 [12]. Considering that the effective potential should somehow follow the distribution of the nucleons, it

is expected then to be deformed if a non uniform arrangement of particles takes place, which is physically reasonable. This model applies then for those nuclei far from the shell closures, where substantial deformations are observed. In a spherical potential, the magnetic substates of the  $(nlj)$  level are degenerate in energy, but the presence of a deformed potential breaks this degeneracy favouring energetically some of these substates. The situation shown in Figure 2.6 shows a (simple) prolate-deformed potential and two  $j$ -orbits with  $K_1$  and  $K_2$ , the maximum and minimum angular momentum projection in the symmetry axis, e.g.  $K_1 = \pm j$  and  $K_2 = \pm 1/2$ . The particle in the  $K_2$  orbit is in average closer to the potential bulk than the particle in the  $K_1$  orbit which is more perpendicular; therefore,  $K_2$  ( $K_1$ ) will be more (less) attracted than in the spherical-potential scenario. Geometrically, the energy shift of each substate depends on the angle of its orbit with respect to the symmetry axis,  $\sin \theta \sim K/j$ . Given the symmetry of the deformation, both orbits of the substates  $K = \pm m$  ( $m = 1/2, 3/2, \dots, j$ ) have the same angle and so the same single-particle energy variation. For an oblate-deformed potential the situation is inverted so the orbitals with  $K_1$  would be more attracted. Since the interaction is short-range, the magnitude of the  $K$ -splitting in energy must be more pronounced for larger deformations. A schematic illustration of the energy splitting for the spherical-orbital  $(nlj)$  into the  $(2j+1)/2$  levels of different  $K$  values is shown Figure 2.6.

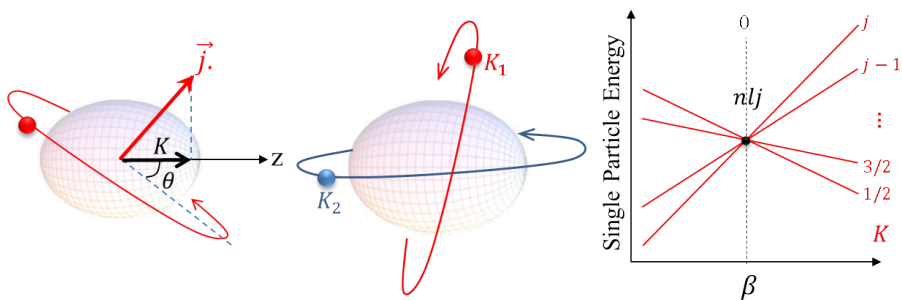


**Figure 2.6:** Geometry of a 'spherical' orbit interacting with an axially symmetric deformed potential. The strength of the interaction changes with the angle  $\theta$  between the orbit plane and the symmetry axis, such that the the smaller the angle, the stronger(weaker) the interaction for prolate (oblate) deformations. The split of the single particle energy for the substates of an  $nlj$  spherical-level as a function of the deformation is also illustrated schematically to the right.

The energy of the single particle levels in the Nilsson model depends obviously on the parametrization used for the potential. In general, they are solution of the single particle Hamiltonian

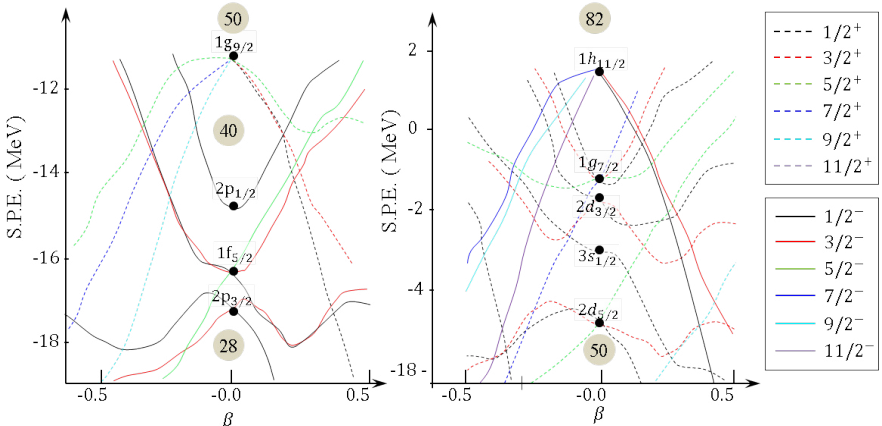
$$H = \frac{\vec{p}^2}{2m} + V(r, \theta) + D\vec{l}^2 - C\vec{l} \cdot \vec{s}. \quad (33)$$

The effective potential  $V(r, \theta)$  can be a deformed harmonic oscillator, a modified Woods-Saxon, self-consistent Gogny-D1S, etc. [60]). A *Nilsson diagram* corresponds to a plot of single-particle energies (SPE) for each  $K$ -level as a function of the axial quadrupolar deformation  $\beta$ , see Figures 3.2 and 3.3. In this axially deformed potential, the angular momentum is not anymore a good quantum number but only  $K$ , so the energy levels are labeled as

$$K^\pi[Nn_z\Lambda], \quad (34)$$

with  $\pi=(-1)^l$  the parity of the orbital,  $N$  the number of the major shell,  $n_z$  the number of nodes of the wave function along the symmetry axis direction, and  $K$  the sum of the projections of the orbital angular momentum and spin,  $K=\Lambda\pm 1/2$ .

To correctly label the levels stemming from each  $(nlj)$  in the diagram, notice that for the ‘more aligned’ orbits to the axis the wave function is more extended along  $z$ , so  $n_z$  takes its maximum value  $N$ . Besides, in that case the angular momentum projection is minimum and equal to  $K=1/2$ . Notice that for positive (negative) parity the possible values of  $n_z + \Lambda$  must be even (odd) if  $N$  is even (odd), allowing this to select the correct value of  $\Lambda$  (recall that  $K=\Lambda\pm 1/2$  in general). For instance, for the  $1g_{9/2}$  proton orbital ( $\pi 1g_{9/2}$ ) in the diagram of Figure 2.7 it occurs that  $l=4$  and  $n=1$  so  $N=2(n-1)+l=4$  and  $\pi=(-1)^l=+1$ . Since  $N$  is even, for the  $K^\pi=1/2^+$  level it must be that  $\Lambda=0$ . The level sequence is then given by  $1/2^+[440]$ ,  $3/2^+[431]$ ,  $5/2^+[422]$ ,  $7/2^+[413]$ , and  $9/2^+[404]$ .



---

### 3 State-of-the-art Beyond-Mean-Field Calculations

---

The complexity of the nuclear many-body problem due to its mesoscopic nature and the complexity of the nuclear interaction has motivated several approaches and models to describe different nuclear properties. Nowadays, the large-scale interacting shell model calculations [8, 34] stands as rather succesfull tool to compute low-lying states and spectroscopic features along large regions of the nuclide chart. It demands very high computing power since it relies on considering a very large valence space for accurately results. Nevertheless, the optimal interaction used for the calculation is still not shown to be universal along the nuclide chart and somehow must be tuned to a particular mass region. There is another very succesfull approach to perform calculations known as *Beyond-Mean-Field methods* using density-dependent functional forces. The effective interactions used in these type of calculations have already been fitted to describe bulk properties along the nuclide chart [61], which confers them a global character so they can be expected to have good predictive power on not explored regions so far. In general, state-of-the-art Beyond-Mean-Field Theories (BMF) consist of the following steps:

1. Derivation of a self-consistent mean field potential via a method such as the Constrained Hartree-Fock-Bogoliubov calculations. In particular, the particle-number, angular-momentum and parity symmetries broken at the HFB level are restored. Additional constraints on observables such as the deformation or the angular momentum can be added in order to analyze the behaviour of specific collective degrees of freedom of a nucleus.

2. A beyond-mean-field calculation to obtain the properties of excited states. For this step, alternative methods have been developed with different degrees of sophistication. For the neutron-rich Selenium nuclei studied in this thesis, there are very recent publications using different approaches:

- A Symmetry-Conserving Configuration-Mixing (SCCM) calculations based on the Generator Coordinates Method (GCM) using the variation after particle-number-projection method (PN-VAP) to restore symmetries. For details see Refs. [24, 31].
- A Five Dimensional Collective Hamiltonian (5DCH) calculations, also based on the GCM where the input parameters of the Hamiltonian such as the potential, moments of inertia and mass parameters are obtained from the CHFB calculations. For details see Refs. [38, 62].
- An Interacting Boson Model (IBM) calculation, where the mean-field as a function of  $(\beta, \gamma)$  is mapped into the expectation value of the IBM Hamiltonian with configuration mixing in the boson condensate state. The resultant Hamiltonian is used to compute excitation energies and electromagnetic

properties. This type of calculations will be used for the data comparison but will not be explained more extensively, since they do not provide information on the single particle structure and their agreement with the data is the less accurate. For details, the reader is welcomed to review Ref. [41].

### 3.1 Gogny effective interaction

In all the calculations here discussed, the Gogny interaction [63] was used as the effective nucleon-nucleon interaction. Its expression is given by [61]

$$V_{12} = \sum_{i=1}^2 e^{-(\vec{r}_1 - \vec{r}_2)^2/\mu_i^2} (W_i + B_i P_\sigma - H_i P_\tau - M_i P_\sigma P_\tau) + W_{LS}(\vec{\sigma}_1 + \vec{\sigma}_2) \vec{k} \times \delta(\vec{r}_1 - \vec{r}_2) \vec{k} + V_{12}^C + V_{DD}. \quad (35)$$

It consists of a central finite range part (first line), a spin-orbit interaction having a zero range (second line), a Coulomb term for the interaction between protons

$$V_{12}^C = (1 + 2\tau_{1z})(1 + 2\tau_{2z}) \frac{e^2}{|\vec{r}_1 - \vec{r}_2|}, \quad (36)$$

and a density-dependent term

$$V_{DD} = t_3(1 + x_0 P_\sigma) \delta(\vec{r}_1 - \vec{r}_2) \rho^{1/3} \left( \frac{1}{2}(\vec{r}_1 + \vec{r}_2) \right), \quad (37)$$

where the density operator  $\rho(\vec{r})$  is given by

$$\hat{\rho}(\vec{r}) = \sum_{j=1}^A \delta(\vec{r} - \vec{r}_j). \quad (38)$$

There are several versions of this effective interaction, the better tested corresponds to the 'D1S' and 'D1M' parametrizations [64]. In particular, the former was used in the SCCM and 5DCH calculations and the latter in the IBM ones.

### 3.2 Constrained Hartree-Fock Bogoliubov method (CHFB)

The Hartree-Fock-Bogoliubov method is one of the most widely used mean-field approaches to solve a many-body problem. In the case of nuclear physics, The goal is to use an effective interaction and a trial wave function to find a self-consistent potential and wave function such that the Hamiltonian is minimized with respect to the energy of the system using the variational principle. In the HFB theory, the Bogoliubov transformation defines the quasiparticle (qp) operators as [61]

$$\alpha_l = \sum_k U_{kl}^* c_k + V_{kl}^* c_k^\dagger, \quad (39)$$

with  $c_k^\dagger$ ,  $c_k$  the particle creation and annihilation operators in a trial basis  $\{|\psi_k\rangle\}$ , normally the Harmonic Oscillator.  $U$  and  $V$  are the matrices to be determined with

the variational principle. Due to the mix of both creator and annihilation operators, the HFB wave function  $|\phi\rangle = \prod_k \alpha_k |0\rangle$  ( $|0\rangle$  the qp vacuum) is not eigenstate of the particle number operator. Furthermore, if the index  $k$  covers indiscriminately all the states of the trial basis then  $|\phi\rangle$  mixes states with different parity, angular momentum, deformation, etc. The non-conservation of particles and the breaking of symmetries such as parity or angular momentum are both critical problems since nuclei have indeed defined values of particles and nuclear states have defined values of angular momentum and parity. The general solution consists on the use of Lagrange multipliers  $\{\lambda_i\}$  during the minimization of the Hamiltonian using the variational principle, so that the solutions are constrained to ‘restore the broken symmetries’, which means finding a minimum energy and wave function that satisfy the conservation of good quantum numbers  $s_i$ , linked to the observables  $\mathcal{S}_i$  of interest. Concretely,

$$0 = \delta \{ \langle \phi | \hat{H} - \sum_i \lambda_i \mathcal{S}_i | \phi \rangle \}, \quad \lambda_i \rightarrow \{ \langle \phi | \mathcal{S}_i | \phi \rangle \} = s_i. \quad (40)$$

These observables can be specific nuclear properties such as the proton or neutron particle numbers, the angular momentum, the deformation, etc, are selected ‘by hand’ according to the properties that are under study or must be imposed in the system. The wave function obtained is only the particular self-consistent solution for a specific value  $s_i$  of the constraints, e.g.  $|\phi\rangle \equiv |\phi\rangle_s$ . This approach can be enough for explaining fair enough some ground-state properties using effective interactions such as Gogny or Skyrme [64]. However, the minimization procedure in Equation (40) yields only the lowest-energy solution (e.g. the ground-state) so it is not adequate for calculations of higher energy-levels (e.g. excited states).

### 3.3 Generator Coordinates method (GCM)

A much more general solution to the many-body problem can be constructed using the method of *generator coordinates* [65]. It consists on defining a trial wave function that is a linear combination of HFB solutions  $|\phi\rangle_s$  for different values of the particular parameter represented by  $s$  (referred as ‘generator coordinate’)

$$|\Psi\rangle = \sum_s f_s |\phi\rangle_s. \quad (41)$$

This apparently rather abstract approach in practice means choosing a range of values for some of the coordinates  $s$  so that each value represents a different physical state. For instance, the set of all the possible quadrupolar deformations  $(\beta, \gamma)$ , or the set of states with defined parities, values of angular momentum, etc.

In principle, the larger the amount of coordinates that explore different nuclear properties, the better the representation of the nuclear state obtained in the variational method now using the  $|\Psi\rangle$  function. Nevertheless, these type of calculations

demand high-computing power so only coordinates representing relevant aspects should be included. This minimization procedure allows to obtain the coefficients  $f_s$  from the Hill-Wheeler-Griffin Equations, see Ref [65]. This Beyond-Mean-Field approach produces a highly correlated and complete wave function that can be used to compute properties for states beyond the ground-state, by imposing specific values of angular momentum, for example.

The calculations previously mentioned for the nuclei under study in this work present some differences in the implementation of the CHFB and GCM methods previously explained. In the following, some details on their implementation will be shown, together with their predictions for  $^{90-94}\text{Se}$ .

### 3.4 Calculations for neutron-rich Selenium isotopes

#### 3.4.1 Symmetry-Conserving Configuration-Mixing (SCCM) method

In the Symmetry-Conserving Configuration-Mixing calculations the many-body states (Equation 41) are calculated as a linear combination (e.g. mixing) of HFB-type wave functions of different quadrupole shapes (both axial and triaxial) and with particle-number and angular momentum restored:

$$|\Psi^{IM\sigma}\rangle = \sum_{\beta\gamma K} f_{\beta\gamma K}^{I\sigma} P_{MK}^I P_{MK}^N P_{MK}^Z |\phi_{\beta\gamma}\rangle \quad (42)$$

where  $I, M, K$  correspond to the angular momentum and the z-axis projections in the laboratory and intrinsic frame, respectively.  $P^{N(Z)}$  are the neutron (proton) particle projectors,  $P_{MK}^I$  the angular momentum projector, and  $\sigma$  labels different states for a given value of  $I$ .

The HFB states  $|\phi_{\beta\gamma}\rangle$  are obtained with the variational principle,

$$0 = \delta \{ \langle \phi_{\beta,\gamma} | E^{N,Z}(\beta, \gamma) - \lambda_{20} \hat{Q}_{20} - \lambda_{22} \hat{Q}_{22} | \phi_{\beta,\gamma} \rangle \}, \quad (43)$$

where  $\hat{Q}_{20}$  and  $\hat{Q}_{22}$  are the operators determining the quadrupolar deformation. The values of the Lagrange multipliers  $\{\lambda_i\}$  are obtained from the constraints

$$\langle \phi_{\beta,\gamma} | \hat{Q}_{20} | \phi_{\beta,\gamma} \rangle = q_0, \quad \langle \phi_{\beta,\gamma} | \hat{Q}_{22} | \phi_{\beta,\gamma} \rangle = q_2, \quad (44)$$

and the coordinates  $q_0, q_2$  are directly related to the quadrupolar coordinates  $(\beta, \gamma)$  via

$$\beta = \sqrt{\pi/5} \sqrt{q_0^2 + 3q_2^2} / A\langle r^2 \rangle, \quad \gamma = \arctan \sqrt{3} \frac{q_2}{q_0}. \quad (45)$$

The restoration of neutron and proton number is conducted instead projecting the HFB wave function  $|\phi_{\beta,\gamma}\rangle$  with the  $\hat{P}_Z$  and  $\hat{P}_N$  operators determining the proton and neutron numbers. This step, conducted before minimization with the variational method [Equation (40)] guarantees that *only states with the right quantum numbers are used in the minimization*. This method receives the name of variation after particle-number-projection method (PN-VAP) [31].

Finally, the term  $E^{N,Z}(\beta, \gamma)$  corresponds to the potential energy surface in the triaxial map:

$$E^{N,Z}(\beta, \gamma) = \frac{\langle \phi_{\beta,\gamma} | \hat{H} \hat{P}_N \hat{P}_Z | \phi_{\beta,\gamma} \rangle}{\langle \phi_{\beta,\gamma} | \hat{P}_N \hat{P}_Z | \phi_{\beta,\gamma} \rangle} \quad (46)$$

where  $\hat{H}$  is the Hamiltonian in which the potential component is defined using the Gogny effective interaction. The calculation of the weights  $f_{\beta\gamma K}^{I\sigma}$  in Equation 42 are found using the Hill-Wheeler-Griffin Equations, which are not explicitly listed to keep simplicity.

### 3.4.2 5-Dimensional Collective Hamiltonian (5DCH) calculations

In the 5-Dimensional Collective Hamiltonian calculations the CHFB step is implemented as

$$0 = \delta \{ \langle \phi_{\beta,\gamma} | \hat{H} - \lambda_{20} \hat{Q}_{20} - \lambda_{22} \hat{Q}_{22} - \lambda_Z \hat{Z} - \lambda_N \hat{N} | \phi_{\beta,\gamma} \rangle \}, \quad (47)$$

where  $\hat{H}$  is the Hamiltonian in which the potential component is defined using the Gogny effective interaction, and the quadrupolar deformations are constrained similarly as in Equation 43. Here the particle number restoration is conducted using Lagrange multipliers instead of projecting the wave function,  $\hat{P}_Z$  and  $\hat{P}_N$  are the operators determining the proton and neutron numbers, and the values of their Lagrange multipliers are obtained from

$$\langle \phi_{\beta,\gamma} | \hat{P}_N | \phi_{\beta,\gamma} \rangle = N, \quad \langle \phi_{\beta,\gamma} | \hat{P}_Z | \phi_{\beta,\gamma} \rangle = Z. \quad (48)$$

The CHFB states  $|\phi_{\beta,\gamma}\rangle$  are used as a triaxial base of a more general correlated wave function constructed via the GCM [62]

$$|\Psi^{IM\sigma}\rangle = \sum_K \int f_{\beta\gamma K}^{I\sigma} \varphi_{MK}^I(\Omega) R(\Omega) |\phi_{\beta\gamma}\rangle \times D^{1/2} d\beta d\gamma d\Omega, \quad (49)$$

where  $\varphi_{MK}^I(\Omega)$  are the normalized combination of Wigner rotation matrices functions of the Euler angles  $\Omega$ , mentioned in Equation 18. The integral runs over the generator coordinates that in this case corresponds to the 5 dimensions of the Collective Hamiltonian [Equation (13)]. The coefficients  $f_{\beta\gamma K}^{I\sigma}$  are in principle obtained from the Hill-Wheeler-Griffin Equations. However, this process demands very high computing power so instead this integral Equation is transformed via a Gaussian Overlap approximation (GOA) [62] into the second-order differential Equation

$$\hat{H}_{coll} g_k(q_0, q_2) = E_k g_k(q_0, q_2), \quad (50)$$

with the Collective Hamiltonian to solve

$$\hat{H}_{coll} = \frac{1}{2} \sum_{k=1}^3 \frac{J_k^2}{\mathfrak{J}_k} - \frac{1}{2} \sum_{m,n=0,2} D^{-1/2} \frac{\partial}{\partial q_m} D^{1/2} B_{mn}^{-1} \frac{\partial}{\partial q_n} + V(q_0, q_2) \quad (51)$$

where  $q_0 = \beta \cos \gamma$  and  $q_2 = \beta \sin \gamma$  are explicitly used instead of  $(\beta, \gamma)$ ,  $D$  is a metric factor and  $\hat{J}_k$  are the angular momentum operators. The other terms are all computed locally with the CHFB solutions. For instance,

$$V(q_0, q_2) = \langle \phi_{\beta, \gamma} | \hat{H} | \phi_{\beta, \gamma} \rangle - \Delta V \quad (52)$$

where  $\hat{H}$  is the many-body mean field Hamiltonian where the Gogny interaction is used. To calculate the three moment of inertia, an additional constraint  $\omega \hat{J}_k$  is added to Equation (47). With the new self-consistent solution  $|\phi_{\beta, \gamma}^\omega\rangle$ , the moment of inertia are obtained as

$$\mathfrak{J}_k = \lim_{\omega \rightarrow 0} \langle \phi_{\beta, \gamma}^\omega | \hat{J}_k | \phi_{\beta, \gamma}^\omega \rangle / \omega. \quad (53)$$

Finally, the quadrupole mass parameters are calculated also in the cranking approximation, the derivation can be found in [38].

### 3.4.3 Comparison of calculations

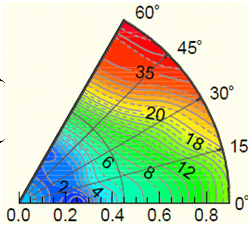
#### Potential energy surfaces (PES)

The Potential energy surfaces (PES) in the triaxial map  $(\beta, \gamma)$  obtained from the CHFB method are shown in Figure 3.1. In general, the PES show a similar behaviour, with two potential minimum evolving along the isotopic chain. At  $N=56$  ( $^{90}\text{Se}$ ), the global minimum is prolate deformed with the presence of a weaker second minima on the oblate side. The situation inverts at  $N=60$  ( $^{94}\text{Se}$ ), where the global minimum is oblate and the second minimum becomes prolate. The nucleus  $^{92}\text{Se}$  is a transitional point at  $N=58$ , where both minima have rather similar depths and are more spread over the  $\gamma$  direction. Therefore, these nuclei are predicted to have a prolate-to-oblate shape transition via a  $\gamma$ -soft shape, the transition taking place between the two coexisting equilibrium shapes (e.g. the pronounced minima of different deformations in the potential of each isotope). Note, however, that the location of the minima in the PES does not yet determine the nuclear shape, as correlations beyond the mean field have to be taken into account [66]. The similarity of the CHFB results between the different calculations is consistent since they all use Gogny force as the underlying interaction. There are, however, some differences between the plots as well. For instance, the depth of the second minima is smaller for CHFB+5DCH, it increases for the CHFB+SCCM, and is more pronounced for the CHFB+IBM. Also, the degree of  $\gamma$ -softness of the minima of  $^{92}\text{Se}$  also changes, being more evident for CHFB+5DCH, decreasing a bit in CHFB+SCCM, and even more in CHFB+IBM.

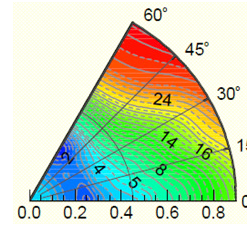
#### Nilsson diagrams

The general behaviour of the energy potential surfaces can be understood analyzing the underlying Nilsson single particle levels, which have been reported in the publications of the SCCM and 5DCH calculations and are shown in Figures 3.2

$^{90}\text{Se}_{56}$



$^{92}\text{Se}_{58}$



$^{94}\text{Se}_{60}$

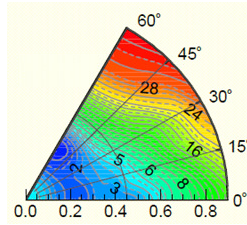


**Figure 3.1:** Contour plot of potential energy surfaces in the triaxial map ( $\beta, \gamma$ ) for the even-even neutron-rich  $^{90,92,94}\text{Se}$ . The potential depth is represented in color scale, in all three cases the deepest points correspond to blue, with the less deeper the closer to red. Further details on the scales and the number of grid points can be found on the references. For the present comparison is enough to see that they follow similar trends.

and 3.3. The predicted energies of excited states are presented in Chapter 8, when compared to experimental results. The evolution of the different orbitals is qualitatively similar in both calculations. The number of neutrons in the gaps of Figure 3.3 indicate the deformation of the minima in the potential energy surfaces. The levels for protons were not reported but it is mentioned that the diagrams are similar, but shifted in energy.

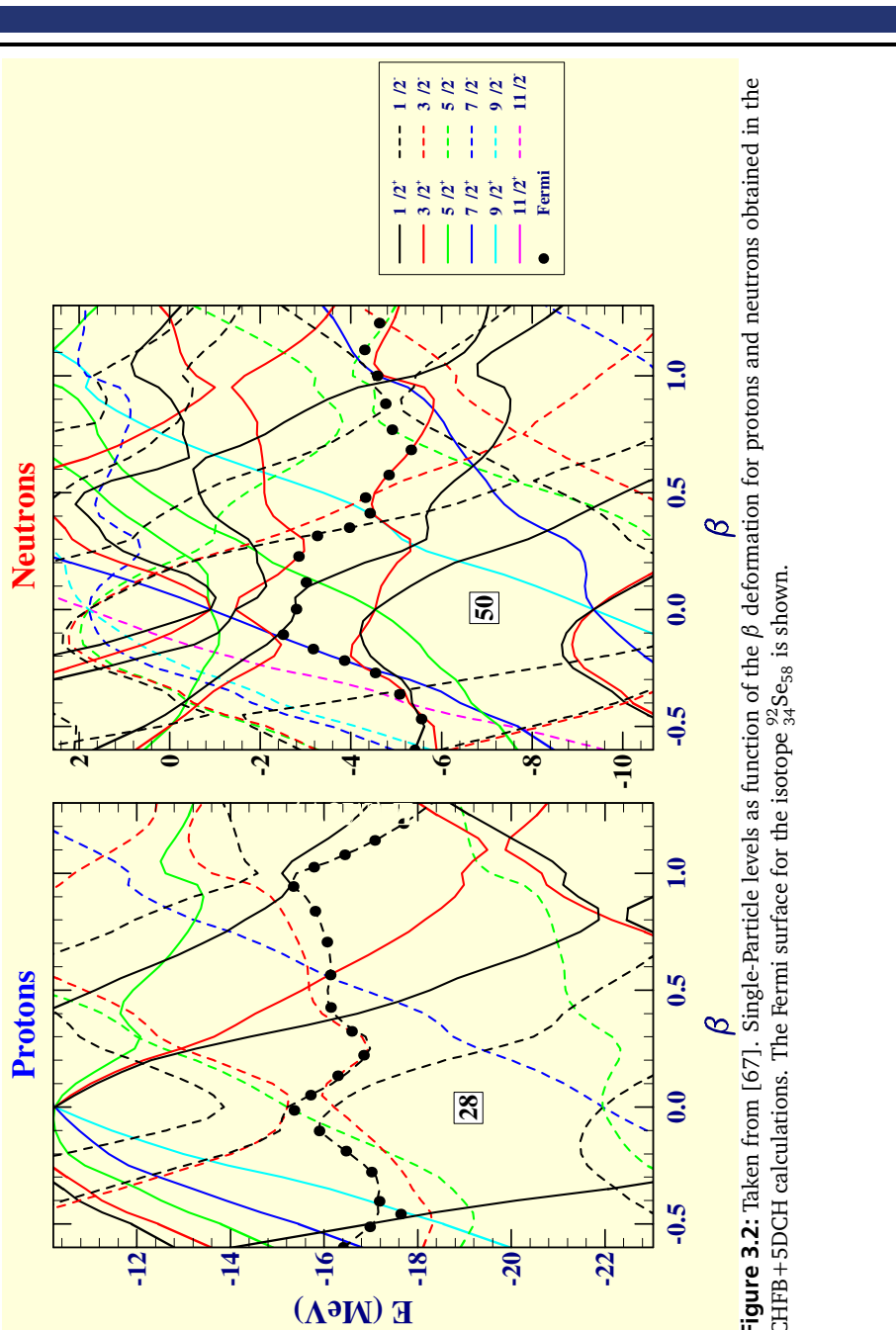


**Figure 3.2:** Taken from [67]. Single-Particle levels as function of the  $\beta$  deformation for protons and neutrons obtained in the CHFB+5DCH calculations. The Fermi surface for the isotope  $^{92}_{34}\text{Se}_{58}$  is shown.

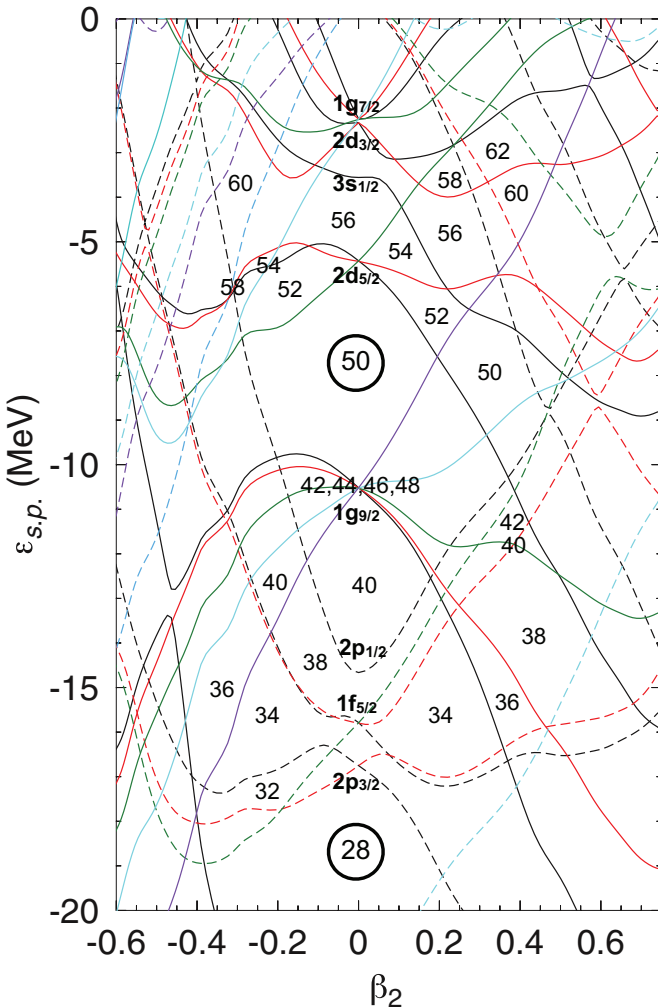


**Figure 3.3:** Taken from [31]. Evolution of neutron single-particle diagrams obtained for  $^{96}\text{Kr}_{60}$  in the PN-VAP SSCM calculations using the Gogny D1S interaction. Neutron numbers in the gaps and level crossings indicate the minima in the axial PES. Continuous (dashed) lines correspond to positive (negative) parity levels and the color code represents the angular momentum projection  $K$ : 1/2 (black), 3/2 (red), 5/2 (green), 7/2 (cyan), 9/2 (purple), 11/2 (light blue).

---

## 4 Fundamentals of $\gamma$ -ray spectroscopy

---

Nuclear spectroscopy is the study of the particles emitted by the atomic nucleus with respect to their energies. The properties of these particles constitute the probes used for testing the predictions of different models and theories proposed to explain the internal dynamics of the nuclear system.

Nuclei populated in excited states have an energy excess eventually released via the spontaneous decay into states of lower energy. When the energy difference between both states involved in the transition is large enough, particles such as p, n,  $\alpha$ ,  $\beta^{+/-}$  can be emitted, leading to a transmutation of the initial nucleus into a different isotope.

However, the transitions between excited states of the same nucleus provide the majority of the information about the nuclear structure. In particular, those close to the Fermi surface or to the 'yrast'-line (a 'yrast' state corresponds the lowest energetic level of a given spin) area of high interest since they are caused by fundamental excitation modes of the nucleus and thus display most clearly the basic properties of a finite nuclear system [68].

These excited states cover a broad energy range roughly of  $\sim 0.01\text{-}10$  MeV and decay mainly via the emission of electromagnetic radiation in the form of  $\gamma$ -rays (sometimes referred as ' $\gamma$  decay' or ' $\gamma$  emission'). Alternatively, the decay can occur via 'internal conversion', where the energy of the transition is transferred to an electron of the atomic shells, or 'internal pair-production', where the transition energy is large enough to form an electron-positron pair. The last of these mechanism always occurs with a probability around  $10^{-3}$  times lower than the  $\gamma$ -decay so its contribution can be neglected for the experiment of this thesis.

In this chapter, the most important features of the electromagnetic nuclear radiation are explained because the characterization of the  $\gamma$ -rays emitted in nuclear transitions are the main part of the data analysis. Also, a discussion of the different mechanisms of nuclear isomerism is presented, to shed some light on the interpretation of the results. A description of the interaction of  $\gamma$ -radiation with matter is shown to understand the interaction with the germanium detectors used.

---

### 4.1 Half-life and branching ratio

---

An ensemble of nuclei in the same excited state undergoes spontaneous decay with a constant probability over time,  $\lambda$ . The decay rate  $dN(t)/dt$  is proportional to the number of nuclei of the ensemble which have not decayed,  $N(t)$ . More precisely,

$$\frac{dN(t)}{dt} = -\lambda N(t). \quad (54)$$

The solution of this Equation is the exponential-decay law

$$N(t) = N_0 \cdot \exp \{-t/\tau\}, \quad (55)$$

with  $\tau = 1/\lambda$  known as the *mean-life* of the excited state, and corresponds to the average amount of time needed to observe the one decay in the ensemble:

$$\frac{\int t \times e^{-t/\tau} dt}{\int e^{-t/\tau} dt} = \tau = \frac{T_{1/2}}{\log(2)}. \quad (56)$$

The value  $T_{1/2}$  is known as the half-life and corresponds to the time needed for the number of nuclei in the ensemble that did not decay to be decreased by half of the initial value  $N_0$ .

The initial state can decay into several final states. Therefore, the total transition rate is

$$\lambda_T = \sum_f \lambda_{i \rightarrow f}, \quad (57)$$

with  $\lambda_{i \rightarrow f}$  the partial decay-rate to the particular final state  $f$ . The fraction of nuclei that decay to this state is known as the branching ratio, and is given by

$$b_{i \rightarrow f} = \frac{\lambda_{i \rightarrow f}}{\lambda_T}. \quad (58)$$

The partial lifetime of each decay channel is related to the lifetime of the initial state simply by

$$\tau_{i \rightarrow f} = 1/\lambda_{i \rightarrow f} = \tau/b_{i \rightarrow f}. \quad (59)$$

## 4.2 Electromagnetic decay of excited states

### 4.2.1 Kinematics of $\gamma$ -ray emission

Consider the emission of a  $\gamma$ -ray due to the transition from an initial excited state of energy  $E_i$ , angular momentum and parity  $I_i, \pi_i$ , to a final state of energy  $E_f$ , and angular momentum and parity  $I_f, \pi_f$ . Due to momentum conservation the  $\gamma$ -ray and the nucleus in the final state  $f$  will have opposite momentum (in the center-of-mass reference frame), the nucleus recoiling with a kinetic energy given by:

$$p_f = p_\gamma = E_\gamma/c \quad \Rightarrow \quad T_f = \frac{p_f^2}{2m_f} = \frac{E_\gamma^2}{2m_f c^2} \quad (60)$$

From the energy conservation of the system:

$$E_i = E_f + E_\gamma + T_f \quad \Rightarrow \quad E_\gamma = (E_i - E_f) - T_f = \Delta E - \frac{E_\gamma^2}{2m_f c^2} \quad (61)$$

Since  $m_f c^2 \sim A \cdot 951$  MeV and  $E_\gamma \sim 1$  MeV for typical nuclear transitions, then  $E_\gamma^2 / 2m_f c^2 \ll 1$ , so that

$$E_\gamma \approx \Delta E. \quad (62)$$

To have an idea of the order of magnitudes of the dimensions involved, consider the wave-length  $\lambda$  of the  $\gamma$ -ray emitted:

$$\begin{aligned} E_\gamma &= \hbar \omega = \hbar \cdot \frac{2\pi}{T} = \hbar \cdot \frac{2\pi}{\lambda/c} = \frac{2\pi \hbar c}{\lambda} \\ \Rightarrow \lambda &= \frac{2\pi \hbar c}{E_\gamma} \approx \frac{6.28 \times 197 \text{ MeV} \cdot \text{fm}}{E_\gamma}. \end{aligned} \quad (63)$$

$\gamma$ -rays have a broad energy range from  $E_\gamma \sim 0.01$  to 10 MeV, leading to wave lengths in the range of  $10^5$  to  $10^3$  fm, respectively. In comparison to the standard parametrization of the nuclear radius,

$$\frac{\lambda}{R_0} \approx \frac{\lambda}{1.2 \cdot A^{1/3} \text{ fm}} \approx \frac{1.2 \cdot 10^3 \text{ MeV} \cdot \text{fm}}{E_\gamma \cdot 1.2 \cdot A^{1/3} \text{ MeV} \cdot \text{fm}} \approx \frac{10^3}{E_\gamma \cdot A^{1/3}}. \quad (64)$$

For a 1 MeV transition and a mid-mass nucleus with  $A \approx 100$  then  $\lambda/R_0 \gg 1$ , reason why the emission of  $\gamma$ -rays is studied within the frame of the long-wavelength approximation.

#### 4.2.2 Multipole expansion

The possible values of angular momentum  $I_\gamma$  carried by the  $\gamma$ -ray emitted in the transition  $i \rightarrow f$  are given by the angular momenta addition rule,

$$|I_i - I_f| \leq I_\gamma \leq |I_i + I_f|. \quad (65)$$

Transitions between states with the same angular momentum  $I_i = I_f$  are not possible via  $\gamma$ -ray emission since a photon must carry at least one unit of angular momentum and cannot be zero, thus, they occur only via internal conversion.

Nuclear transitions are classified according to their *multipolarity*. When a photon carries  $I_\gamma$  units of angular momentum, the transition is said to be  $2^I$ -polar. For instance, for  $I_\gamma = 1$  is called dipolar,  $I_\gamma = 2$  quadrupolar, and so on.

The electromagnetic decay between nuclear states can be understood as the interaction of the electromagnetic radiation field and the nuclear charge and current density. A complete theoretical description is treated in [54, 68]; here only the results are presented.

The interaction of the electromagnetic field with the nucleons during a transition can be expressed as a series of multipolar operators, each one a tensor of rank  $L$  with ‘electric’ and ‘magnetic’ parts

$$\mathcal{O} = \sum_L \sum_{m=-L}^L \sum_{\sigma=E,M} \mathcal{O}(\sigma L) = \sum_{L,m} \{ \mathcal{O}_m(EL) + \mathcal{O}_m(ML) \}, \quad (66)$$

with the following definitions obtained in the long-wavelength limit:

$$\mathcal{O}_m(EL) = \int \rho_N(\vec{r}) r^L Y_{Lm}(\theta, \phi) d^3r, \quad (67)$$

$$\mathcal{O}_m(ML) = \frac{1}{c(L+1)} \int \vec{j}_N(\vec{r}) \{ \vec{r} \times \vec{\nabla} \} r^L Y_{Lm}(\theta, \phi) d^3r, \quad (68)$$

$Y_{Lm}(\theta, \phi)$  the spherical harmonics, and  $\rho_N(\vec{r})$  and  $\vec{j}_N(\vec{r})$  the nuclear charge and current densities, respectively. The expressions of the multipole operators are important since they connect the electric (magnetic) operators with the nuclear charge (current) density, providing some insights on the nuclear structure change occurred during the transition. For instance, a shift of the initial nuclear charge density gives rise to an electric field, and a change in the current density generating a magnetic field. The former can occur for example when a proton has a transition between two different orbitals, and the latter when there is a change in the orientation of a nucleon orbital.

Since the initial and final states have defined parities as well as each of the electric and magnetic components of the operator, the parity selection rules

$$\pi_i \pi_f (-1)^L = 1 \quad \text{for } \sigma = E, \quad (69)$$

$$\pi_i \pi_f (-1)^L = -1 \quad \text{for } \sigma = M, \quad (70)$$

constrains the possible multipolarities of the operators (and therefore of the  $\gamma$ -ray emitted) that can participate in the transition. A list of the lower multipole orders is presented in Table 2, together with the parity selection rule that they obey.

Radiation Type	Name	$L_\gamma$	$\Delta\pi_{if}$
E1	Electric Dipolar	1	$\pi_i = -\pi_f$
M1	Magnetic Dipolar	1	$\pi_i = +\pi_f$
E2	Electric Quadrupolar	2	$\pi_i = +\pi_f$
M2	Magnetic Quadrupolar	2	$\pi_i = -\pi_f$
E3	Electric Octupolar	3	$\pi_i = -\pi_f$
M3	Magnetic Octupolar	3	$\pi_i = +\pi_f$

**Table 2:** Lower multipole orders of electromagnetic nuclear transitions and parity rule they satisfy.

#### 4.2.3 Decay rate and transition probability

The decay rate of the transition  $|\alpha_i I_i\rangle \rightarrow |\alpha_f I_f\rangle$  due to the operator  $\mathcal{O}(\sigma L)$  is given by

$$\lambda_{i \rightarrow f}(\sigma L) = \frac{8\pi(L+1)}{L[(2L+1)!!]^2} \frac{k^{2L+1}}{\hbar} B(\sigma L; i \rightarrow f) \quad (71)$$

where  $k = E_\gamma/\hbar c$ , and

$$B(\sigma L; i \rightarrow f) = \frac{|\langle \alpha_f I_f \parallel \mathcal{O}(\sigma L) \parallel \alpha_i I_i \rangle|^2}{2I_i + 1}, \quad (72)$$

known as the *reduced transition probability*. Conventionally, the electric transition matrix elements are expressed in the units of  $e^2 \cdot \text{fm}^{2L}$ , and the magnetic transition matrix elements in units of  $\mu_N^2 \cdot \text{fm}^{2L-2}$ , where  $\mu_N$  corresponds to the nuclear magneton, given by  $\mu_N = e\hbar/2m_p c = 0.105 \text{ e-fm}$ . The  $B(\sigma L)$  depend on the ‘direction’ of the transition, e.g.

$$B(\sigma L \downarrow) = \frac{2I_f + 1}{2I_i + 1} B(\sigma L \uparrow), \quad (73)$$

with the ‘ $\downarrow$ ’ symbol denoting the  $i \rightarrow f$  transition from a higher to a lower spin, and ‘ $\uparrow$ ’ the  $f \rightarrow i$  case.

In general, a transition can occur via several multipole orders, so the total decay rate is given by

$$\lambda_{i \rightarrow f} = \sum_L \{ \lambda_{i \rightarrow f}(EL) + \lambda_{i \rightarrow f}(ML) \}, \quad (74)$$

for most of the cases, though, only the lowest allowed order of each type contribute considerably to the transition, as it can be seen from the ratio of the rates driven by the multipoles of order  $L$  and  $L + 2$ :

$$\begin{aligned} \frac{\lambda_{i \rightarrow f}(\sigma, L + 2)}{\lambda_{i \rightarrow f}(\sigma, L)} &= \frac{(L + 3)k^{2L+5}/(L + 2)[(2L + 5)!!]^2}{(L + 1)k^{2L+1}/L[(2L + 1)!!]^2} \cdot \frac{B_{i \rightarrow f}(\sigma L + 2)}{B_{i \rightarrow f}(\sigma L)} \\ &= \frac{(L + 3)L[(2L + 1)!!]^2}{(L + 1)(L + 2)[(2L + 5)!!]^2} k^4 \cdot \frac{B_{i \rightarrow f}(\sigma L + 2)}{B_{i \rightarrow f}(\sigma L)} \\ &= \frac{(L + 3)L}{(L + 1)(L + 2)[(2L + 5)(2L + 3)]^2} k^4 \cdot \frac{B_{i \rightarrow f}(\sigma L + 2)}{B_{i \rightarrow f}(\sigma L)} \end{aligned}$$

This quantity is always much less than 1. Consider the lower case  $L = 1$  and a typical energy  $E_\gamma = 1 \text{ MeV}$  (e.g.  $k \sim 1/197 \cdot \text{fm}^{-1}$ ),

$$\begin{aligned} \frac{\lambda_{i \rightarrow f}(\sigma, L + 2)}{\lambda_{i \rightarrow f}(\sigma, L)} &\lesssim \frac{2}{3 \times 35^2} \cdot \frac{1}{197^4} \cdot \frac{B_{i \rightarrow f}(\sigma L + 2)}{B_{i \rightarrow f}(\sigma L)} \\ &\lesssim 3.6 \cdot 10^{-13} \cdot \frac{B_{i \rightarrow f}(\sigma L + 2)}{B_{i \rightarrow f}(\sigma L)} \ll 1. \end{aligned}$$

A very rough estimate [68] reveals that when the lowest allowed multipolarity is of electric type, all higher possible multipoles (e.g. the ones that satisfy the same parity selection rule) can be neglected,

$$\frac{\lambda_{i \rightarrow f}(M, L+1)}{\lambda_{i \rightarrow f}(E, L)} \approx 10^{-8}, \quad (75)$$

while in case that the lowest allowed multipolarity is of magnetic type the next higher possible multipole (which is of electric type) may have to be considered since

$$\frac{\lambda_{i \rightarrow f}(E, L+1)}{\lambda_{i \rightarrow f}(M, L)} \approx 10^{-2}. \quad (76)$$

The expressions for the transition rates of the lower multipole orders are given in Table 3, for  $E_\gamma$  evaluated in MeV.

$\sigma L$	$\lambda_{i \rightarrow f}(\sigma L) (s^{-1})$	$\sigma L$	$\lambda_{i \rightarrow f}(\sigma L) (s^{-1})$
E1	$1.59 \times 10^{15} E_\gamma^3 B(E1)$	M1	$1.76 \times 10^{13} E_\gamma^3 B(M1)$
E2	$1.22 \times 10^9 E_\gamma^5 B(E2)$	M2	$1.35 \times 10^7 E_\gamma^5 B(M2)$
E3	$5.67 \times 10^2 E_\gamma^7 B(E3)$	M3	$6.28 \times 10^1 E_\gamma^7 B(M3)$
E4	$1.69 \times 10^{-4} E_\gamma^9 B(E4)$	M4	$1.87 \times 10^{-6} E_\gamma^9 B(M4)$

**Table 3:** Transition rates for some low multipole orders [54].

#### 4.2.4 Weisskopf estimates

The Weisskopf estimates are a useful criterion to determine the strength of a nuclear transition at a given multipole order in comparison to the situation where a single nucleon would have caused the transition. The basic assumption is that during the transition the nucleus remains inert as a core except for a nucleon that changes between two single-particle orbitals whose radial wave function is approximated by a constant. The reduced transition probabilities for magnetic and electric types are given by [54]

$$B_{Weiss.}(E\lambda) = \frac{1}{4\pi} \left[ \frac{3}{\lambda + 3} \right]^2 R_N^{2\lambda} \quad e^2 \text{fm}^{2\lambda}; \quad (77)$$

$$B_{Weiss.}(M\lambda) = \frac{10}{\pi} \left[ \frac{3}{\lambda + 3} \right]^2 R_N^{2\lambda-2} \quad \mu^2 \text{fm}^{2\lambda+2}, \quad (78)$$

with  $R_N = 1.23A^{1/3}$  the standard parametrization for the nuclear radius. The Weisskopf estimates of single particle transition rates for the lowest multipole orders can be found using Equation (71) and are shown in Table 4, and their behaviour in the range 0.01-5 MeV for  $A = 92$  is shown in Figure 4.1.

$L$	$\lambda_{Weiss.}(EL) (s^{-1})$	$\lambda_{Weiss.}(ML) (s^{-1})$
1	$1.0 \times 10^{14} A^{2/3} E_\gamma^3$	$5.6 \times 10^{13} E_\gamma^3$
2	$7.3 \times 10^7 A^{4/3} E_\gamma^5$	$3.5 \times 10^7 A^{2/3} E_\gamma^5$
3	$3.3 \times 10^1 A^2 E_\gamma^7$	$1.6 \times 10^1 A^{4/3} E_\gamma^7$
4	$1.1 \times 10^{-5} A^{8/3} E_\gamma^9$	$4.5 \times 10^{-6} A^2 E_\gamma^9$

**Table 4:** Weisskopf single-particle rates for the lowest multipole orders [1].

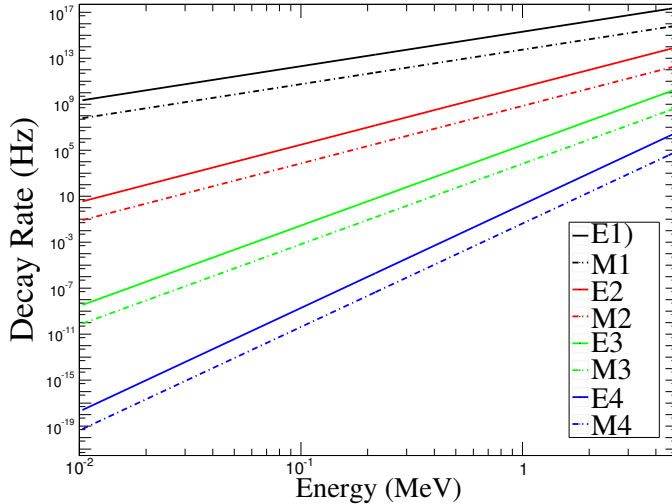


**Figure 4.1:** Weisskopf rate estimates for  $0.01 \leq E_\gamma \leq 10$  MeV, and  $A=92$ .

Several conclusions can be drawn from these estimates. First at all, the transition rates of levels with same parity are such that

$$\lambda_{W.u.}(E1) \gg \lambda_{W.u.}(M2) \gg \lambda_{W.u.}(E3) \gg \dots,$$

$$\lambda_{W.u.}(M1) \gg \lambda_{W.u.}(E2) \gg \lambda_{W.u.}(M3) \gg \dots$$

When the experimental value of a transition is such that  $\lambda_{exp}(\sigma L) \gg \lambda_{W.u.}(\sigma L)$  then the transition is more likely to be driven by several nucleons, on the other hand, when  $\lambda_{exp}(\sigma L) \ll \lambda_{W.u.}(\sigma L)$ . The small matrix element of the reduced transition probability indicates that the overlap of the wavefunctions between the initial and final states is very low, so a drastic change in the inner structure occurs.

## 4.2.5 Internal Conversion

The internal conversion is a competing process to  $\gamma$  emission consisting of the electromagnetic interaction of an excited nucleus with an electron in the atomic shells. The excitation energy is transferred directly to the electron without the emission of a photon so that the electron is emitted from the atom with an energy

$$E_{IC} = E_i - E_f - E_b, \quad (79)$$

with  $E_b$  the binding energy of the electron, which differs for each atomic-shell. Therefore, conversion electrons can exhibit several energy peaks for the same nuclear transition, being the inner shells the ones that contribute considerably to the process, namely, the K, L and M shells.

The competition between internal conversion and  $\gamma$  decay is characterized by the *internal conversion coefficient*:

$$\alpha_{IC} = \frac{\text{rate of internal conversion decays}}{\text{rate of } \gamma\text{-ray decays}}. \quad (80)$$

Furthermore, the total decay rate for the transition  $i \rightarrow f$  must be re-defined as the sum of the  $\gamma$ -ray and internal conversion channels:

$$\lambda_{i \rightarrow f} = \lambda_\gamma + \lambda_{IC} = (\alpha_{IC} + 1)\lambda_\gamma. \quad (81)$$

The total conversion coefficient is the sum of the partial conversion coefficients for each shell (and sub-shell),

$$\alpha_{IC} = \alpha_K + \alpha_L + \alpha_M + .. \quad (82)$$

A non-relativistic estimation of the conversion coefficient for different electric and magnetic multipoles is given by [1]

$$\alpha_{IC}(EL) \approx \frac{Z^3}{n^3} \cdot \frac{L}{L+1} \left[ \frac{e^2}{4\pi\epsilon_0\hbar c} \right]^4 \left[ \frac{2m_e c^2}{E_\gamma} \right]^{L+5/2} \quad (83)$$

$$\alpha_{IC}(ML) \approx \frac{Z^3}{n^3} \cdot \left[ \frac{e^2}{4\pi\epsilon_0\hbar c} \right]^4 \left[ \frac{2m_e c^2}{E_\gamma} \right]^{L+3/2} \quad (84)$$

with  $Z$  the atomic number,  $n$  the main quantum number of the electron wavefunction, and  $\alpha = e^2/4\pi\epsilon_0\hbar c \approx 1/137$ , the fine structure constant. These expressions (though not accurate as the electron should be treated relativistically) show that internal conversion competes strongly with  $\gamma$ -ray emission at high multipole orders or low transition energies, and is proportional to  $Z^3$ , becoming important for heavier nuclei. The calculation of the conversion coefficient for Selenium nuclei was evaluated using BrIcc [69], a widely used program developed to help ENSDF evaluators to calculate conversion coefficients using the best available theoretical data, see Figure 4.2.

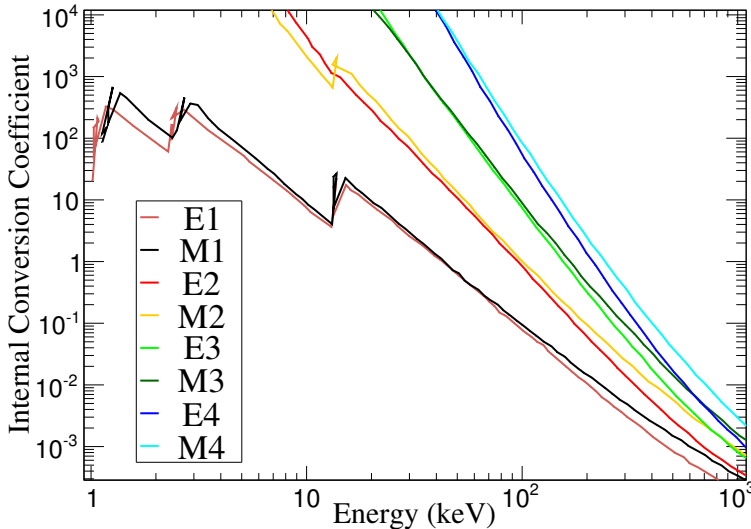


**Figure 4.2:** Internal Conversion coefficient for  $Z=34$  nuclei at lower multipolarities. Data from [69].

### 4.3 Nuclear Isomerism

Nuclear Isomerism is a phenomenon that has contributed largely to the understanding of the nuclear structure. It refers to the occurrence of an excited nuclear state with a half-life much larger in comparison to a typical nuclear state, which is on the order of  $\lesssim 100$  ps. Though there is no formal minimum value to establish a distinction, states with half-lives larger than few nanoseconds are considered to be isomeric. This range extends over very different orders of magnitude, from  $\sim 500$  ns in case of the  $I^\pi=49/2^+$  state of  $^{147}\text{Gd}$ , up to  $>10^{16}$  years for the  $I^\pi=9^+$  state of  $^{180}\text{Ta}$ , the largest isomeric half-life known to date [70].

No nuclear model can predict accurately neither the existence nor the half-life of an isomeric state over extended regions of the nuclide chart. However, predictions in specific mass-regions and accurate explanations further to the experimental discovery of isomeric states for a vast range of nuclei have been performed, in many cases proving the existence of the nuclear shell structure and the nuclear deformation unambiguously. As it has been shown in Sections 4.1 and 4.2.3 the half-life and decay rate of a nuclear state are inverse to each other, thus, for a transition decaying mainly via a particular multipole order it is satisfied that

$$\tau \sim \frac{1}{\Delta E^{2\lambda+1} \cdot |\langle \alpha_f I_f \parallel \mathcal{O}(\sigma\lambda) \parallel \alpha_i I_i \rangle|^2}. \quad (85)$$

From this Equation, it is clear that the transition matrix element, determined by the internal structure, is directly related to the lifetime. Pinning down the causes leading to isomerism is a difficult task since many factors influence the half-life of a state. For example, when the lowest allowed nuclear transition in the energy spectra of a nucleus corresponds to a high multipole order, a long half-life results simply as a consequence of the natural transition rate of electromagnetic decays. Also, in many cases (though not always) a long lifetime results when the energy difference between the two states of the transition,  $\Delta E$ , is very small. Other less serendipitous causes of isomerism showing a systematics over regions of the nuclide chart are known for the heavy  $A=160$ -190 mass region, or the  $Z\sim 40$ ,  $N\sim 60$  region. A complete and comprehensive review of nuclear isomerism is presented in [71], and other works such as [70–73]. Here the main ideas of the different types of isomeric states known so far are presented, namely, spin-traps, seniority isomers, shape isomers, and  $K$ -trap isomers.

---

#### 4.3.1 Spin-traps

This type of isomerism already mentioned occurs when the lowest multipole order transition allowed by the angular momentum addition rules has a slow decay-rate leading to a large half-life. For this kind of isomers the rules of angular momentum are conserved; their occurrence is relatively random since it is required that no other states ‘opening’ faster decay branches are close in the excitation energy spectrum of the nucleus. An example of a spin-trap isomer is the  $^{180}\text{Ta}^*$  case, where the transition from the  $I = 9$  to the  $I = 1$  ground state with an energy gap of just 75 keV has an associated half-life  $>10^{16}$  years [72].

---

#### 4.3.2 Shape isomers

They occur when there is a secondary minimum in the nuclear potential as a function of the quadrupolar deformation (the absolute minimum corresponds to the ground state). One of the clearest examples corresponds to the 2.2 MeV isomer of  $^{242}\text{Am}$  with  $\tau \sim 14$  ms with a major-to-minor axis ratio about 2:1 [72]. These type of isomers can be known as *fission isomers* when their decay via fission into two lighter nuclei becomes a competitive process to the decay from the isomeric state to the ground state by  $\gamma$ -ray emission.

---

#### 4.3.3 Seniority isomers

Seniority is a concept borrowed from atomic physics referring to the number ‘ $\nu$ ’ of nucleons with angular momentum not coupled to zero. It becomes important in regions of the nuclide chart close to the shell closures, particularly in semi-magic nuclei where only one type of nucleons (either protons or neutrons) are

active. In these regions, the single-particle features of the shell structure dominate over collective phenomena, and the two-body interactions become the strongest first-order residual interaction of the nuclear system. In the simplest scenario, the lowest excited states of these nuclei are considered as  $j^n$  multiplet configurations, e.g. as  $n$  identical active nucleons in a single- $j$  shell while the nucleons of the other type remain inert. These levels will be formed by configurations with the lowest possible seniority, so the ground state is formed coupling all nucleon pairs to  $J = 0$ , therefore  $\nu=0$ ; and the yrast  $J=2, 4, \dots, 2j-1$  levels are formed for seniority  $\nu=2$ . A characteristic energy spectrum is illustrated in Figure 4.3, where it is shown the example of the neutron  $h_{11/2}$  orbital of the Sn isotopic chain.

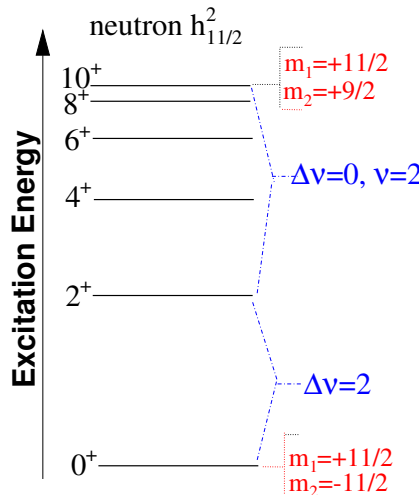


**Figure 4.3:** Schematic energy spectrum of  $\nu=2$  configuration states in the  $h_{11/2}$  orbital for the Sn isotopes. All the transitions for angular momentum  $J \geq 2$  connect states with seniority  $\nu=2$ . However, the  $2_1^+ \rightarrow 0^+$  transition involves the seniority change  $\Delta\nu=2$ , since all the pairs couple in the ground-state.

The decay strength for the E2 transitions between states with same seniority satisfies [11, 74]

$$B(E2; J \rightarrow J-2) \propto \left( \frac{\Omega - n}{\Omega - \nu} \right)^2, \quad (86)$$

where  $2\Omega=2j+1$  corresponds to the maximum possible occupancy of the  $j$ -orbital. This term becomes very small at mid-shell when  $n \rightarrow \Omega$ , hence leading to a long isomeric half-life by virtue of Equation 85. In cases such as the one shown in Figure 4.3, the  $\nu=2$  seniority isomer is commonly referred to the transition between the higher-spin states  $10^+ \rightarrow 8^+$  in the multiplet, which is reinforced by the

weak B(E2) and the small energy gap. This isomeric state remarkably exists for the Sn chain between the  $N=50$  and  $N=82$  magic numbers [71].

#### 4.3.4 *K*-traps

To understand isomerism caused by *K*-traps, consider an axially symmetric deformed nucleus with seniority different than zero. The angular momentum of the unpaired particles has a total value  $j_1 + j_2 = J \neq 0$ , which in turn couples with the angular momentum contribution from the nuclear collective rotation  $\mathbf{R}$ , leading to a total *nuclear spin*  $\mathbf{I}$ , see Figure 4.4.

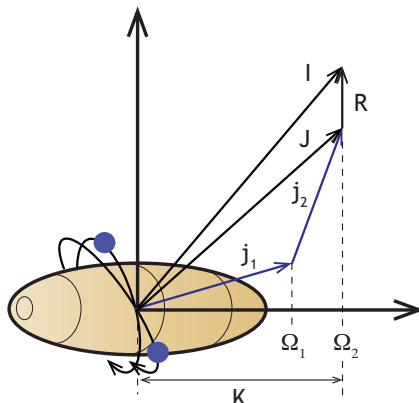


**Figure 4.4:** Schematic picture of the angular momentum coupling between single-particle and collective motion occurring in axially deformed nuclei. Source [71].

For fixed values of  $J$  associated rotational bands can appear, leading to states of different  $\mathbf{R}$ , with the respective bandhead characterized by  $\mathbf{I}=J$  (when  $\mathbf{R}=0$ ). The projection of the total angular momentum in the symmetry axis for each band is given by

$$K^{\pi} = \sum_i \Omega_i^{\prod_j \pi_j} \quad (87)$$

with the bandhead state having an excitation energy dominated by the breaking of pairs so that (see Section 2.1.1).

$$E^* \approx \sum_i \sqrt{(\epsilon_i - \epsilon_F)^2 + \Delta^2} \quad (88)$$

where  $\epsilon_i$  is the single-particle energy,  $\epsilon_F$  the Fermi energy, and  $\Delta$  the pairing energy gap, directly related with the mass difference with respect to odd-even neighbouring isotopes [71].

A transition between states with different K-values is, in principle, only possible when the multipolarity of the decay radiation  $\lambda$  is at least as large as the change in the K-value,  $\lambda \geq \Delta K$  [72]. For large changes of K, the allowed transition rates will inevitably be very slow. However, it has been observed for several cases that these isomeric transitions decay faster than expected via  $\gamma$ -rays with lower multipolarities than the allowed ones by the K-selection rule. These ‘forbidden’ transitions, hindered rather than literally forbidden, exist due to additional symmetry-breaking processes not considered in the initial picture of the nuclear dynamics (e.g. higher order asymmetric deformations, K-mixing due to Coriolis coupling, etc.).

### Hindrance and Forbiddenss

The ‘degree of forbiddenss’  $\nu$  of a transition<sup>4</sup> is defined as the magnitude of the mismatch between the multipole order of the observed transition and  $\Delta K$  [75],

$$\nu = \Delta K - \lambda. \quad (89)$$

The ‘hindrance factor’, defined as the ratio between the lifetimes of the  $\gamma$ -ray decay observed and the one obtained from a Weisskopf single-particle estimate,

$$F = \frac{\tau^\gamma}{\tau^W} = \frac{B_W(\sigma\lambda)}{B_\gamma(\sigma\lambda)}, \quad (90)$$

is a first indication to distinguish a K-forbidden isomer from other types [73], since a hindered transition is expected to have a decay-strength much lower in comparison to the single-particle case (otherwise it is not likely to be forbidden or even isomeric) so  $F \gg 1$ .

For K-forbidden decays, the ‘reduced hindrance’ is defined as

$$f_\nu = (F)^{1/\nu} = (\tau^\gamma/\tau^W)^{1/\nu}, \quad (91)$$

and it evaluates the hindrance per degree of K-forbiddenss. In an ideal situation,  $f_\nu$  should scale such that it would be independent of  $E_\gamma$ ,  $\sigma\lambda$ , and  $\nu$ ; the experimental evaluation of this factor has shown that  $f_\nu \sim 20\text{-}200$  for a wide range of values of  $\nu$  and  $\lambda$  (though several exceptions are found to specific additional reasons), so this remains as one strong criterion that suggest K-isomeric decays [70, 71, 73, 75].

### Nilsson Levels and Multi quasi-particle states

The existence of a K-isomer relies not only on an approximate good axial-deformation so that the use of  $K$  as a quantum number is valid, but also in the existence of an excited state with a high- $K$  value. Such state is created from the coupling of at least two quasi-particles occupying different Nilsson levels. Therefore, a high- $K$  state can be formed only for nuclei whose Fermi surface is close to Nilsson levels with  $K$  values which can couple to a high- $K$ . This condition con-

<sup>4</sup> Unfortunately, the widely used symbol in the literature to denote forbiddenss is the same for seniority

strains the possible regions of the nuclide chart where  $K$ -isomerism can happen since high- $K$  Nilsson levels stem from high- $j$  spherical-shell orbitals, which are normally occupied by mid or high masses. This has been experimentally corroborated for the  $K$ -isomer cases so far known [76].

The most complete calculations to date for the excitation energies of this multi quasi-particle states add two ingredients extra to the calculation of Nilsson diagrams: The ‘blocking effect’, where singly occupied quasiparticle orbitals prevent the scattering of pairs into those orbitals, leading to a decrease of the pairing correlation energy as the number of quasiparticles increase. Second, the relevance of the interactions between quasiparticles favouring some  $K$ -couplings depending on the relative orientation of the nucleon intrinsic spins [73]. For instance, the two quasi-particle states of even-even nuclei prefer the anti-parallel coupling of the intrinsic spins since this situation gives more binding than the parallel coupling case [11].

Despite the inevitable model dependence on the quantitative calculations of the excitation energies of the high- $K$  *multi-quasiparticle* states (a specific nuclear deformation and potential must be assumed to calculate the Nilsson diagrams, and specific parametrizations must be used for the pairing interaction accounting for blocking), there are usually a very few (or unique) combination of orbitals that lead to the right spin/parity assignments needed to explain the isomeric decay. This motivates the use of  $K$ -isomers to probe the microscopic orbital structure close to the Fermi surface, as well as the quadrupolar deformation of a nucleus.

### K-isomer example: The $^{180}_{72}\text{Hf}$ case

To illustrate how the ideas discussed previously are used on real data, consider the  $^{180}_{72}\text{Hf}$  case. It has some historical relevance since it was the first case where the violation of the  $K$ -selection rule was observed, and triggered the understanding of the collective nuclear structure, as highlighted by A. Bohr in his Nobel Prize lecture (1975) [53].

The isomeric state  $K^\pi = 8^-$ ,  $I = 8$  at 1.1 MeV decays via an  $E1$  58 keV transition to the  $I^\pi = 8^+$  state of the  $K = 0$  ground state band with a half-life of 5.5h. This transition is highly forbidden since  $\nu = 8 - 1 = 7$ . It leads to a change in the orientation, but not magnitude, of the angular momentum, see Figure 4.5. The hindrance factor as well as the reduced hindrance suggest a highly  $K$ -hindered decay:

$$F = \frac{T_{1/2}^\gamma}{T_{1/2}^W} = \frac{(1 + \alpha_{IC})T_{1/2}}{T_{1/2}^W} = \frac{(1 + 0.29)5.5 \times 3.6 \times 10^3}{1.1 \times 10^{-12}} \approx 10^{16} \gg 1,$$

$$f_\nu = F^{1/\nu} = (2.3 \times 10^{16})^{1/7} \approx 2.17 \times 10^2.$$

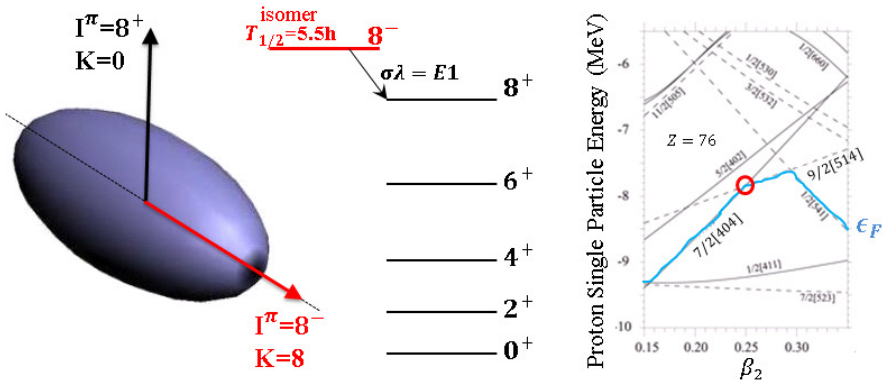


**Figure 4.5:** Schematic picture of the  $K$ -forbidden isomer decay in  $^{180}\text{Hf}$ , and Nilsson single-particle energies for protons as a function of the quadrupolar deformation  $\beta_2$ , with  $\beta_4 = -0.035$  and axial symmetry ( $\gamma = 0^\circ$ ). The single-particle Fermi surface  $\epsilon_F$  is highlighted in blue, and the crossing point of the  $7/2^+[404]$  and  $9/2^-[514]$  levels that generate the  $8^-$  isomeric state is marked in red. Modified from [73].

This transition is however much faster than the  $K$ -allowed  $M8$  transition to the  $I^\pi = 0^+$  ground state, not observed to date [73]. The possible spin/parity values of the  $K$ -isomeric state are deduced from the Nilsson single particle levels for protons. For a quadrupolar deformation of  $\beta_2 \sim 0.26$ , the  $7/2^+[404]$  and  $9/2^-[514]$  levels are close to each other and define the Fermi surface, see Figure 4.5. Therefore, the lowest two quasi-particle state that can create the  $K=8$  isomeric state is obtained at this deformation value, since the only excitation energy needed is spent on breaking a pair. Two states can be created since the possible couplings are  $K = \Omega_1 \pm \Omega_2 = 8$  or 1. Nevertheless, the  $K^\pi = 8^-$  isomer is the one observed, since the  $7/2^+[404]$  proton is ‘spin-down’, and the  $9/2^-[514]$  proton is ‘spin-up’. This spin coupling is energetically favoured for identical single particles in comparison to the  $K^\pi = 1^-$  spin-up of the same two protons [73].

For this almost ideal example of  $K$ -isomerism the comparison of the observations with single-particle calculations allow to track down unambiguously the orbitals near the Fermi surface and the magnitude of the quadrupolar deformation. In many other cases, however, sophisticated corrections have to be included since the mechanisms responsible of the isomerism may not be isolated.

#### 4.4 Interaction of $\gamma$ -rays with matter

$\gamma$  radiation interacts with matter mainly through three different mechanisms, namely, Photo-electric interaction, Compton scattering, or Pair production:

## Photo-electric interaction

It occurs when an incoming photon transfers all its energy to a bound electron of an atom in the material. The electron is ejected with a kinetic energy  $E_{e^-} = E_\gamma - E_b$ , where  $E_\gamma$  is the photon energy and  $E_b$  the binding energy of the electron. The interaction ionizes the atom with a free vacancy in the shell of the photoelectron emitted, and this vacancy is rapidly occupied by one of the electrons from other shells in the atom or by surrounding electrons from the material. Both cases lead to the release of the atomic excitation energy mainly via the emission of characteristic X-rays or Auger electrons [77]. The photoelectric absorption is the dominant interaction process of lower  $\gamma$ -rays, e.g.  $E_\gamma \lesssim 200$  keV, and it is enhanced by materials with high atomic number  $Z$ . A rough approximation for the interaction probability per atom is given by [78]

$$P_{phot} \cong k \cdot \frac{Z^n}{E_\gamma^{3.5}} \quad (92)$$

with  $k$  a constant,  $n$  a factor that varies between 4 and 5 over the  $\gamma$ -ray region of interest. The probability decreases strongly with the photon energy but does not reflect some discontinuities of the cross-section, since it increases sharply when the incoming  $\gamma$ -ray matches the ionisation energy of an atomic shell of the material. The energy and momentum conservation cannot be simultaneously satisfied for a photo-electric interaction with a free electron, so this process only occurs for bounded electrons.

## Compton scattering

It occurs when the incoming  $\gamma$ -ray collides elastically with an electron of the material (either free or bound) and then it is scattered at an angle  $\theta_c$  with a lower energy. The recoil electron receives an energy equal to the energy lost of the incoming  $\gamma$ -ray. The energy of the outgoing photon is given by

$$E'_\gamma = \frac{E_\gamma}{1 + \frac{E_\gamma}{m_e c^2} (1 - \cos \theta_c)}$$

where  $m_e c^2 = 511$  keV is the rest mass of the electron. The energy of the outgoing  $\gamma$ -ray decreases for larger scattering angles, in a similar manner of a 2-body elastic collision in classical mechanics. This interaction mechanism is predominant for an extensive range of  $\gamma$ -ray energies, e.g.  $\sim 0.2\text{-}3$  MeV.

The angular distribution of scattered  $\gamma$ -rays is given by the *Klein-Nishina Formula* for the differential scattering cross section  $d\sigma/d\Omega$  [77]:

$$\frac{d\sigma}{d\Omega} = Z r_0^2 \left( \frac{1}{1 + \alpha(1 - \cos \theta)} \right)^2 \left( \frac{1 + \cos^2 \theta}{2} \right) \left( 1 + \frac{\alpha^2(1 - \cos \theta)^2}{(1 + \cos^2 \theta)[1 + \alpha(1 - \cos \theta)]} \right), \quad (93)$$

where  $\alpha = E_\gamma/m_e c^2$  and  $r_0$  the classical electron radius.  $\gamma$ -rays with higher energies have a much lower probability to be scattered at large angles in comparison with low-energy ones.

### Pair production

For incident photon energies higher than  $2 \cdot m_e c^2 = 1.022$  MeV, the production of an electron-positron pair becomes possible. The cross section of this process remains very low for a large range of incident energies, and only is important for high-energy  $\gamma$ -rays of several MeV. The combined kinetic energy of the pair is equal to the energy of the incident photon minus the 1.022 MeV of energy invested in the pair production. Since this process occurs in a material, the positron emitted will annihilate with an electron and normally emit a pair of 511 keV photons.

### Linear attenuation coefficient

The relative importance of the processes described before for materials with different atomic numbers and  $\gamma$ -ray energies is illustrated in Figure 4.6.

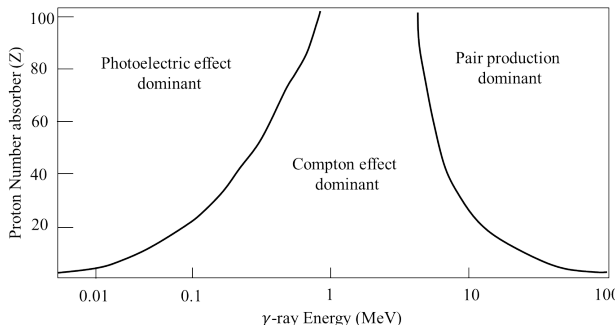


**Figure 4.6:** Relative importance of the three major types of  $\gamma$ -ray interaction with matter. The lines represent the values of  $Z$  and  $E_\gamma = h\nu$  for which the probability of the two neighbouring effects is equal. Source: [79].

The total interaction probability per path length of a  $\gamma$ -ray in a material is known as the *linear attenuation coefficient*. It simply corresponds to the addition of the interaction probabilities of each of the three processes described:

$$\mu_T = \mu_{phot.} + \mu_{Compt.} + \mu_{P.P.} \quad (94)$$

---

## 5 Experiment setup

---

As it was mentioned in Section 1.1, the experiment analyzed in this thesis was conducted at the Radioactive Isotope Beam Factory (RIBF) [80] at the RIKEN Nishina Center [22] as part of the second campaign of the SEASTAR scientific program [21], which focused on the search of the first excited states of nuclei in the  $30 \leq Z \leq 36$ ,  $54 \leq N \leq 62$  neutron-rich mass region. An overview of the main steps and the key devices of the experiment are shown in Figure 5.1. The discussions of the different techniques and machines used are presented in the subsections.

Initially, a primary beam of  $^{238}\text{U}$  with a kinetic energy of 345 MeV/nuc. was provided by the RIBF accelerator complex. It impinged on a  $^9\text{Be}$  target producing neutron-rich exotic nuclei that were collected by the superconducting BigRIPS fragment separator [81]. This machine allowed to select and identify the nuclei of interest on an event-by-event basis from the rest of the fragments by tuning conveniently the different magnets of the spectrometer. In particular for the dataset analysed, the BigRIPS magnets were tuned to transmit mainly  $^{94,95}_{35}\text{Br}$  during a measuring time of about 33 hours, with average intensities of 182 and 50 particles per second, respectively [24].

The combination of the in-flight fission technique with the magnetic separation of BigRIPS produced a radioactive beam cocktail of exotic nuclei from the mass region of interest. This secondary beam impinged on a 99(1)-mm liquid hydrogen target producing neutron-rich Selenium nuclei via knockout reactions. For instance,  $^{92}\text{Se}$  was produced mainly via the  $^{35}\text{Br}(p, 2pn)^{92}_{34}\text{Se}$  reaction and  $^{94}\text{Se}$  via the  $^{95}\text{Br}(p, 2p)^{94}_{34}\text{Se}$ . The knockout of few nucleons off the incoming-beam isotopes led to the population of the ejectiles in excited states. Short-lived states ( $\tau \lesssim 100$  ps) decayed promptly after the reaction, with the ejectiles still inside the target volume. These decays were study via the detection of the  $\gamma$ -rays emitted, using the NaI(Tl) detector array DALI2 [82] placed around the target. Since the emission occurs in-flight, a Doppler correction was conducted using the MINOS device, discussed in Section 5.5.

The velocity and identity of the ejectiles were measured with the ZeroDegree mass spectrometer [80], placed at  $0^\circ$  in the forward beam direction after MINOS. ZeroDegree uses similar methods as BigRIPS for the transmission and particle identification. After crossing ZeroDegree, the nuclei were stopped at the F11 focal plane, where they were implanted into silicon layers of the AIDA detector [83]. In average, the times of flight between the production and reaction targets to the stopper were  $\sim 650$  and  $\sim 380$  ns, respectively. The exotic nuclei produced can also be populated into isomeric states enough long-lived to decay after implantation. These states were studied using a decay-spectroscopy setup at F11.

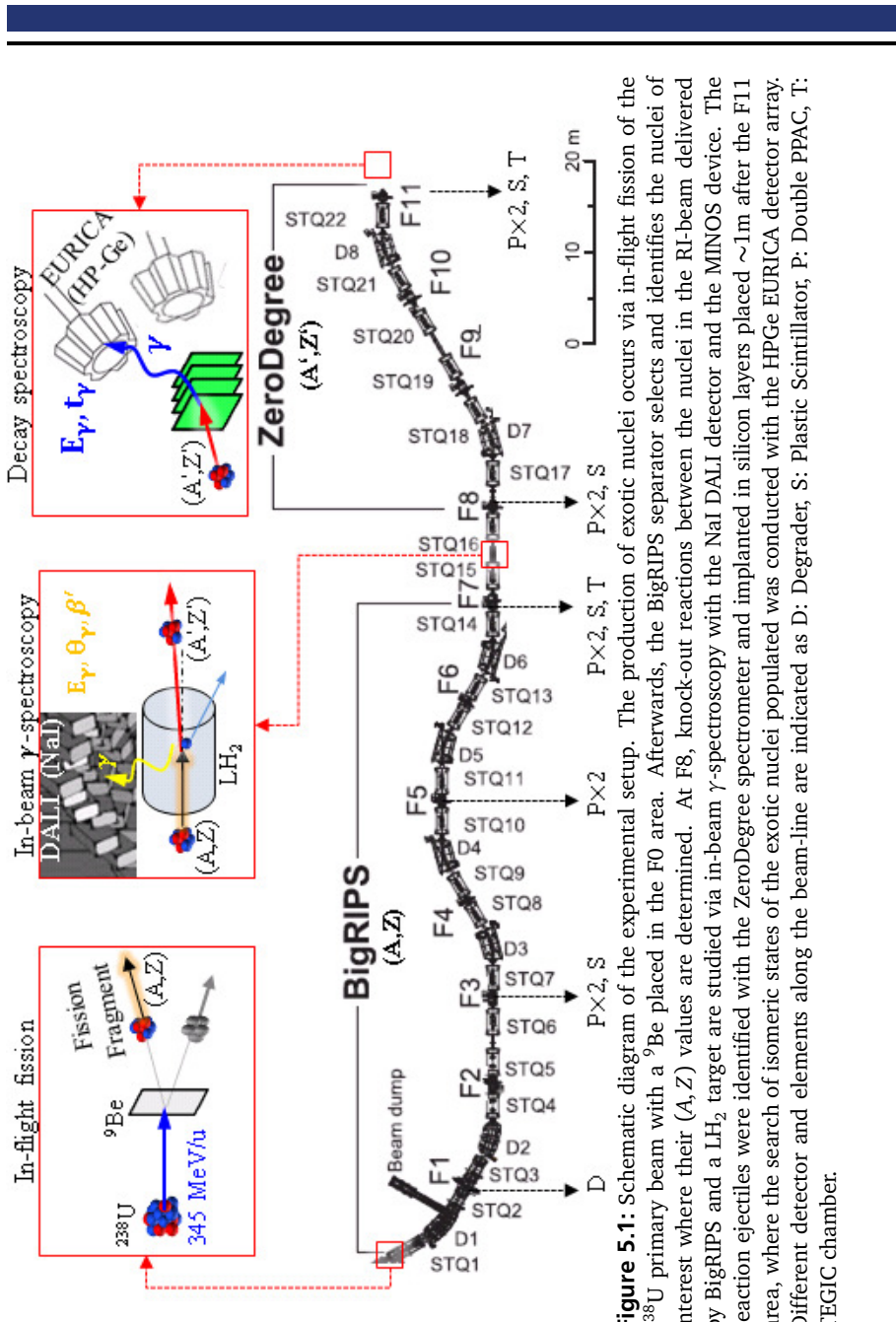


**Figure 5.1:** Schematic diagram of the experimental setup. The production of exotic nuclei occurs via in-flight fission of the  $^{238}\text{U}$  primary beam with a  $^{9}\text{Be}$  placed in the F0 area. Afterwards, the BigRIPS separator selects and identifies the nuclei of interest where their  $(A, Z)$  values are determined. At F8, knock-out reactions between the nuclei in the RI-beam delivered by BigRIPS and a  $\text{LH}_2$  target are studied via in-beam  $\gamma$ -spectroscopy with the NaI DALLI detector and the MINOS device. The reaction ejectiles were identified with the ZeroDegree spectrometer and implanted in silicon layers placed  $\sim 1\text{m}$  after the F11 area, where the search of isomeric states of the exotic nuclei populated was conducted with the HPGe EURICA detector array. Different detector and elements along the beam-line are indicated as D: Degrader, S: Plastic Scintillator, P: Double PPAC, T: TEGIC chamber.

The  $\gamma$ -rays emitted following the isomer decay were studied with the EURICA detector array (EUROBALL-RIKEN Array) [84], a set of 84 HPGe crystals belonging to the former EUROBALL array. The energies ( $E_\gamma$ ) and times ( $t_\gamma$ ) of the hits in EURICA were recorded during a 100- $\mu$ s time window that was triggered when an ion crossed a plastic scintillator located  $\sim$ 1 m upstream of implantation. Therefore, a correlation  $\gamma$ -particle was achieved on an event-by-event basis. The measurement of energy and time allowed not only measuring the half-life of an isomeric state, but also a high energy-resolution analysis of the low-energy excitation schemes of the exotic nuclei involved. These measurements were not only simultaneous but also complementary to the in-beam spectroscopy performed at F7, which is sensitive only to prompt decays with better efficiency but lower energy-resolution.

---

## 5.1 Production of radioactive ion beams (RIB)

---

The RIBF facility currently provides the most intense RI-beams in the world at energies of hundreds of MeV/nuc. over a large set of atomic masses, from light to heavy ones [22]. It comprises the accelerator complex providing stable beams with kinetic energies up to 345 MeV/nuc., the production target where exotic nuclei are produced via the projectile fragmentation of heavy ions or the in-flight fission of uranium ions, and the BigRIPS superconducting fragment separator used to separate and identify the nuclei of interest.

---

### 5.1.1 RIKEN accelerator complex

---

A schematic view of the accelerator complex can be seen in Figure 5.2. A beam of  $^{238}\text{U}$  ions was obtained after a 28 GHz microwave from a gyrotron was injected into the SuperConducting Electron Cyclotron Resonance (SC-ECR) ion source. The ions are stripped up to 35+ charge state in the RILAC (RIKEN Heavy-ion Linac) linac accelerator, where they are accelerated with 6 frequency-tunable cavities that provide a total acceleration voltage of 16 MV [85]. The beam is injected afterwards in the RRC (RIKEN Ring Cyclotron), delivered then to the fRC (fixed-frequency ring cyclotron), and finally to the IRC (Intermediate Ring Cyclotron). Each step boosts the beam energy successively to 11 MeV/nuc., 51 MeV/nuc., and 115 MeV/nuc. [22]. Each of these cyclotrons has four sector magnets and two RF cavities for accelerating the beam. At the injection and exit of the fRC, electron strippers were placed to increase the charge state of the beam ions up to 71+ and 88+, respectively [60].

In the final acceleration stage, the beam is sent to the SRC (SuperConducting Ring Cyclotron) where it reaches up to 345 MeV/nuc. of kinetic energy. This device contains six superconducting sector magnets specially developed for the RIBF and achieves a bending power of (8 Tm). With a total weight of 8300 Tons, it has so

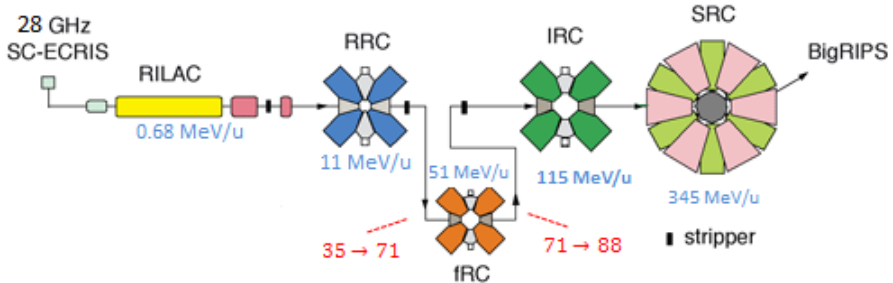


**Figure 5.2:** Schematic view of the of accelerator complex elements used in the experiment. Modified from [22].

much iron that provides it with a self-shielding capacity for magnetic shield and radiation leakages protecting the facility surroundings [86].

### 5.1.2 In-flight fission of $^{238}\text{U}$

The mechanism used to produce exotic nuclei depends on the mass region of interest. For example, very proton-rich nuclei are produced with fusion-evaporation reactions, since the final products have a mass, neutron, and proton numbers close to the sum of the ones of projectile and target. In the case of neutron-rich nuclei, the projectile fragmentation and in-flight fission methods are widely used. In both processes, a heavy-ion projectile collides against a lower mass target at rest leading to the projectile break-up. However, the distribution of mass, proton-to-neutron ratio, and scattering angle of the products differ considerably. In projectile fragmentation, the products are projectile-like residues after several nucleons are grasped during a peripheral collision with the target. This process exhibits a mass distribution that peaks at a value close but lower than the projectile mass, and decreases rapidly with mass number. Due to the high initial momentum of the projectile, the products are emitted in a narrow cone in the forward direction to the incident trajectory of the beam. In the case of in-flight fission, the projectile normally breaks into two products, one of them slightly smaller than the other, leading to an asymmetric mass distribution with a double peak structure. In the projectile reference frame, the fragments are emitted almost isotropically, which transforms into a forward-focused cone in the laboratory system, though with larger angular distribution as in comparison to projectile-fragmentation. Mid-mass neutron-rich nuclei very far from stability are produced through the in-flight fission method because it leads to stronger yields in this mass region as the fission fragments tend to have a similar proton-to-neutron ratio of the projectile. [87]. For instance,

the in-flight fission of heavy nuclei such as  $^{238}\text{U}$ , with significantly more neutrons than protons in comparison to medium-heavy nuclei ( $\text{N}/\text{Z}_{^{238}\text{U}} = 1.586$ ), can produce a larger number of very neutron-rich products otherwise not accessible [15]. In this experiment, the in-flight fission of the  $^{238}\text{U}$  primary beam against 3-mm thick ( $=0.56 \text{ g/cm}^2$ )  $^9\text{Be}$  target at a kinetic energy of  $345 \text{ MeV}/c^2$  was chosen. The mass distribution of this reaction peaks at the mass ranges  $A_1 \sim [72-118]$  and  $A_2 \sim [120-166]$ , and proton number ranges  $Z_1 \sim [28-44]$  and  $Z_2 \sim [50-62]$  [60].

## 5.2 BigRIPS: Selection and identification of fission fragments

The in-flight fragment separator BigRIPS [88] was used to select and identify the ejectiles of the production reaction. This spectrometer benefits from its large angular acceptances of 80 and 100 mrad in the horizontal and vertical directions, respectively, and a momentum acceptance of 6%. These large values can be achieved due to the use of the large-aperture superconducting quadrupoles that allow the collection of about half of the fission fragments [89].

BigRIPS is composed of 14 superconducting triple quadrupoles (SQT) and 6 room-temperature dipoles (D1-D6) with a  $30^\circ$  bending angle, see Figure 5.1. There are seven foci along the beamline of the separator indicated as F1-F7. The two-stage design of the spectrometer is commonly used with the first stage for the isotope separation (and selection), and the second for particle identification. The first stage comprises the area between the production target (also referred as F0) and the focal plane F2. It consists of two dipoles (D1, D2) and four STQs (STQ1-STQ4), forming a two-bend achromatic system with the momentum dispersive focus at F1 [80]. In addition, an achromatic wedge-shaped degrader is placed at the intermediate focal plane of F1 used to induce a different energy loss depending on the horizontal position of the incoming ions.

The separation of ions in a magnetic spectrometer exploits the fact that charged particles with different mass-to-charge ratios ( $A/Q$ ) and velocities ( $v$ ) have different paths in presence of a magnetic field. In a simple picture, consider a homogeneous magnetic field of constant intensity and perpendicular to the particle momentum. The kinematics of the system is given by

$$Bqv = mv^2/\rho, \quad (95)$$

with  $q$ ,  $v$ ,  $m$  the charge, velocity, and mass of the ion,  $B$  the intensity of the magnetic field, and  $\rho$  the radius of the ion trajectory in the field area. From this equation, an expression can be obtained for the *magnetic rigidity* ( $=B\rho$  [T·m]), a quantity that describes conveniently the bendability of a moving charge due to the presence of a magnetic field:

$$B\rho = \frac{p}{q} = \frac{\gamma(v) \cdot m_0 \cdot A \cdot v}{q}, \quad (96)$$

with  $m_0$  the atomic mass unit ( $\approx 931.49 \text{ MeV}/c^2$ ),  $\gamma(v) = 1/\sqrt{1-(v/c)^2}$ , and  $c$  the speed of light.

The fragment selection in BigRIPS is performed tuning the magnetic fields of the D1 and D2 dipoles. The degrader placed between D1 and D2 increases the differences of  $B\rho$  at different positions and amplifies the separation effect in the D2 area. This procedure steps on the investigations conducted at GSI in the late eighties, that led to the development of the momentum-loss achromatic method [90]. A schematic overview of the BigRIPS optics can be seen in Figure 5.3.

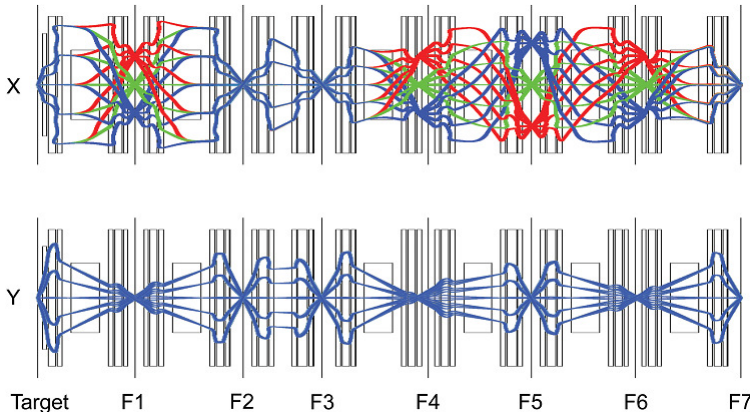


**Figure 5.3:** Schematic overview of BigRIPS ion optics. Source [88].

The second stage consists of 4 dipoles (D3-D6) and eight STQs (STQ7-STQ14) located between the foci F3 and F7, forming a four-bend achromatic system with dispersive foci at F4, F5, and F6, and achromatic foci at F3 and F7 [80]. This stage is used for the particle identification via the TOF- $B\rho$ - $\Delta E$  measurement, that allows to determine the mass-to-charge ratio ( $A/Q$ ) and atomic number ( $Z$ ) of an ion. The TOF (time-of-flight) is measured between two thin plastic scintillators counters placed at F3 and F7. A two-fold  $B\rho$  measurement is done by trajectory reconstruction from the positions and angles measured at F3 and F5 by using the PPAC detectors (Parallel Plate Avalanche Chambers) [91], and from the PPACs at F5 and F7. These measurements allow to obtain the velocity of the particle and therefore to determine the  $A/Q$  as

$$\frac{A}{Q} = \frac{B\rho}{\gamma(v) \cdot v \cdot m_0}. \quad (97)$$

The  $\Delta E$  measurement was conducted at F7 with a tilted-electrode gas ionisation chamber (TEGIC) [92]. Following the Bethe-Bloch formula, the atomic number  $Z$  is related with the energy loss via

$$\Delta E = \frac{Z^2}{\beta^2} \cdot \frac{4\pi e^4}{m_e c^2} \cdot N_g z_g \left[ \ln(2m_e v^2/I) - \ln(1 - \beta^2) - \beta^2 \right], \quad (98)$$

with [15]:

- $Z$  and  $\beta (=v/c)$  the proton number and velocity of the ion passing through the chamber gas,
- $e = \sqrt{1.4399} \text{ MeV}^{1/2} \text{ fm}^{1/2}$  (the electron charge),
- $m_e = 0.511 \text{ MeV}/c^2$  (the electron rest mass),
- $z_g = 18$  (proton number of the Argon ionisation gas),
- $I \approx 16 \cdot z_g^{0.9} \text{ eV}$  (mean ionisation potential of the gas),

$N_g$  refers to the density of atoms in the ionisation gas, which is given by

$$N_g = N_a \rho / A_g, \quad (99)$$

with

- $N_a = 6.022 \times 10^{23} \text{ mol}^{-1}$  (Avogadro's Number),
- $\rho = 1.562 \times 10^{-3} \text{ g/cm}^3$  (gas density),
- $A_g = 39.948 \text{ g/mol}^{-1}$  (atomic mass of the gas).

### 5.3 ZeroDegree spectrometer

The ZeroDegree spectrometer covers the area between the focal planes F8 and F11, see Figure 5.1. It consists of two dipoles and six STQs, indicated as D7-D8 and STQ17-22 in Figure 5.1, using similar magnets like those in BigRIPS. ZeroDegree is designed as a two-bend achromatic system with the object point located at F8, where the MINOS target was placed. The intermediate foci F9 and F10 are momentum dispersive, and the final focus at F11 is fully achromatic [80]. The section from F7 to F8 is used as a matching section between the BigRIPS separator and the ZeroDegree spectrometer, using the STQ15-16 quadrupoles. The angular-acceptance of ZD can be up to  $\pm 45$  mr and  $\pm 30$  mr in the horizontal and vertical directions, with  $\pm 3\%$  momentum dispersion [80]. The total length of the spectrometer is 36.5 m. An overview of the optics is shown in Figure 5.4. The particle identification in ZeroDegree was also conducted via the TOF- $B\rho$ - $\Delta E$  measurement, with a set of tracking detectors placed both at the focal planes F8 and F11 (e.g. one plastic scintillator and two sets of double PPACS, see Section 5.4). In addition, a TEGIC chamber was used at F11 for the energy-loss measurement.

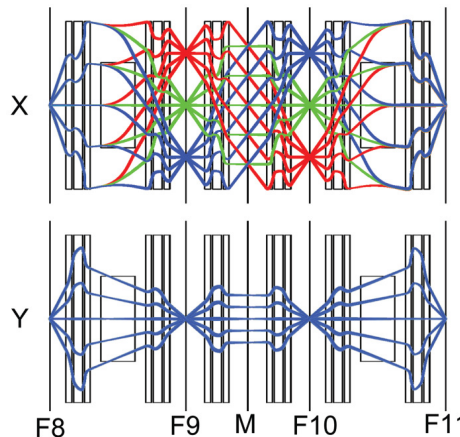


**Figure 5.4:** Schematic overview of ZeroDegree ion optics used in this experiment. Source [80].

## 5.4 Beam-line detectors for tracking and particle identification

### Parallel Plate Avalanche Counters PPACs

The Large-area Parallel Plate Avalanche Counter detector is used extensively as a focal detector in BigRIPS and the subsequent RI-beam delivery lines at RIBF. This detector measures the position of the ions passing through a sensitive area of 240 mm  $\times$  150 mm employing the delay-line readout method [91]. The reconstruction of a nucleus trajectory is done using two sets of PPACs at several focal planes (see Figure 5.1), measuring both position and angles of the fragments relative to the perpendicular axis of the plates. The performance of the detector has been tested at various beams, energies, and intensities both at RIKEN and GSI, reaching a detection efficiency  $\geq 90\%$ , and position and timing resolutions of 0.9 mm, and 1.2 ns [15]. A schematic view of this detector can be seen in Figure 5.5.

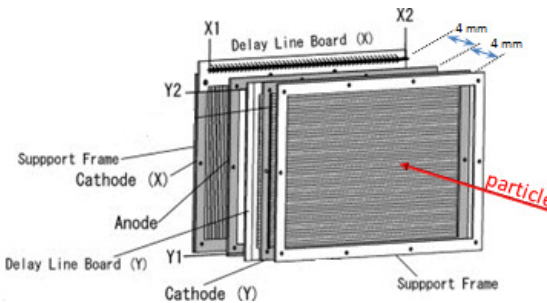


**Figure 5.5:** Schematic diagram of PPACs used at RIKEN. Modified from [91].

The operation principle of a PPAC detector consists of two parallel electrode plates separated few millimeters, across which a constant electric field in the order of hundreds of mV is produced [60]. The gap is filled with a gas that ionises easily when a charged particle traverses the detector. The released electrons are accelerated by the electric field causing themselves further ionisation of the gas and therefore an electron avalanche. The  $C_3F_8$  gas is commonly used due to its high-electron-mobility properties, leading to signals produced on the electrodes with very good timing properties (e.g. rise and fall times  $\sim 10$  ns) and almost no delay before the avalanche occurs [91]. The position measurement is achieved by using continuous thin strips adjacent to each other instead of a full plate to cover the cathode area. The two ends of each strip are connected to delay lines so that the position of the ion along the strip is found determining the time difference between the signals appearing at each side [91]. A 2D position can be obtained using two parallel cathodes planes with a  $90^\circ$  relative orientation of their strips.

The PPACS used at RIKEN are comprised of two cathodes with an anode plate in between them, see Figure 5.5. The anode was  $2.5\ \mu m$  thick, and the cathodes  $4\ \mu m$ . The distance between the electrodes is  $\sim 4$  mm. Each cathode consists of forty strips of 2.4-mm width with a  $150\text{-}\mu m$  inter-strip gap. The gas pressure to fill the PPAC was set to 30 Torr, and an operating anode bias voltage  $\leq 2000$  V was used [91]. The position of the particle (in mm) is determined as

$$X = k_x \frac{T_{x1} - T_{x2}}{2} + X_{\text{Offset}}, \quad Y = k_y \frac{T_{y1} - T_{y2}}{2} + Y_{\text{Offset}}, \quad (100)$$

with  $T_{x1}$ ,  $T_{x2}$ ,  $T_{y1}$ , and  $T_{y2}$  the time employed by the signal in the strips to travel from the interaction point to the delay line at each end of the cathode strips;  $k_x$ ,  $k_y$  the conversion factors from time to position, in this case  $1.25\ \text{mm/ns}$ ; and  $X_{\text{Offset}}$  and  $Y_{\text{Offset}}$  two offset parameters to correct any possible misalignment. For the double set of PPACs at each focal plane the analogue signals  $X_1$ ,  $X_2$ ,  $Y_1$ ,  $Y_2$ , were delivered to a Constant-Fraction-Discriminator (CFD) before being read by a Time-to-Digital Converter (TDC) [15].

### Plastic Scintillator detectors

Thin plastic scintillator detectors were placed at F3 and F7 in BigRIPS, and F8 and F11 in ZeroDegree, to produce time signals produced by the passage of ions. The signals were amplified and transformed with photo-multiplier tubes (PMTs) located to the left and right sides of the scintillator layer, placed perpendicular to the beamline. These signals were delivered to a QDC and then to a TDC for charge and time measurements [60]. The time measured at a given X focal point ( $T_{FX}$ ) is defined as the average of the time signals measured by the PMT on each side

of the corresponding scintillator (*TLX*, *TRX*). The time of flight in BigRIPS was measured by the time difference of the signals F3 and F7, namely :

$$TOF = T_{F7} - T_{F3} = \frac{TL7 + TR7}{2} - \frac{TL3 + TR3}{2} + TOF_{\text{Offset}}. \quad (101)$$

With this measurement, the velocity can be determined via  $v = L/TOF$ , since the flight path between the detectors is known (= 46.8 m).

### TEGIC: Gas ionisation Chamber

The energy loss of the ions ( $\Delta E$ ) was measured at F7. This measurement in combination with the ion velocity allows determining the proton number  $Z$ , following Equation (98). Usually, a multi-sampling ionisation chamber (MUSIC) design is used, however, due to the high-intensity beams at the RIBF the tilted-electrode gas ionisation chamber (TEGIC) design was employed [93]. The tilted electrodes reduce the recombination of electron-ion pairs within the gas, increasing the detection efficiency in comparison to the MUSIC. A schematic view of the detector is shown in Figure 5.6.

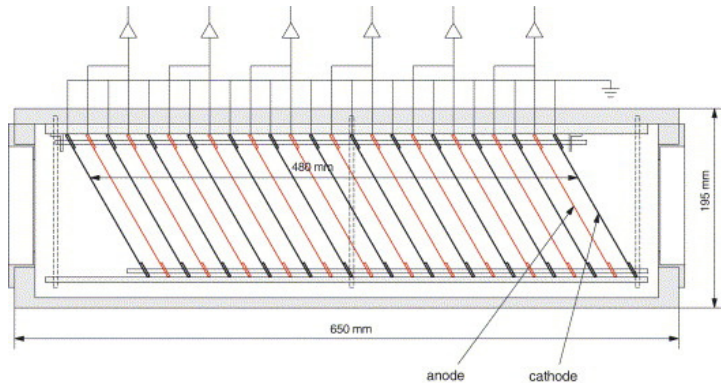


**Figure 5.6:** Schematic diagram of TEGIC detector used at RIKEN. Source [92].

The detector consisted of twelve anode plates and thirteen cathode plates placed alternatively in 20-mm steps along the 48-cm long chamber [94]. The electrode plates were tilted by 30°. A gas mixture of Ar-CH<sub>4</sub> (90/10 %) was used, with a purity larger than 99.9 %. The anodes were set to 500 V and successive pairs of anodes were connected together leading to only six outputs to read out. The cathodes were all connected and grounded together, as it is shown in Figure 5.6.

## 5.5 DALI2 & MINOS: In-beam $\gamma$ -spectroscopy of knockout reactions

A setup consisting of the MINOS device surrounded by the NaI(Tl) scintillator array DALI2 was placed at the focal plane F8, see Figure 5.7.

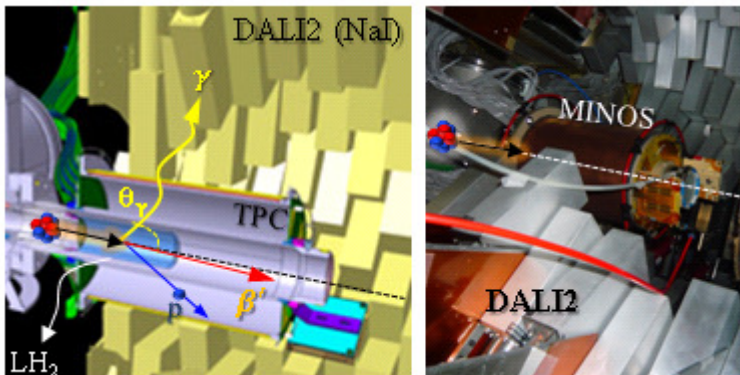


**Figure 5.7:** Schematic overview of the SEASTAR in-beam  $\gamma$ -spectroscopy setup.

The radioactive beam delivered by BigRIPS collides with the liquid-hydrogen target ( $\text{LH}_2$ ) of the MINOS device [95] causing excitation of the nuclei interacting with the protons of the target via nucleon knockout or inelastic scattering processes. The energy of the prompt  $\gamma$ -rays emitted is measured with the DALI2 scintillator array [82]. The nuclei emit in-flight at kinetic energies of  $\sim 250$  MeV/nuc. so that a Doppler-correction for the  $\gamma$ -ray energy detected is needed. For this purpose, the reaction vertex is reconstructed tracking the protons scattered in the reaction using a time projection chamber (TPC) surrounding the  $\text{LH}_2$  target. Also, the nucleus velocity during the collision is interpolated from the velocities before and after the target and the reaction position. The use of a hydrogen target with vertex reconstruction (of mm accuracy) has several advantages over a traditional solid target such as  $^{12}\text{C}$  or  $^9\text{Be}$  to perform knockout reactions of heavy-ions at the intermediate energies of this experiment. From the physics point of view, a proton is the “cleanest” hadronic probe for the knockout mechanism, populating collective and single-particle excited states close to the Fermi surface. From the experimental side, it improves the quality of the Doppler correction compared to a thick solid target where nor the velocity or emission point can be obtained with the same accuracy. The vertex reconstruction with the TPC allows the  $\text{LH}_2$  target to have larger thicknesses compared to standard solid targets leading to an increase of the luminosity, necessary for experiments with exotic nuclei where production cross-sections are very low.

The target cell containing the  $\text{LH}_2$  is made out of a polyethylene referred as Mylar. It has a 110- $\mu\text{m}$  thick entrance window with an effective target diameter of 39 mm and a 150  $\mu\text{m}$  thick exit window with 52 mm diameter [95]. The target length along the beam axis was set to 100 mm to maximize the rate of  $(p, 2p)$  reactions while minimizing the rate of a second interaction. The cell pressure was set to 0.5 bar, leading to a  $\text{LH}_2$  density of  $\sim 73 \text{ kg/m}^3$  [93].

The projectiles suffer little deviation in the target due to the inverse kinematics nature of the reactions, so most of the products can be identified with the ZeroDegree mass spectrometer, placed in the beam direction just after MINOS. The identification of the reaction products with ZeroDegree allows the unique assignment of  $\gamma$ -rays to a particular nucleus. This in-beam  $\gamma$ -spectroscopy analysis is not the scope of this thesis, however, an extensive discussion about it can be found in Ref. [96], and recent results have been published in [97], [23–26].

## 5.6 EURICA & AIDA: $\gamma$ -ray decay spectroscopy

The study of isomeric states and  $\beta$ -decays provides essential information on the nuclear structure. The half-lives of these metastable states cover a broad range from nanoseconds to years, occurring mostly in the range of nano to milliseconds. As they do not occur promptly after a nucleus production, they cannot be studied adequately via in-beam  $\gamma$ -spectroscopy. Instead, in a decay spectroscopy setup the nucleus is typically implanted into a stopper material which is in turn surrounded by high-resolution  $\gamma$ -ray detectors, with the purpose to observe the  $\gamma$ -rays emitted following the isomeric decay. Sometimes, the stopper material consists of detectors sensitive to electrons, allowing the measurement of  $\beta$ -particles or internal conversion electrons, obtaining additional valuable spectroscopic information.

During the SEASTAR experiments, a decay-spectroscopy station was set at F11, at the end of ZeroDegree, to study isomeric decays of exotic nuclei produced either at the  $^9\text{Be}$  or  $\text{LH}_2$  targets placed at F0 and F8, see Figures 5.1 and 5.8. The nuclei were stopped into the AIDA detector [83], a stack of double-sided silicon strip detector layers (DSSSD) each with an implantation area of  $8 \times 8 \text{ cm}^2$  and 1000- $\mu\text{m}$  thickness. The isomeric  $\gamma$  decays were detected with the high energy-resolution EURICA detector array. It consists of 84 HPGe crystals arranged in twelve clusters distributed in three different rings at 51° (five clusters), 90° (two clusters), and 129° (five clusters) relative to the beam axis. Each cluster, comprised of seven crystals sharing a common cryostat, was placed pointing at the center of the array, with a distance of  $\sim 21 \text{ cm}$  to the cluster frontal face. AIDA was centered in the same point as well. A picture of AIDA surrounded by several of the EURICA clusters is shown Figure 5.9.

During the experiment of this thesis, EURICA presented a similar performance compared to its commissioning test: A resolution of  $\sim 2.9 \text{ keV}$  at 1333 keV, and an

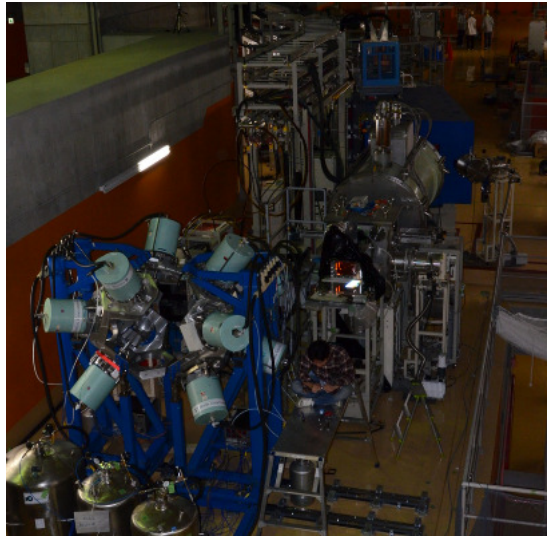


**Figure 5.8:** Decay spectroscopy station at F11 after the Zero Degree spectrometer.

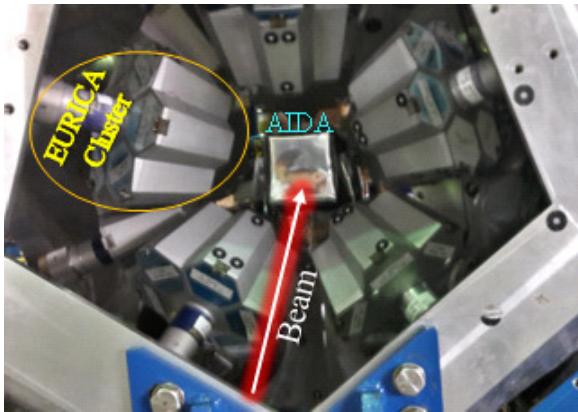


**Figure 5.9:** Decay spectroscopy setup at RIKEN using the AIDA stopper and the EURICA detector array.

absolute efficiency varying from  $\sim 19\%$  to  $\sim 6\%$  between 200 and 1400 keV [84]. The exact values will be discussed in the next chapter.

The  $\gamma$ -rays detected in the Ge crystals were correlated to the implanted nuclei on an event-by-event basis by means of the delayed- $\gamma$  coincidence technique: The energies ( $E_\gamma$ ) and times ( $t_\gamma$ ) of the hits in EURICA were recorded during a  $100\text{-}\mu\text{s}$  time window that was triggered when an ion crosses a plastic scintillator located  $\sim 1$  m upstream of implantation. The time measured corresponds to the difference

between the detection of the  $\gamma$ -ray and the trigger signal, and was used to estimate the half-lives of the isomeric states. For each crystal, two output signals were produced by the preamplifier and sent to different branches for energy and timing measurements, respectively. The energy branch was processed by a digital  $\gamma$ -finder module (DGF) manufactured by XIA [98]. A 6- $\mu$ s shaping time and a 100- $\mu$ s time gate were used for the DGF to measure the  $\gamma$ -ray hits in EURICA. The DGF acts as an ADC with 65536 channels, as well as a Time-to-Digital Converter (TDC) with a resolution of 25 ns/bin. The HV and gain of the crystals' preamplifiers were set to measure energies up to  $\sim$ 7 MeV, with  $\sim$ 0.10 keV/bin.

In the analogue timing branch, the preamplifier signal was sent to a timing filter amplifier (TFA), followed by a constant fraction discriminator (CFD), from which two identical output signals were extracted and analysed in parallel. One of them was processed by a (short-range) V775 CAEN TDC [99] with 1.2  $\mu$ s time range and 0.31 ns digital time resolution. The other one was processed by a (long-range) V767 CAEN TDC [99] with 800  $\mu$ s time range and 0.73 ns digital time resolution. Having three time branches (DGF, short-range, long-range) allows scanning different time regimes with different resolutions.

An add-back algorithm was implemented for the energy reconstruction of  $\gamma$ -rays that were Compton-scattered between adjacent crystals, with the purpose of increasing the efficiency at high  $\gamma$  energies. It will be explained in more details in Section 6.2.3.

In this experiment, AIDA was used in a stand-alone mode to perform commissioning measurements. Therefore, no data merging with EURICA or BigRIPS was retrieved so no information for electrons emitted from  $\beta$ -decay or nuclear de-excitation via internal conversion were analysed. The data analysis of this thesis was focused on the  $\gamma$ -ray decay branch of the isomer decay.

---

## 6 Data Analysis

---

In this chapter, the data analysis procedure is discussed. The spectroscopic information of a nucleus was determined via particle- $\gamma$  correlation, analyzing the set of  $\gamma$ -rays detected by EURICA within a 100  $\mu$ s time window after a particle crosses the plastic scintillator at F11, just about  $\sim$ 1 m before its implantation into AIDA. The data analysis is divided into a particle identification (PID) process (Section 6.1) to select the nuclei of interest; and a  $\gamma$ -ray analysis section (Section 6.2). If not explicitly mentioned, the histograms shown for the particle identification part correspond to the dataset of the run 3023.

---

### 6.1 Zero Degree Particle identification

---

#### 6.1.1 Atomic number determination

---

The atomic number was obtained from the  $\Delta E$  energy loss at F11 and the nucleus velocity  $v$  between F8 and F11. The uncalibrated energy loss  $\Delta E_{raw}$  is determined as the geometric mean of the signals provided by the six anode read-outs of the TEGIC at F11,

$$\Delta E_{raw} = \left\{ \prod_{i=1}^6 \Delta e_i \right\}^{1/6}. \quad (102)$$

In those cases where an ion is stopped before the end of the chamber then at least one of the  $\Delta e_i$  signals will be zero, and therefore  $\Delta E_{raw}=0$ . Those background cases are automatically excluded thanks to the employment of the geometric mean to define  $\Delta E$ .

Using Equations 98 and 102 the atomic number was determined as:

$$\begin{aligned} Z &= p_0 \times \left[ \beta \cdot \sqrt{\frac{\Delta E_{raw}}{\ln(2m_e v^2/I) - \ln(1 - \beta^2) - \beta^2}} \right] + p_1, \\ Z &= p_0 \times Z_{raw} + p_1 \end{aligned} \quad (103)$$

with  $\{p_0, p_1\}$  the parameters to be determined in a linear calibration. This procedure was conducted independently for each one of the 47 run datasets since the *gain factor* of the TEGIC was not constant during the experiment time. The variation is caused by a temperature-dependence of the IC chamber gain and reflected in a change of few percent in its output signal due to room-temperature changes. The  $Z_{raw}$  histogram is shown in Figure 6.1. A multi-Gaussian function was fitted to obtain the centroids and widths of the peaks, and a subsequent linear calibration into atomic number units was performed. Specific atomic number values have been assigned to the peaks based on the fact that the largest production of nuclei corresponds to Krypton ( $Z=36$ ). The assignment was corroborated afterwards looking to the EURICA  $\gamma$ -ray spectroscopic information of known isomeric transitions in

this mass region. A high linearity of the raw data signals is observed, but also a right-skewed distribution for the Br and Kr peaks, produced by piled up signals in the TEGIC and more visible for the more intense nuclei.

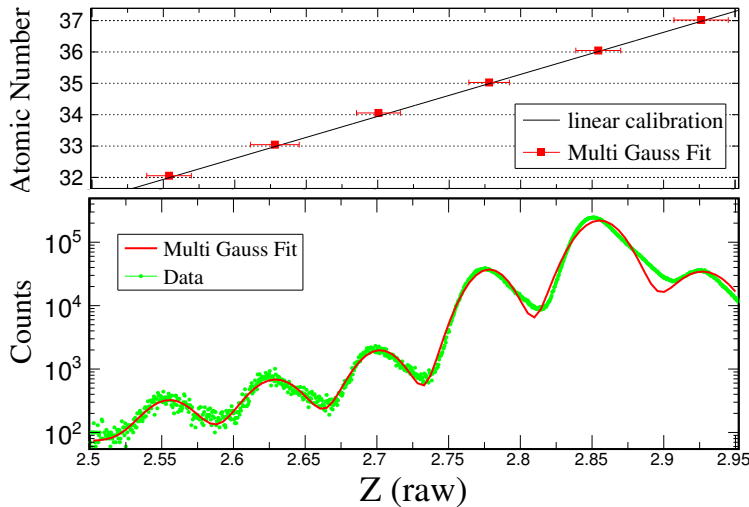


**Figure 6.1:** (Bottom)  $Z_{\text{raw}}$  histogram and the multi-Gaussian function fitted to find the peaks' positions. (Top) Linear calibration into atomic number units.

The  $Z$  value presented a slight dependence with the velocity. This dependence leads to a slight broadening of the peaks at different  $Z$  values. A linear adjustment was applied to correct this problem, leading to the  $Z$ -vs- $\beta$  histogram shown in Figure 6.2.

### 6.1.2 Mass-to-Charge ratio determination

The mass-to-charge ratio is determined using the Equation (97),

$$\frac{A}{Q_{F8-11}} = \frac{B\rho}{\gamma(v) \cdot v \cdot m_0}. \quad (104)$$

To determine  $B\rho$ , the radius  $\rho$  is obtained after the trajectory reconstruction of the positions and angles using the PPACS at F8 and F11. The  $A/Q$  histogram for events with  $33.5 \leq Z \leq 34.5$ , selecting mainly Selenium nuclei, is shown in Figure 6.3. The calibration procedure was similar to the atomic number calibration. A multi-Gaussian fit was used to obtain the centroids and a linear calibration was used afterwards to convert to  $A/Q$  values. Two peaks centred at 2.641 and 2.665 were added to fit the contaminant peaks of Br nuclei and not degrade the centroid determination of the Selenium peaks.

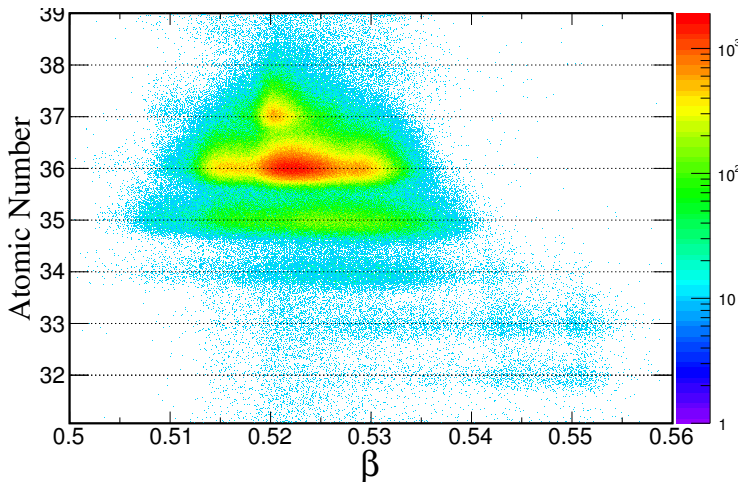


**Figure 6.2:**  $Z$ -vs- $\beta$  histogram with the corrections to achieve  $\beta$  independence of the atomic number reconstructed. The color scale at the right corresponds to the number of events per bin.

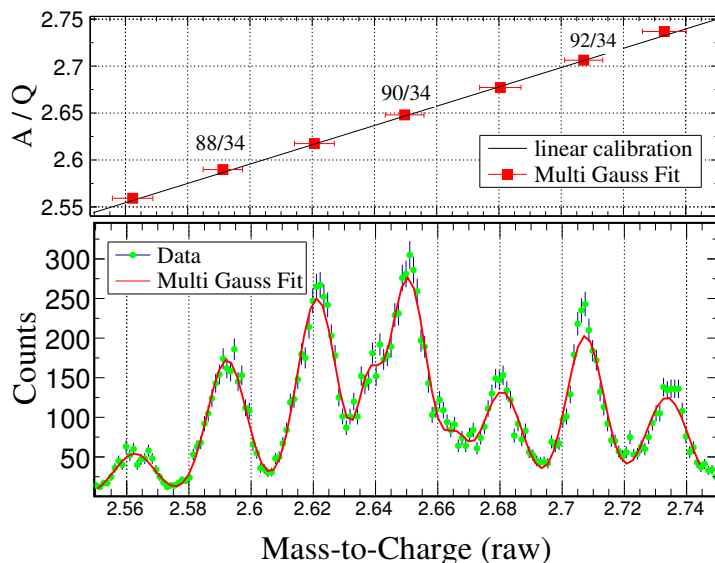


**Figure 6.3:** (Bottom) Raw mass-to-charge histogram and the corresponding multi-Gaussian fit. (Top) Linear calibration to  $A/Q$  values.

### 6.1.3 Improvement of the Particle IDentification (PID)

The resolution of  $A/Q$  depends on the tracking detectors signals used for the angle and position reconstruction at F8 and F11, as it is shown in Figures 6.4 and 6.5 for events with  $33.5 \leq Z \leq 34.5$ . The strip-like structures clustering large number of counts correspond different isotopes. These structures should be vertical so that a projection on the  $A/Q$  axis would not mix events from different nuclei. However, the ‘non-corrected’ distributions are tilted and deformed leading to a low mass resolution, like the one in Figure 6.3. The correction was applied to rotate and align the histograms with respect to their central values, straightening up the distributions.

$$\begin{aligned}
 A/Q_{corr.} = A/Q &+ p_1(F8X - F8X_{av.}) + p_2(F8X - F8X_{av.})^2 \\
 &+ p_3(F8A - F8A_{av.}) + p_4(F8A - F8A_{av.})^2 \\
 &+ p_5(F11X - F11X_{av.}) + p_6(F11X - F11X_{av.})^2 \\
 &+ \underbrace{p_7(F11A - F11A_{av.})}_{\text{rotation}} + \underbrace{p_8(F11A - F11A_{av.})^2}_{\text{straightening}}
 \end{aligned} \quad (105)$$

The set  $\{p_i\}$  of parameters were tuned iteratively until the width of the strip distributions was considerably decreased and at the same time the adjacent ones did not overlap on the  $A/Q$  axis. The values used are shown in Table 5. A slight dependence with the angles (F8A and F11A) remains after the corrections, but it was not further optimized after the distributions did not overlap considerably.

$F8X_{av.}$	0	$p_1$	$70 \cdot 10^{-6}$	$p_2$	$15 \cdot 10^{-8}$
$F8A_{av.}$	-1335.4	$p_3$	$45 \cdot 10^{-5}$	$p_4$	$85 \cdot 10^{-4}$
$F11X_{av.}$	0	$p_5$	$62 \cdot 10^{-5}$	$p_6$	0
$F11A_{av.}$	-70	$p_7$	$40 \cdot 10^{-5}$	$p_8$	$8 \cdot 10^{-6}$

**Table 5:** Set of parameters used in the  $A/Q$  optical corrections.

The Particle IDentification histogram corresponds to an  $Z$ -vs- $A/Q$  plot, which is shown in Figure 6.6 before and after the implementation of the optical corrections. A projection on the  $A/Q$  axis for the regions corresponding to  $^{92,93,94}\text{Se}$  is shown in Figure 6.7, where the impact of the corrections on the mass resolution is evidenced, narrowing down the width of the peaks. The obtained mass resolution, defined as  $\Delta A = FWHM_A/A$ , are shown in Table 6.

$A$	92	93	94
$\Delta A$	$3.6 \cdot 10^{-3}$	$3.8 \cdot 10^{-3}$	$4.3 \cdot 10^{-3}$

**Table 6:** Mass resolution for  $^{92,93,94}\text{Se}$  isotopes.

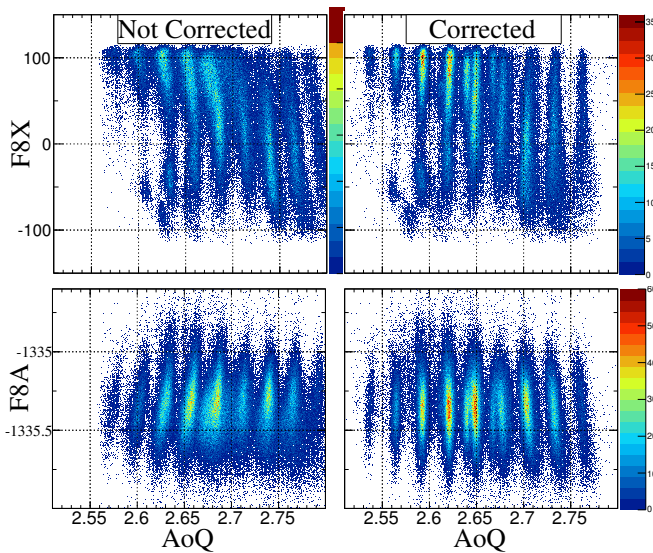


**Figure 6.4:**  $A/Q$  vs  $F8X$  (top) and  $F8A$  (bottom), before (left) and after (right) optical corrections. Histograms on the same row share the same z-axis scale, shown in the colour-palettes on the right.

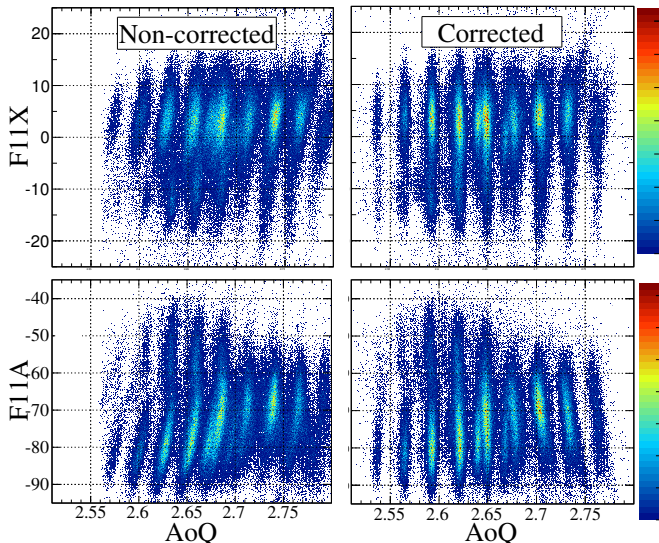


**Figure 6.5:**  $A/Q$  vs  $F11X$  (top) and  $F11A$  (bottom), before (left) and after (right) optical corrections. Histograms on the same row share the same z-axis scale, shown in the colour-palettes on the right.

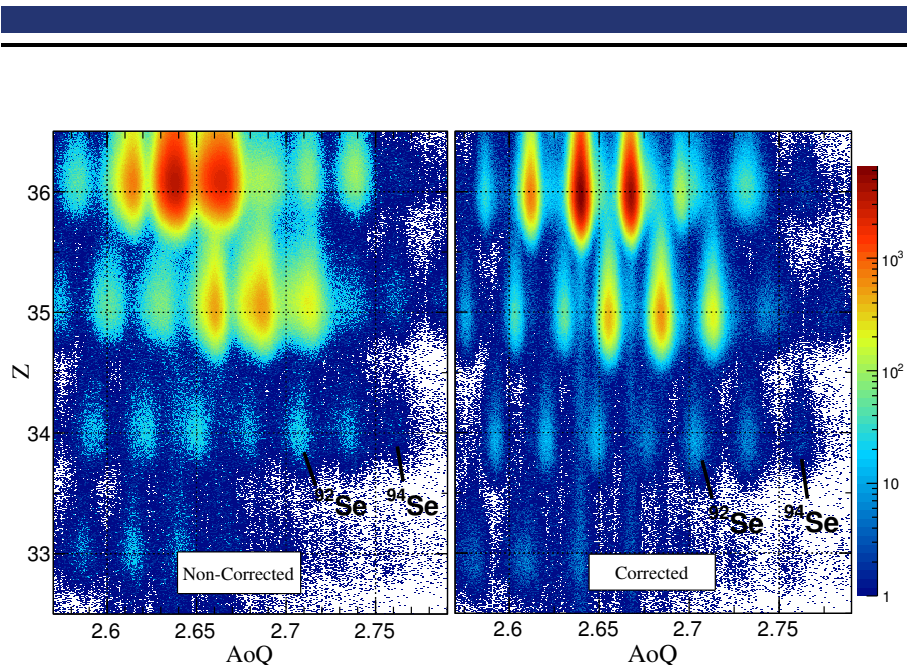


**Figure 6.6:** PID plot before (left) and after (right) optical corrections for the date.

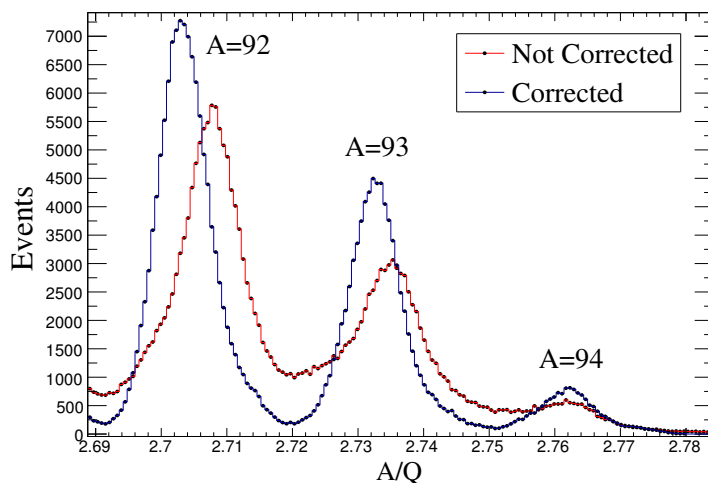


**Figure 6.7:** A/Q spectrum for events with  $33.6 \leq Z \leq 34.4$  before and optical corrections.

## 6.2 Analysis of $\gamma$ -rays with EURICA

### 6.2.1 Energy calibration

HP-Ge detectors are unique due to their high energy resolution, therefore, the energy calibration of each crystal of the array must be as accurate as possible in a broad energy range from few keV up to  $\sim 3$  MeV, where low-lying nuclear transitions are normally observed.

When a  $\gamma$ -ray interacts with a crystal, the preamplifier produces an output signal with a height proportional to the energy deposited by the  $\gamma$ -ray. The DGF module linearly assigns to each height a bin position in the range from 0 to 65535, so the bin number has a proportionality relation to the energy deposited by the photon.

During a measurement over some time, the counts registered at each bin position are stored, leading to a “raw-energy” spectrum with the x-axis representing the bin number and the y-axis the number of counts. The energy calibration consisted of rescaling the bin axis of each crystal’s spectrum through the function

$$E_\gamma \text{ (keV)} = a_0 + a_1 \cdot x_b + a_2 \cdot x_b^2 \quad (106)$$

where  $\{a_i\}$  is a set of parameters to be found and  $x_b$  the bin position.

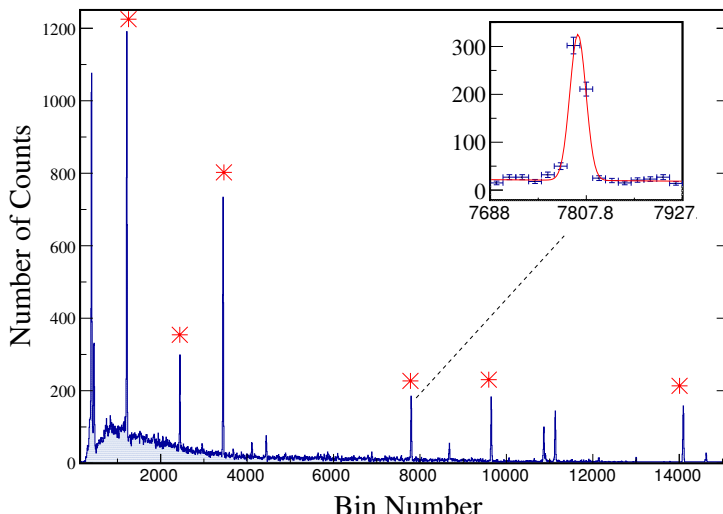


**Figure 6.8:** Raw energy spectrum of crystal N°9 of the  $^{152}\text{Eu}$  source. Peaks marked with (\*) were used for the energy calibration. The inset shows an example of the fit used to find a peak centroid.

A standard  $^{152}\text{Eu}$  calibration source placed in front of AIDA was used for the energy calibration procedure. As an example, the raw-energy spectrum obtained with the crystal N°9 is shown in Figure 6.8. The photo-peaks marked with (\*) were used for the energy calibration and correspond to the strongest  $^{152}\text{Eu}$  transitions, listed in Table 7.

For each peak, the function

$$N_c(x_b) = c_0 \cdot \exp \left\{ -\frac{(x_b - c_1)^2}{2c_2^2} \right\} + c_3 + c_4 \cdot x_b, \quad (107)$$

with  $N_c$  the number of counts at the bin position  $x_b$  and  $\{c_i\}$  parameters to optimize, was fitted to an area of the spectrum comprising only the peak and some bins close to it. In particular, the parameters  $c_1$  and  $c_2$  correspond to the photo-peak's centroid and standard deviation, respectively. The background is assumed to change linearly over the peak range, and is represented by the parameters  $c_3$  and  $c_4$ . An example of this fit is shown in the inset of Figure 6.8.

$E_\gamma$ (keV)	$I_\gamma$
121.78(1)	0.2841(13)
244.69(1)	0.0755(4)
344.27(1)	0.2658(12)
778.90(1)	0.1296(6)
964.08(1)	0.1462(6)
1408.01(1)	0.2085(9)

**Table 7:**  $^{152}\text{Eu}$  transitions used for the energy calibration. The intensity  $I_\gamma$  is equal to the probability of emitting a photon of  $E_\gamma$  per one nucleus decay [100].

The set of points  $\{(E_\gamma, c_1)_i\}$  were used to find the parameters of the energy calibration function described in Equation (106) via a  $\chi^2$  fit method. The fit results for some crystals can be seen in Figure 6.9. As an example, for crystal N°9 it was obtained  $a_0=0.23(95)$  keV,  $a_1=9.99(4) \cdot 10^{-2}$  keV/bin, and  $a_2=4.79(24) \cdot 10^{-9}$  keV/bin $^2$ . The detection system, composed by the detectors and the electronics, has high linearity over the large energy range considered, which is reflected in the fact that  $a_2/a_1 \ll 1$ .

The raw and energy-calibrated spectra for all the EURICA crystals are shown in Figure 6.11. The x-axis corresponds to the crystal number (ID), the y-axis corresponds to the energy scale (in a.u. or keV), and the z-axis (represented with the color scale shown to the right) corresponds to the number of counts registered at each bin position.

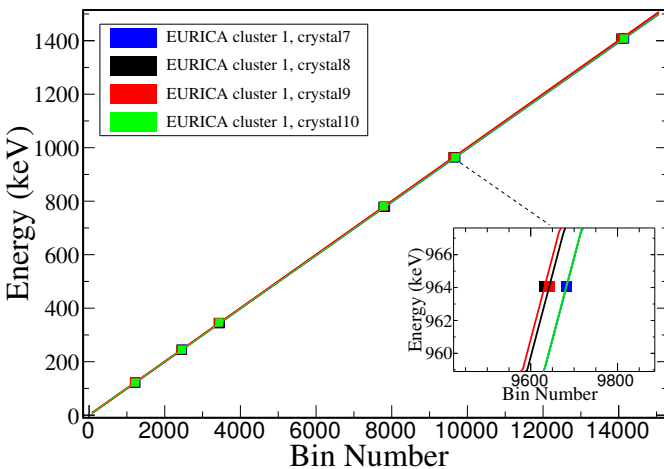


**Figure 6.9:** Bin Number vs  $E_{\gamma}$  for some EURICA crystals and the energy-calibration functions fitted. The inset shows a zoom view near the 778 keV peak.

The energy-resolution  $R = \text{FWHM}(E_{\gamma})/E_{\gamma}$ , is shown in Figure 6.10 for the same set of crystals of Figure 6.9. The obtained values are always lower than 1.6 % showing the high-resolution feature of HP-Ge detectors.

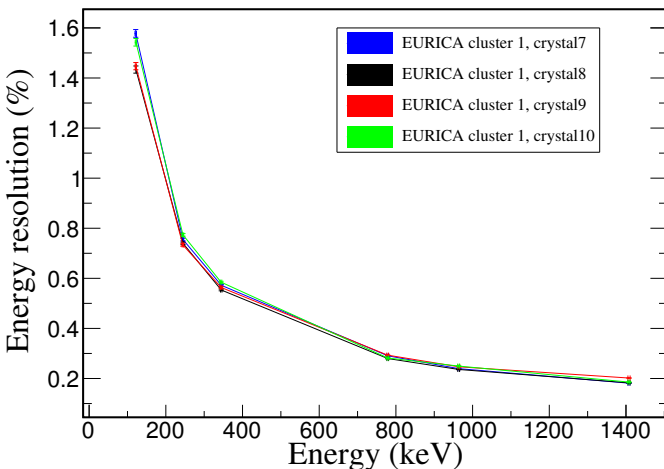


**Figure 6.10:** Energy resolution of the EURICA crystals shown in Figure 6.9. A high resolution is observed for the whole energy range between 122 and 1408 keV, always below 1.6 %.

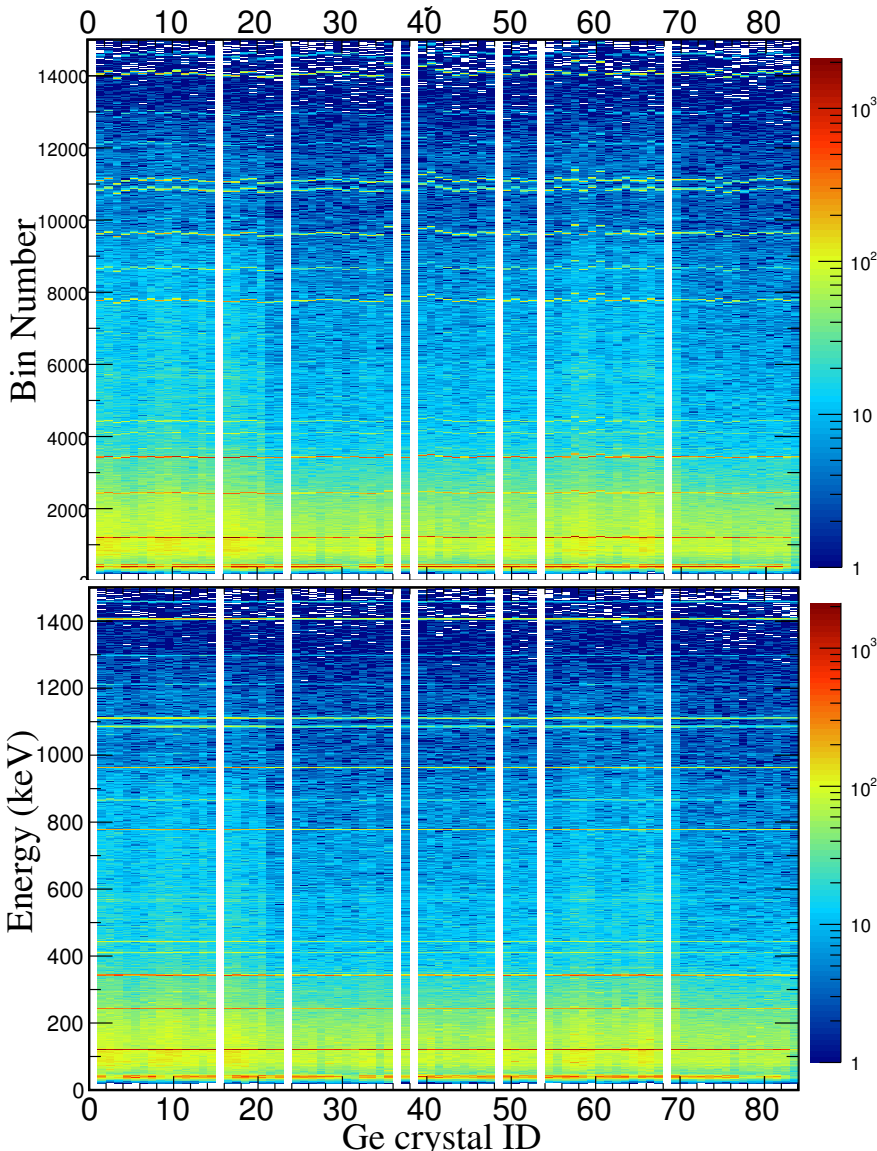


**Figure 6.11:** Energy spectra of the different crystals obtained with the  $^{152}\text{Eu}$  source. (Top) Raw spectra, the y-axis represents the bin number. (Bottom) Energy-calibrated spectra, the y-axis in keV units. The scale of the z-axis is logarithmic and is represented by the colour code shown to the right.

## 6.2.2 Time-walk correction

For this experiment the  $\gamma$ -ray detection time was taken from the DGF modules. In principle, they have incorporated a digital constant fraction algorithm to measure event arrival times down to a few nanoseconds accuracy [98]. However, a large time-walk effect was observed in the data, see Figure 6.12. The spectrum to the left corresponds to the  $E_\gamma$ -vs- $t_\gamma$  matrix obtained using the time measured by the DGF modules. The large-intensity region in the spectrum that shifts from  $t_\gamma \sim 0$  at  $E_\gamma \sim 100$  keV to  $t_\gamma \sim -200$  ns for bigger energies, corresponds to photons emitted during the ion stopping process (see Section 6.2.5), and therefore they should be registered at the same time regardless their energy. This dependence of  $t_\gamma$  with the energy  $E_\gamma$  was partially corrected with an energy-dependent time offset added to align the distribution. The time-walk corrected spectrum is shown to the right.

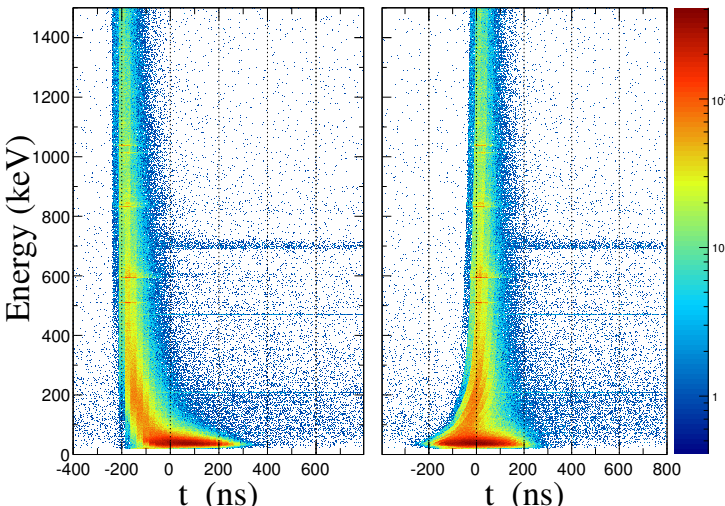


**Figure 6.12:**  $E_\gamma$ -vs- $t_\gamma$  matrix using the DGF time information before (left), and after (right) time-walk correction.

## 6.2.3 Addback

As it was discussed in Section 4.4, the probability of a photo-electric interaction in the detector decreases rapidly with  $E_\gamma$ , and the Compton scattering becomes the dominant interaction process in Ge crystals for  $E_\gamma \sim 250$ -4000 keV. In fact, in a single-crystal spectrum, some counts of any photo-peak correspond not always to a direct photoelectric absorption of the  $\gamma$ -ray, but to multiple scattering of the photon

within the same crystal, releasing full photon energy. Nevertheless, the probability of a large scattering angle increases strongly with  $E_\gamma$  following the Klein-Nishina relation so that the scattering in several crystals is more likely for photons with high energies. An addback routine was implemented to reconstruct the total energy of the photons scattered over several crystals, leading to an increase of the photo-peak efficiency of the detector. All cases where 2 or 3 adjacent crystals (of the same cluster) were fired within less than 400 ns time difference are considered Compton-scattered hits of a same photon. The addback algorithm sums up the individual energies registered by each crystal and assigns to the reconstructed photon a time  $t_\gamma$  equal to the time registered by the crystal with the largest energy deposition. If the time difference was more than 400 ns, the hits are considered individual photons. A schematic overview of the addback algorithm implemented is shown in Figure 6.13. Its impact on the efficiency of the EURICA array is discussed in the next section.

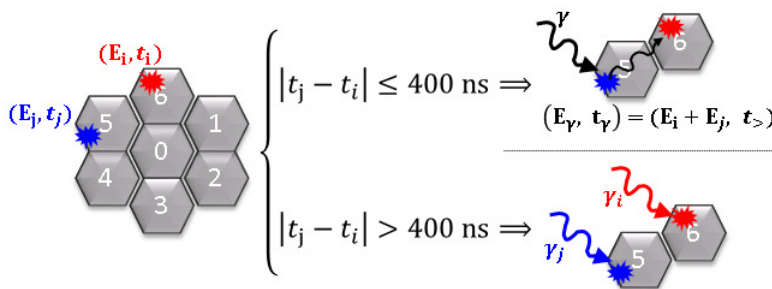


**Figure 6.13:** Schematic overview of Addback algorithm applied.

#### 6.2.4 Detection efficiency

The energy-dependent attenuation coefficient of matter to the passage of  $\gamma$ -rays leads to a variable detection efficiency for  $\gamma$ -detectors. The number of counts in a photo-peak at a given energy  $E_\gamma$  is given by

$$A_{phot.}(E_\gamma) = \epsilon_{phot.}(E_\gamma) \cdot I_t(E_\gamma), \quad (108)$$

with  $\epsilon_{phot.}(E_\gamma)$  the *photo-peak efficiency* and  $I_t(E_\gamma)$  the total number of photons of  $E_\gamma$  emitted by the source. In this experiment, a calibration of the detection efficiency was done placing the  $^{152}\text{Eu}$  source in the front layer of AIDA. The EURICA DAQ was triggered by a 1-kHz clock (pulse generator) leading to a separation of 1 ms between each trigger, bigger than the dead time of the system. The measurement time-window after each trigger signal was  $100 \mu\text{s}$ . Therefore,

$$I_t(E_\gamma) = a_s \cdot N_{trig} \cdot \Delta T \cdot b_\gamma, \quad (109)$$

with  $a_s$  the source activity,  $N_{trig}$  the number of trigger signals sent to the DAQ during the measurement,  $\Delta T$  the measurement time-window, and  $b_\gamma$  the branching ratio of the  $\gamma$ -ray emitted by the source. In particular, we are interested in the *relative efficiency*, which corresponds to  $\epsilon_{phot.}(E_\gamma)$  normalized to the efficiency at a given known energy, in this case  $E_0=245$  keV:

$$\epsilon_r(E_\gamma) = \frac{\epsilon_r(E_\gamma)}{\epsilon_r(E_0)} = \frac{N_{exp}(E_\gamma)/b_\gamma}{N_{exp}(E_0)/b_0}. \quad (110)$$

$N_{exp}(E_\gamma)$  was obtained from the photo-peak areas after background subtraction, and well-known branching ratios  $b_\gamma$  for  $^{152}\text{Eu}$  source transitions were taken from literature [100]. The values measured for  $\epsilon_r$  with and without addback are shown in Figure 6.14.

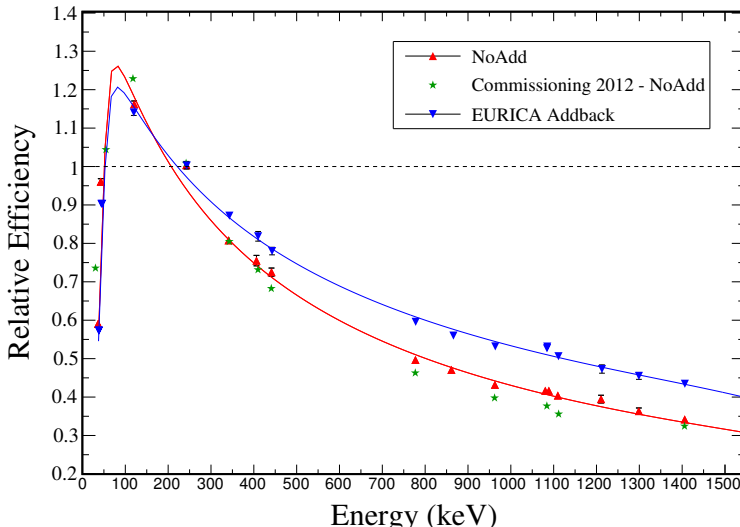


**Figure 6.14:** Relative photo-peak efficiency with (blue) and without (red) addback. The values measured during the commissioning [84] (green) are presented as well.

An efficiency calibration function was determined fitting the measured data points to the widely used expression [101]:

$$\epsilon_r(E_\gamma) = \exp\{[(p_0 + p_1 \cdot x + p_6 \cdot x^2)^{-p_5} + (p_2 + p_3 \cdot y + p_4 \cdot y^2)^{-p_5}]^{-1/p_5}\}, \quad (111)$$

with  $x = E_\gamma/100$ ,  $y = E_\gamma/1000$ , and  $E_\gamma$  in keV. The parameters  $\{p_i\}$  were extracted from the fit. The corresponding calibration functions are shown in Figure 6.14. The efficiency was found to drop by 50 % at 1 MeV relative to the efficiency at  $E_\gamma = 245$  keV. The impact of addback is evidenced for energies  $E_\gamma > 200$  keV. For

---

---

comparison purposes, the efficiency measured for the individual crystals during the commissioning of EURICA is presented, showing a similar behaviour to the one found in this work.

---

### 6.2.5 Background and selection of isomeric $\gamma$ -rays

Different sources of background affect strongly the energy spectrum of the  $\gamma$ -ray detectors used in experiments with heavy-ion beams. Understanding its origin is important to separate it as much as possible from the spectroscopic information of the exotic nuclei studied. The most intense contribution, commonly referred as “atomic background”, corresponds to the radiative processes caused by *atomic* collisions when the ions are decelerated into matter, leading to the emission of electromagnetic radiation of a continuous spectrum in the range  $\sim$ 10-1000 keV with cross sections  $\sim$ 0.1-100 barn/keV [102]. A detailed explanation of the underlying physics processes, namely, the Radiative Electron Capture (REC), and the Primary and Secondary-Electron Bremsstrahlung (PEB, SEB), can be found in Ref. [102]. Though these phenomena are several orders of magnitude more intense than the decay of exotic nuclei, its impact on the  $\gamma$ -energy spectra depends mostly on the geometry of the setup, in particular on the solid angle of the detectors with respect to the emission point. In decay spectroscopy experiments this background contribution creates the prompt flash of  $\gamma$ -rays emitted when the nuclei are implanted into the stopper device. In the present experiment, it can be seen at the beginning of the 100  $\mu$ s time window opened after implantation, as it is shown in Figures 6.12 and 6.15.

On the other hand, the passage of heavy-ions with energies of  $\sim$ 10<sup>2</sup> MeV/u through different elements along the beam-line such as degraders (mainly composed of aluminium), plastic scintillators (made of CH-chains), and the stopper layers themselves, can lead to the emission of light particles such as p,n, or light nuclei. Though experimental studies dedicated to measuring this phenomenon accurately are still missing, it is frequently assumed that the emission of neutrons can be more critical because their large range in comparison to charged particles give them bigger probabilities to reach  $\gamma$ -ray detectors inducing inelastic scattering reactions in all the matter nearby. Indeed, in the present experiments peaks of 691 keV from  $^{72}\text{Ge}(n, n')$ , 608 and 595 keV from  $^{74}\text{Ge}(n, n')$ , 563 keV from  $^{76}\text{Ge}(n, n')$ , and 197 keV from  $^{19}\text{F}(n, n'\gamma)$ , were observed in addition to the 79 and 85 keV X-rays from Lead.

Other background sources are the natural occurring radioactive materials (NORM) such as U, K, or Th are present in most of the substances on Earth. They emit different  $\gamma$ -rays also observed in the experiment such as 1460, 1121, 352, 338 keV. A visible 511 keV peak corresponds to the different positron-electron annihilation events that are always present in these type of experiments.

Additionally, it is worth to remark that the accumulation of the exotic nuclei implanted becomes itself a source of background radiation: The rate of nuclei implantation into AIDA was around  $\sim 500$  Hz, much higher than the beta-decay rates of the nuclei in the mass region  $A \sim 90$ ,  $Z \sim 34$  which are in the order of few Herz (the half-lives in this region are around  $\sim 100$  ms). In this situation, an effective constant source is generated, according to the Bateman Equations. The beta-decay also implies the emission of many  $\gamma$ -rays and neutrons (when energetically possible) increasing the background level.

It is not possible to identify all background peaks only by comparison to databases, so the combination of at least two of the following criteria were used to distinguish possible background peaks from the isomeric  $\gamma$  decays of a nucleus:

- The peak appears in the  $\gamma$ -ray energy spectrum of several nuclei.
- The peak intensity does not decrease gradually over time following an exponential decay. Instead, the intensity remains constant or changes with no clear pattern over time.
- The peak has no particular time correlation with the transitions of a specific nucleus, meaning that it was not emitted after the decay of one or several isomer states in a nucleus decay path.

Several of these aspects can be seen in Figure 6.15. The plot on top shows the energy spectra in coincidence with the nuclei of the Selenium isotopic chain ( $Z=34$ ) for  $t_\gamma \leq 250$  ns (blue), and  $250 \text{ ns} < t_\gamma < 95 \mu\text{s}$  (red). The statistics accumulated during the first 250 ns after ion implantation is larger than the left  $94.750 \mu\text{s}$ , a direct consequence of the large atomic background. Some intense peaks of NORM radioactivity or neutron reactions are also indicated. The plot at the bottom shows a partial energy spectrum for  $250 \text{ ns} < t_\gamma < 30 \mu\text{s}$  (red),  $30 \leq t_\gamma < 60 \mu\text{s}$  (green), and  $60 \leq t_\gamma < 90 \mu\text{s}$  (blue). The peaks at 511 and 563 keV are observed for all the Se isotopes produced, with their intensities remaining constant for the different time ranges, fulfilling the criteria above mentioned for background peaks. In contrast, the peaks at 429, 503, and 539 keV appear only for  $^{92}\text{Se}$ , with their intensity decreasing gradually for larger times, characteristic of an isomeric decay. This analysis will be discussed in detail in the next chapter.

### 6.2.6 $\gamma\gamma$ coincidences

For many implanted nuclei, two or more  $\gamma$ -rays were detected with EURICA during the  $100 \mu\text{s}$  detection window. The set of detected  $\gamma$ -ray energies  $\{E_{\gamma i}; i = 1, \dots, m_\gamma\}$  with  $m_\gamma$  the multiplicity of the event, can be used to create a  $\gamma\gamma$  coincidence matrix, e.g. a bi-dimensional histogram filled with the pairs  $(E_x, E_y)$ , with  $x = 1, \dots, m_\gamma$ ;  $y =$

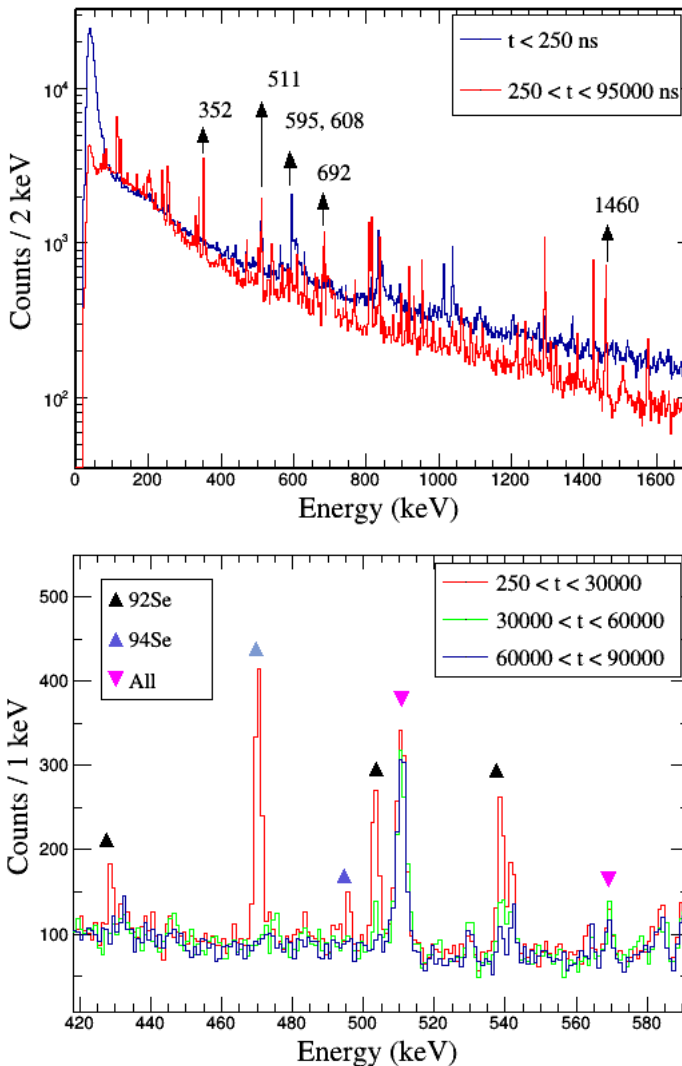


**Figure 6.15:** Energy spectra of  $\gamma$ -rays correlated to implantations of  $Z=34$  nuclei with different time conditions. (Top) Spectra for  $t_\gamma < 250$  ns (blue), and  $t > 250$  ns (red). (Bottom) partial spectra in three different time ranges showing the different behaviour of isomeric transitions and background peaks.

$x + 1, \dots, m_\gamma$ , revealing which coincident pair of energies happened more frequently during the experiment.

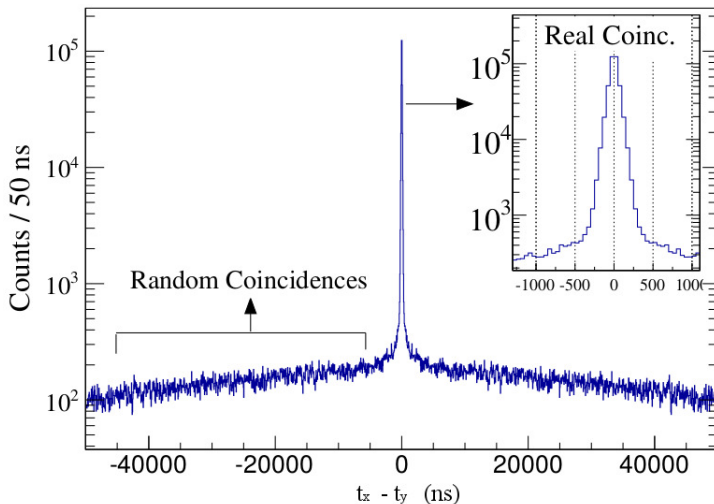


**Figure 6.16:** Time difference histogram for coincident pairs of delayed  $\gamma$ -ray energies detected in EURICA. The conditions  $250 \text{ ns} \leq t_y \leq 95 \mu\text{s}$ , and  $20 \text{ keV} \leq E_\gamma \leq 5 \text{ MeV}$ .

When a coincident pair  $(E_x, E_y)$  is emitted by the same source then the  $\gamma$ -rays must have a defined time correlation. For instance, the transitions following the isomeric decay of nuclei are detected almost at the same instant because nuclear states lifetimes are lower than few pico or nanoseconds (except isomeric states), therefore their detection time difference should satisfy  $t_x - t_y \approx 0$ . In case that a second isomeric state is populated along the decay path, the time difference should follow an exponential distribution  $\exp\{-t/\tau\}$ , with  $\tau$  the life-time of the second isomer. The time difference histogram for “delayed”  $\gamma$ -rays (e.g. not belonging to the prompt flash mentioned in Section 6.2.2) with energies between  $20 \text{ keV} \leq E_\gamma \leq 5 \text{ MeV}$  and gated on Se nuclei is shown in Figure 6.16. The region of “real” coincidences was chosen as  $|t_x - t_y| \leq 500 \text{ ns}$  where the distribution of events forms a peak-like structure with a maximum of  $\sim 1.1 \cdot 10^5$  counts and  $\sim 500\text{-ns}$  width. The region of “random” coincidences corresponds to  $|t_x - t_y| > 500 \text{ ns}$ , with a slightly decreasing behaviour around a mean value of  $\sim 180$  counts. The ratio of total number of counts in both regions  $N_{\text{random}}/N_{\text{real}} = 2.9 \cdot 10^5 / 4.3 \cdot 10^5 \approx 0.6$  show that random-coincidences are about 60% of the real ones, so they must be excluded from further analysis steps.

The  $\gamma\gamma$  coincidence matrix of delayed  $\gamma$ -rays of Se nuclei, with the ‘real coincidence’ condition  $|t_x - t_y| \leq 500 \text{ ns}$ , is shown in Figure 6.17. For each pair of coincident  $\gamma$ -rays one count was added to the points  $(E_x, E_y)$  and  $(E_y, E_x)$ , just to obtain a symmetric matrix. A projection of the matrix for  $501 \leq E_y \leq 506 \text{ keV}$  is

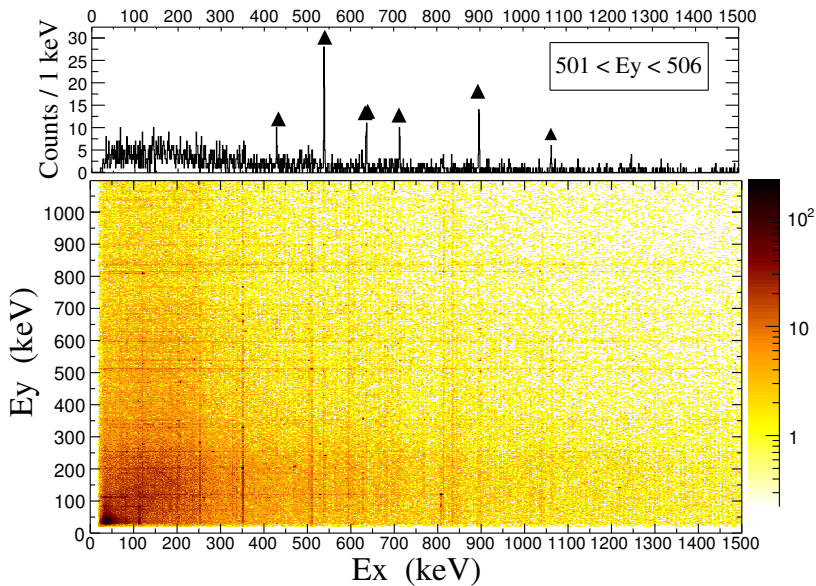


**Figure 6.17:**  $\gamma\gamma$  coincidence matrix with delayed  $\gamma$ -rays correlated with Se nuclei. Shown on top, revealing other transitions in coincidence with the 503 keV transition of  $^{92}\text{Se}$  already shown in Figure 6.15.

---

## 7 Results

---

The  $\gamma$ -ray spectroscopic information found for  $^{92,94}\text{Se}$  are presented in this chapter. The events of each nucleus were selected using a logical condition on the PID plot. The delayed  $\gamma$ -rays of these events were separated from the prompt ones and used to create the  $E_\gamma$ -vs- $t_\gamma$  matrix, where the isomeric  $\gamma$  rays (defined here as the  $\gamma$ -rays emitted by the nucleus after its decay from an isomeric state) were identified analyzing the change of the photo-peak intensity over time.

The isomeric  $\gamma$ -decays found were further studied via  $\gamma\gamma$ -coincidences, to understand their correlations and the level scheme. An effective half-life was obtained for each transition fitting a decay-curve to the time spectrum of the  $\gamma$ -rays in the transition photo-peak. The half-life of each isomeric state was obtained with a similar fit using a total time spectrum created from the  $\gamma$ -rays of the most intense transitions. Finally, an energy spectrum of individual delayed  $\gamma$ -rays (referred as ‘singles’) was created to obtain the efficiency-corrected intensities of the identified transitions, and so their decay branching ratios. The combination of all the previous information allowed to build a decay level-scheme for each nucleus, which are the main subjects of the physics discussion of this thesis presented in the next chapter.

---

### 7.1 Conditions for selection of delayed $\gamma$ -rays

---

#### PID cut

The events of each isotope were selected using a set of ‘PID cuts’, corresponding to the closed polygons defined on the particle identification plot shown in Figure 7.1. The selection condition demands that the  $(A/Q, Z)$  reconstructed values must lie inside the area enclosed by the cut of a specific nucleus. The number events selected for each case are listed in Table 8.

Isotope	Number of events
$^{92}\text{Se}$	$1.243 \times 10^5$
$^{93}\text{Se}$	$7.541 \times 10^4$
$^{94}\text{Se}$	$1.457 \times 10^4$

**Table 8:** Number of events of each isotope selected with the PID cuts

#### Prompt-flash cut

The cut on the  $E_\gamma$ -vs- $t_\gamma$  matrix shown in Figure 7.2 was defined to select and exclude the prompt-flash from the delayed  $\gamma$ -rays.

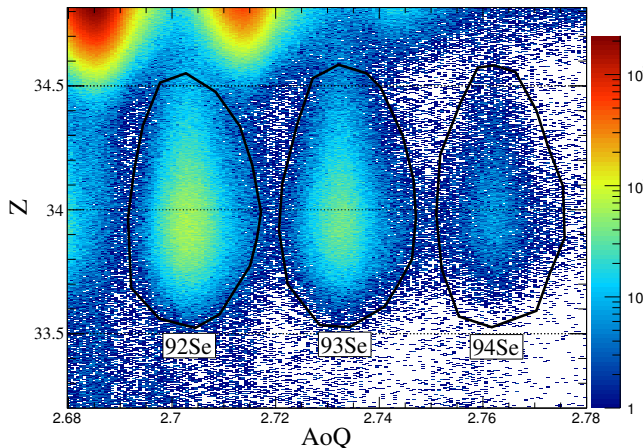


**Figure 7.1:** PID cuts for  $^{92,93,94}\text{Se}$ .

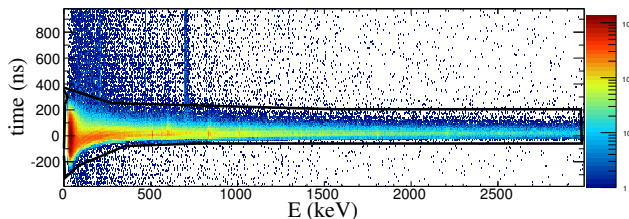


**Figure 7.2:** Prompt cut defined to exclude prompt  $\gamma$ -rays.

---

## 7.2 $^{92}\text{Se}$

---

### 7.2.1 Preliminary identification of isomeric transitions

Isomeric transitions were identified from the comparison of the energy spectrum in different time slots of the 100- $\mu\text{s}$  time window after ion implantation, see Figure 7.3. The time slots are of approximately 24  $\mu\text{s}$  width each and start at 0.2, 24.0, 48.0, and 72.0  $\mu\text{s}$ , respectively. The intensities of the peaks at 429, 503, 539, 637, 713, 898, 967, 1065, and 1250 keV are observed to decrease over time, as it can be seen on the peaks areas for different time slots. For most of the non-labelled peaks the intensity remains either constant or has no clear behaviour over time, following the criteria discussed in Section 6.2.5 of background peaks. The peaks at 67, 338, and 352 keV (marked in red) also present a decreasing intensity over time, however, their pattern is more irregular than the peaks previously mentioned and their nature is further clarified with the analysis of the following sections.

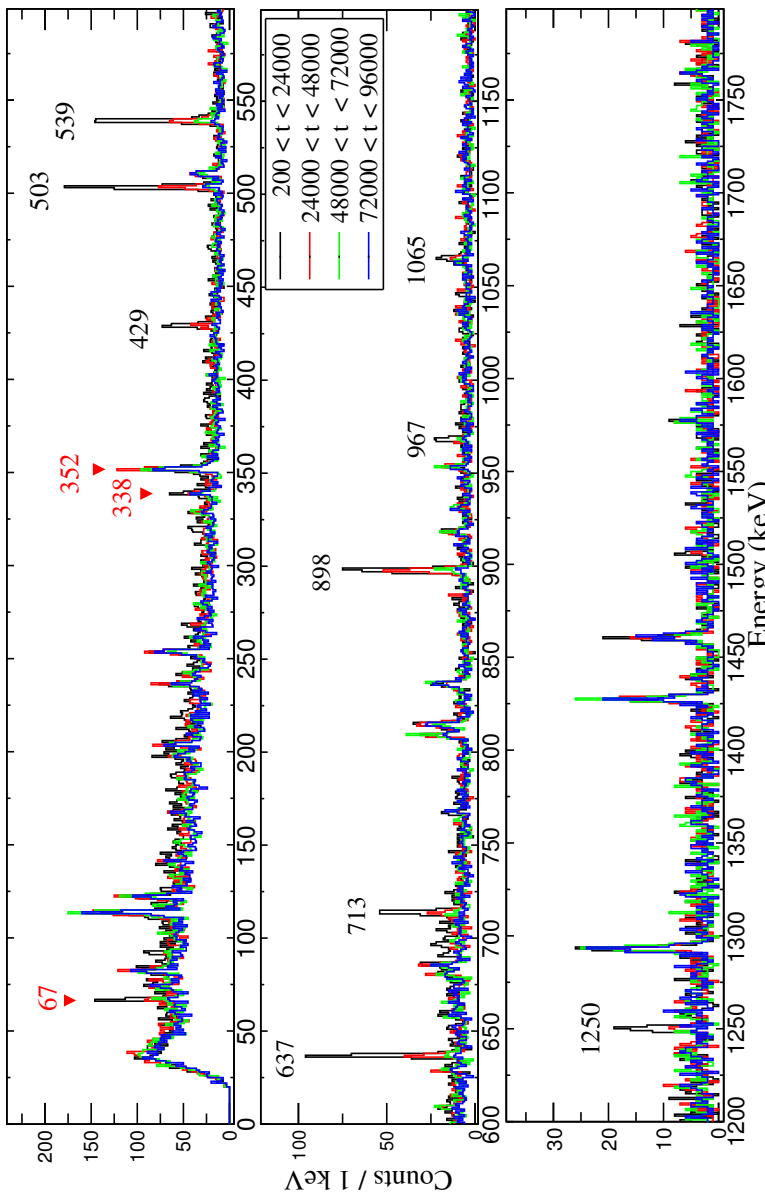


**Figure 7.3:** Energy spectrum in coincidence with  $^{72}\text{Se}$  for different time intervals after ion implantation. The range of the intervals, with  $\sim 24\text{-}\mu\text{s}$  width each, are shown in the legend. The tagged peaks are considered isomeric  $\gamma$  rays emitted after the decay of an isomeric state due to their decreasing intensity over time. Possible additional isomeric peaks are marked in red. Most of the non-labelled peaks are known background peaks.

## 7.2.2 Spectra of $\gamma\gamma$ coincidences

The energy spectrum of  $\gamma$ -rays in coincidence with each of the isomeric transitions identified in Section 7.2.1 was obtained as the projection on the x-axis of the  $\gamma\gamma$ -matrix horizontal section defined by the gate  $|E_y - E_0| \leq \Delta E$ , with  $E_0$  the transition energy and  $\Delta E = 2.5$  keV. The *real coincidence* condition introduced in Section 6.2.6 was demanded to clean the spectrum from spurious coincidences. In addition, a random-coincidence background spectrum created from the  $\gamma$ -rays that satisfy  $550 \text{ ns} \leq |t_y - t_0| \leq 1100 \text{ ns}$  was subtracted afterwards.

As an example, the  $\gamma\gamma$  coincident spectrum for the 503 keV transition is shown in Figure 7.4. The preliminary spectrum using only the energy gate (condition a) is plotted in red, the spectrum obtained after implementing the real coincidence condition (condition b) is plotted in green, and the final spectrum after random-background subtraction (condition c) is shown in blue. The condition c has almost no impact on the spectrum as it is reflected in the fact that the green and blue spectra are nearly identical. Coincident  $\gamma$ -rays interacting via Compton-scattering also satisfy all the analysis conditions demanded, so they necessarily make up part of the remaining background observed.

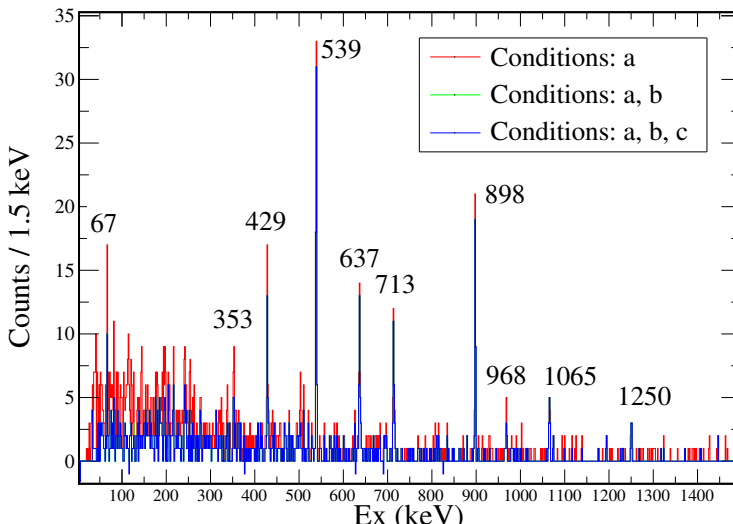


**Figure 7.4:** Energy spectra of  $\gamma$ -rays coincident with the 503 keV gate after the implementation of the different analysis conditions. See text for details.

The final  $\gamma\gamma$  coincident energy spectra are shown in Figures 7.5 and 7.6. The efficiency-corrected intensities of the peaks observed are listed in Table 9, and

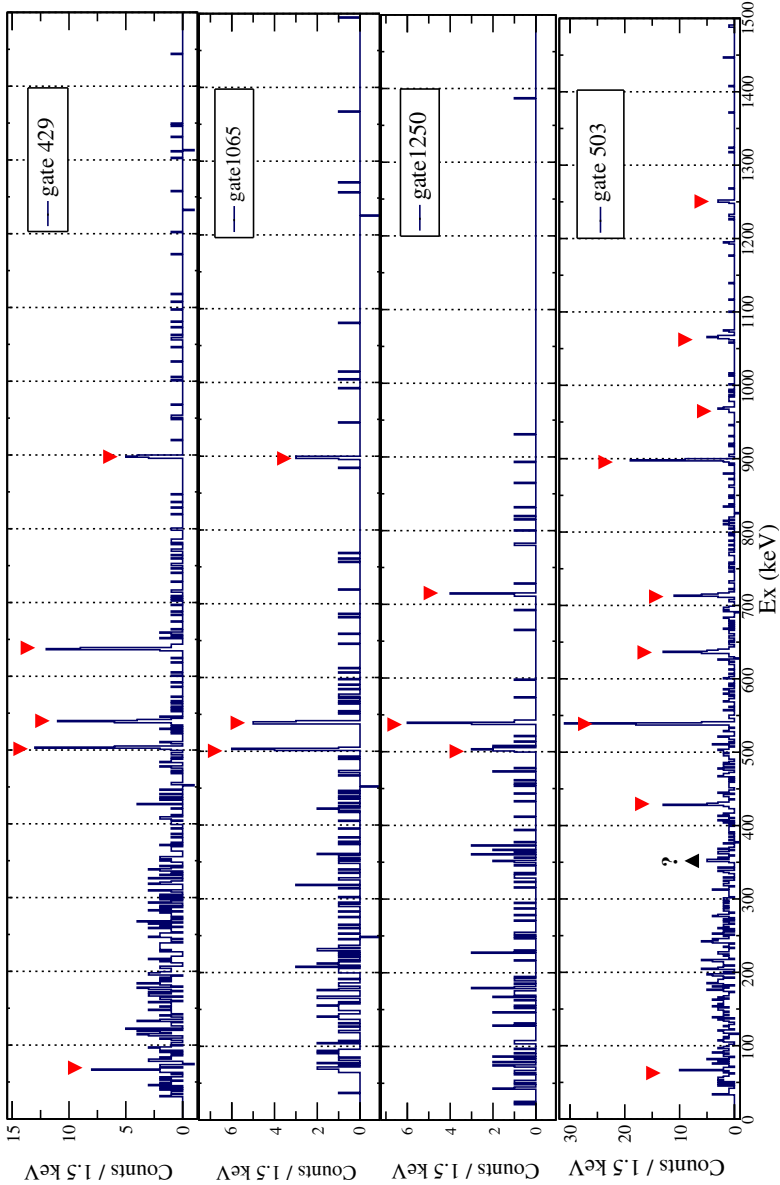


**Figure 7.5:**  $\gamma\gamma$  coincident energy spectra with 429, 1065, 1250, and 503 keV gates. Red triangles mark coincident peaks. Possible ones are denoted with a '?' symbol. Part of the remaining background corresponds to coincidences with Compton-scattered photons from the isomeric transitions.

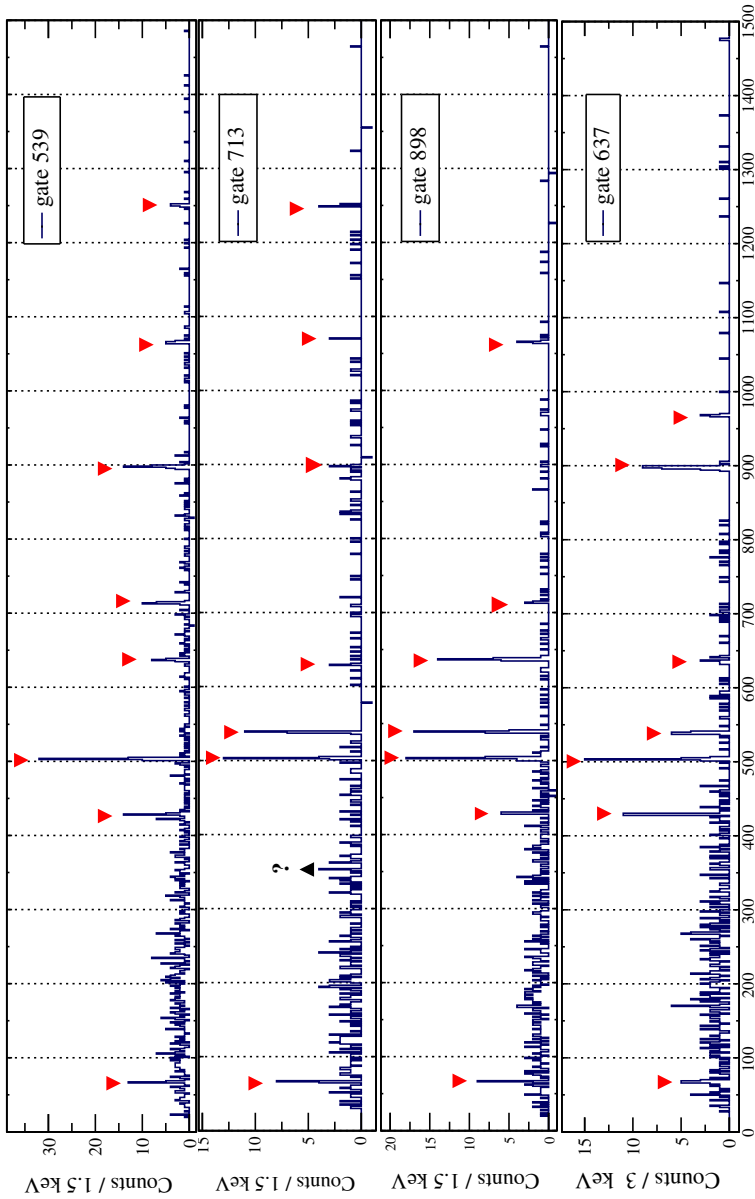


**Figure 7.6:**  $\gamma\gamma$  coincident energy spectra with 539, 713, 898, and 637 keV gates. See Figure 7.5 for details.

the details on the uncertainties determination is discussed in appendix A.2. A peak at 67(1) keV is present in the coincident spectra of all the energy gates except the 1065 and 1250 keV ones, confirming a transition at 67 keV for  $^{92}\text{Se}$ . No peak at 338(1) keV was found, so no transition at this energy value is proposed. Finally, a possible coincidence peak in the spectra of the 713 and 503 keV gates was observed at 352(1) keV, but the intensities are not large enough to confirm a transition at this energy value.

$E_y$ gate (keV)	E <sub>x</sub> - Intensity of coincident peak (counts)				
	67	429	503	539	637
429	10(3)	-	28(5)	29(5)	34(6)
503	9(3)	29(5)	-	76(9)	36(6)
539	14(4)	26(5)	74(9)	-	24(5)
637	8(3)	30(5)	34(6)	24(5)	-
713	10(3)	-	27(5)	27(5)	-
898	9(3)	15(4)	40(6)	42(6)	40(6)
1065	-	-	15(4)	18(4)	-
1250	-	-	11(3)	15(4)	-

$E_y$ gate (keV)	E <sub>x</sub> - Intensity of coincident peak (counts)				
	713	898	968	1065	1250
429	-	21(5)	-	-	-
503	32(6)	53(7)	11(3)	23(5)	15(4)
539	32(6)	48(7)	-	25(5)	22
637	-	40(6)	11(3)	-	-
713	-	7(3)	-	-	9(3)
898	8(3)	-	6(2)	14(4)	-
1065	-	12(3)	-	-	-
1250	10(3)	-	-	-	-

**Table 9:** Efficiency-corrected intensities of coincident peaks with the strongest isomeric transitions identified for  $^{92}\text{Se}$ . The errors shown are only statistical and do not include the uncertainty of the detection efficiency.

### 7.2.3 Half-life measurement

A preliminary spectra of the  $\gamma$ -ray detection time was obtained for each transition using the photo-peak counts, e.g. in a range  $|E_\gamma - E_t| \leq 3\sigma_t$ , with  $E_t$  and  $\sigma_t$  the centroid and standard deviation of the peak. A background time spectrum obtained with the  $\gamma$ -rays at the high and low-energy sides of the photo-peak was subtracted from the preliminary time spectrum. Prior to the subtraction, the background was scaled to the factor  $\Delta E_p / \Delta E_b$ , with  $\Delta E_p = 2 \cdot 3\sigma_t$  the width of the photo-peak in

terval, and  $\Delta E_b$  the width of the energy interval used to create the background spectrum. For example, the preliminary time spectrum of the 503 keV transition used only the photons in the energy range of  $|E_\gamma - 503.2| \leq 2.4$  keV, and the background time spectrum used the photons at the intervals  $493.1 \leq E_\gamma \leq 500.3$  keV and  $505.8 \leq E_\gamma \leq 508.5$  keV, leading to a scale factor of  $2 \times 2.4 / (7.2 + 2.7) = 0.48$ . The preliminary and background time spectra obtained for each transition are shown in Figure 7.8. The time spectra obtained after background subtraction are shown in Figure 7.9. A half-life of each transition was found fitting the decay-curve  $f(t_\gamma) = \exp \{p_0 + p_1 \cdot t_\gamma\} + p_2$ , and obtained as

$$T_{1/2} = \ln\{2\} \cdot \tau = -\frac{\ln\{2\}}{p_1}, \quad (112)$$

the values obtained are listed in table 10. Most of them agree within  $1\sigma$  uncertainty range, except for  $T_{1/2}(898)$  and  $T_{1/2}(1250)$ , which have the largest differences but still agree within  $1.5\sigma$ . In section 7.2.5 it will be shown that all these transitions are emitted following the decay of a common isomeric state, so its half-life was obtained with the fitting analysis of a total time spectrum obtained adding the time spectra of the individual transitions. This spectrum is shown in Figure 7.7, the value found is  $15.7 \pm 0.7$   $\mu$ s.

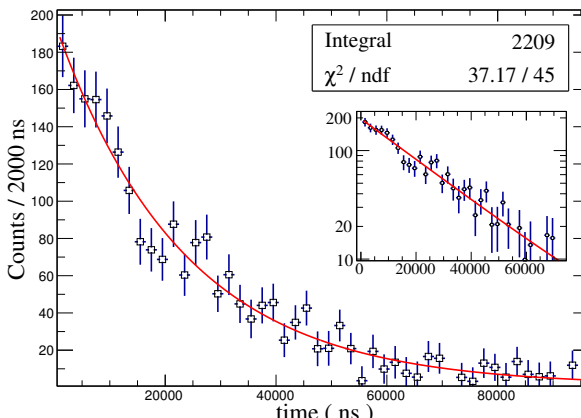


**Figure 7.7:** Time spectrum of the  $^{92}\text{Se}$  isomeric decay. Inset: Logarithmic.

#### 7.2.4 Singles intensities

The efficiency-corrected intensities of the transitions ( e.g. *singles intensities* ) were estimated from the photo-peak integral within the range  $|E_\gamma - E_t| \leq 3\sigma_t$  introduced in Section 7.2.3, considering only the isomeric decays detected within [500 ns,

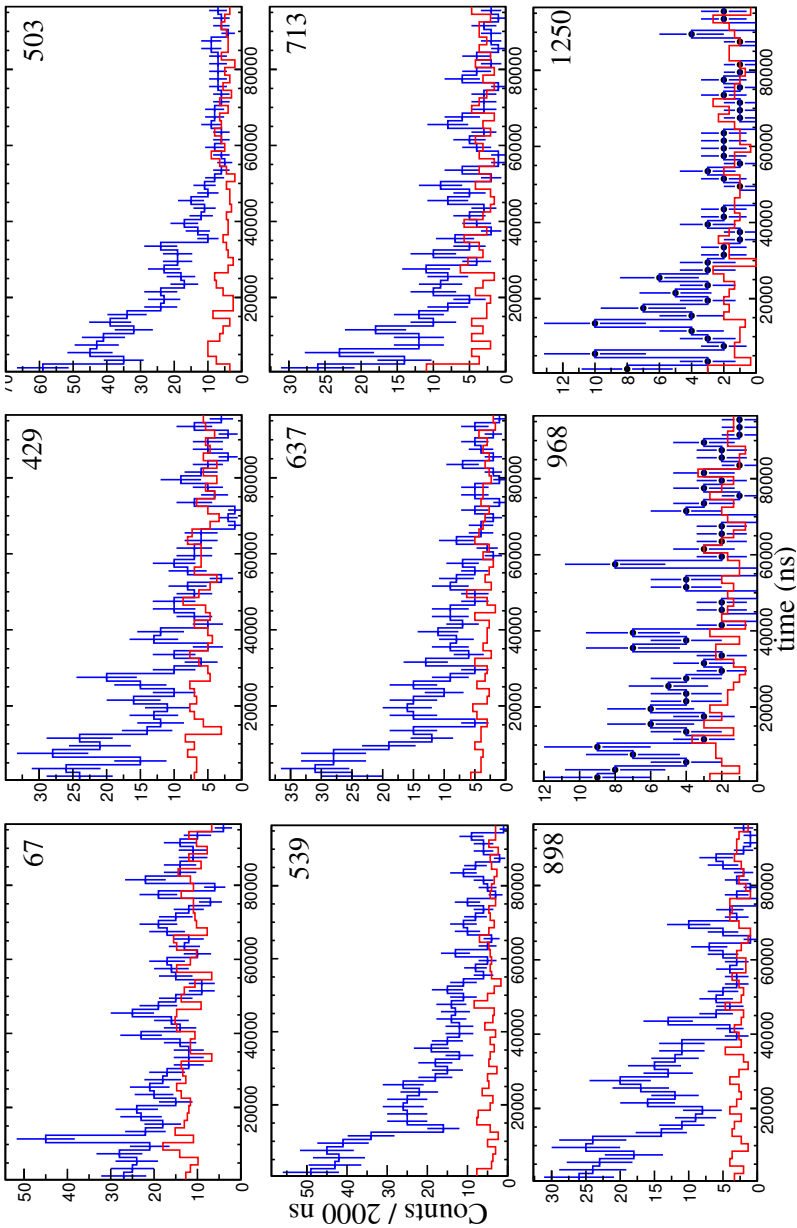


**Figure 7.8:** Blue:  $\gamma$ -ray detection time histogram of the counts in the photo-peak region of each transition. Red: Background time spectrum using counts on energy intervals near the photo-peak, and scaled according to the energy-width of the intervals.

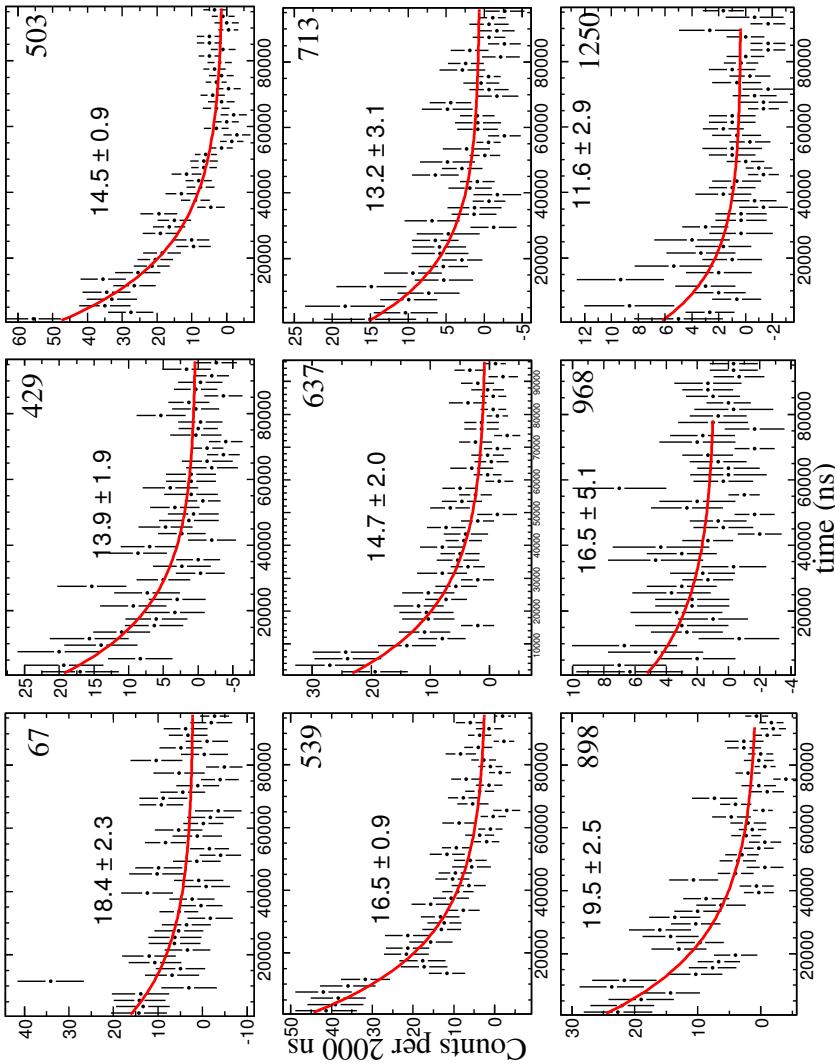


**Figure 7.9:** Background-subtracted time spectra of the identified transitions of  $^{92}\text{Se}$  (black), together with the fit functions used to deduce the half-life (red). The half-life obtained for each fit is shown together with the error.

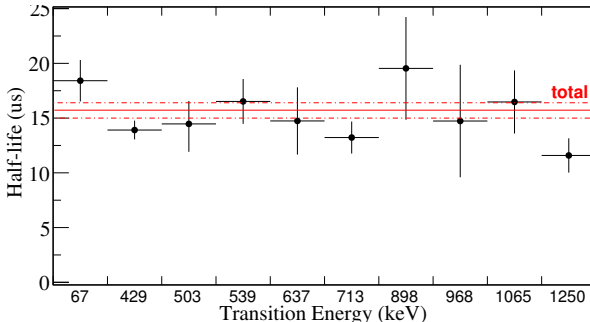


**Figure 7.10:** Half-lives obtained for each individual transition of  $^{92}\text{Se}$ .

86000 ns] after implantation. This interval is equivalent to  $\sim 5.5 \cdot T_{1/2}(^{92}\text{Se}^*)$ , so it contains  $\geq 96\%$  of the isomeric decay events. The minimum value of 500 ns was chosen to avoid any prompt-flash contamination. The  $\gamma$ -rays in the range (86000 ns, 99000 ns] were used as background and were subtracted to the singles spectrum after being scaled to the factor  $\Delta t_s/\Delta t_b$ , with  $\Delta t_s = 85.5 \mu\text{s}$  the time range used to estimate the intensities and  $\Delta t_b = 13 \mu\text{s}$  the background interval. The singles energy spectra before and after background subtraction are shown in Figure 7.11. The remaining background level of the peaks on the background-subtracted spectrum was estimated from the high and low-energy sides next to the peaks, and subtracted to the integral of the peak region to estimate accurately the counts due only to the nuclear transition, the details are discussed in appendix A.1. The absolute intensities obtained are listed in Table 10, as well as the intensities relative to the most intense transition.

Transition energy (keV)	Intensity	Half-life	
	Absolute (cts)	Relative (%)	( $\mu\text{s}$ )
67	154(25)	21(4)	$18.4 \pm 2.3$
429	249(23)	38(4)	$13.9 \pm 1.9$
503	609(28)	94(6)	$14.5 \pm 0.9$
539	650(30)	100(5)	$16.5 \pm 0.9$
637	343(22)	53(4)	$14.7 \pm 2.0$
713	252(22)	39(3)	$13.2 \pm 3.1$
898	554(27)	85(6)	$19.5 \pm 2.5$
968	87(14)	13(2)	$14.7 \pm 4.7$
1065	122(12)	19(2)	$16.5 \pm 5.1$
1250	70(10)	11(2)	$11.6 \pm 2.9$

**Table 10:** Efficiency-corrected singles intensities after background subtraction.

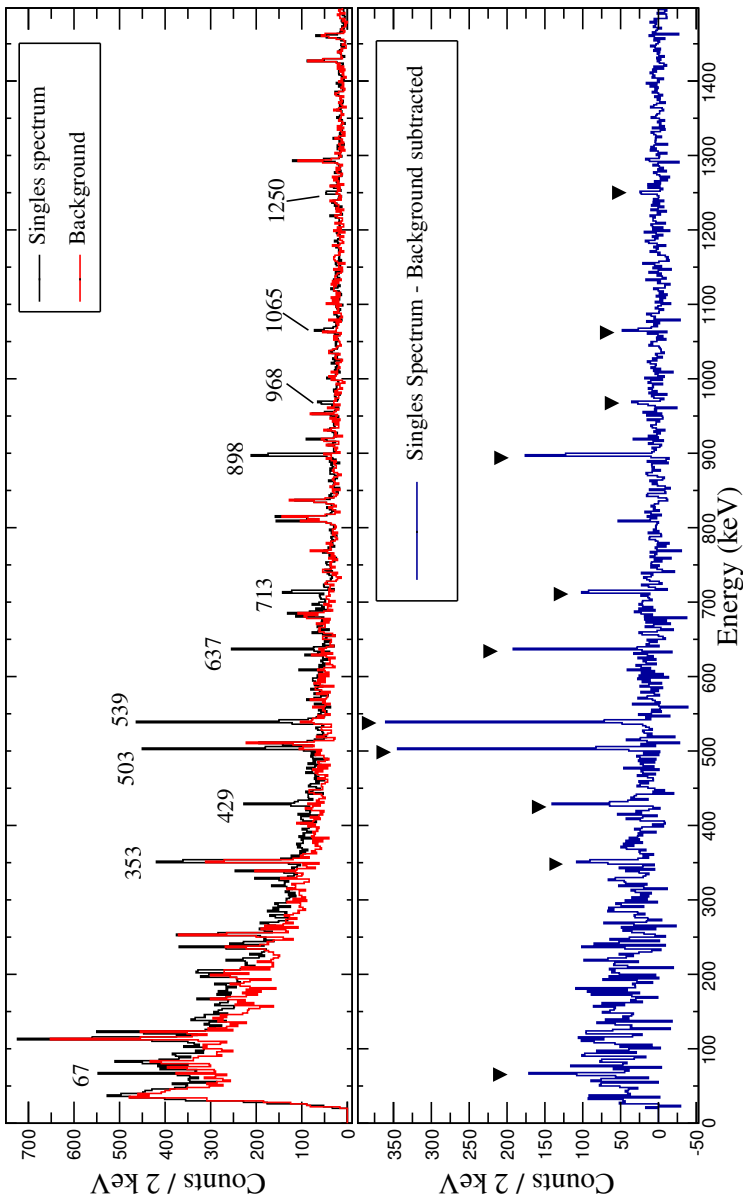


**Figure 7.11:** (Top) Singles energy spectrum obtained for  $500 \text{ ns} \leq t_\gamma \leq 86000 \text{ ns}$ , and the scaled background spectrum obtained with the  $\gamma$ -rays in the range  $86000 \text{ ns} \leq t_\gamma \leq 99000 \text{ ns}$ , see text for details. (Bottom) Background-subtracted energy spectrum used to compute the singles intensities of the peaks marked with black triangles.

## 7.2.5 Level Scheme

From the results obtained so far the following energy-sum relations are satisfied:

- $1065(1) \approx 429(1) + 637(1)$ ,
- $968(1) \approx 429(1) + 539(1)$ ,
- $1250(1) + 713(1) \approx 1065(1) + 898(1)$ ,
- $1250(1) + 713(1) \approx 429(1) + 637(1) + 898(1)$ ,
- $1250(1) \approx 898(1) + 352(1)$ .

Moreover, from the  $\gamma\gamma$  coincidence analysis it is observed that:

- The transition at 503 keV is in coincidence with all the other transitions identified.
- The transition at 539 keV is in coincidence with all the other transitions identified except for the one at 968 keV.
- The transitions at 429 and 637 keV are observed to be in coincidence. Both of them are not in coincidence with the transition at 1065 keV.
- The transition at 429 keV is not coincident with the transition at 968 keV.
- The transitions at 1250 and 713 keV are observed to be in coincidence, but neither of them is in coincidence with the transitions at 1065, 429, or 637 keV.
- The transition at 898 is in coincidence with the transitions at 1065, 429, and 637 keV.
- The transition at 898 is in coincidence with the transition at 713 keV but not with the transition at 1250 keV.
- The transition at 968 keV is coincident with the transitions at 637, 898 and 503 keV.

Finally, the relative intensities found in the singles spectrum reveal that:

- $I_{503} \approx (I_{898} + I_{1250})$ , with a difference of 1(6)%.
- $I_{637} \approx (I_{429} + I_{968})$ , with a difference of 1(5)%.
- $I_{539} \approx (I_{1065} + I_{713} + I_{429})$ , with a difference of 4(7)%.
- $I_{898} - (I_{1065} + I_{637}) \approx 13(6)\% \neq 0$ .

## Decay path

These observations previously listed led to the unique ordering of the transitions shown in Figure 7.12. The possible transition at 352 keV is confirmed since the transitions at 713 and 898 keV are in coincidence, and the combined intensities of the 1065 and 637 keV transitions are 13(6)% lower than the intensity at 898 keV. However, a direct measurement of the 352 keV peak intensity from the singles energy spectrum (Figure 7.11) was not found to be reliable since the strong contribution of the background peak at 353 keV introduces a large error to the intensity of the remaining peak after background subtraction.

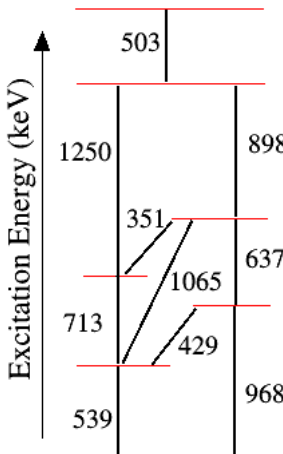


**Figure 7.12:** Unique placement of the identified transitions that fulfils the conclusions obtained from Sections 7.2.1, 7.2.2, and 7.2.4.

Despite the placement of the transitions is unique, the *direction* of de-excitation cannot be deduced, so a scenario where the de-excitation occurs from the bottom to the top is in principle possible as well. This possibility is disregarded from the comparison with the results obtained by the in-beam spectroscopy measurements conducted simultaneously (see Appendix B). They allow an assignment of the lowest excited states based on the transition intensity observed, and placed the  $2_1^+$  and  $4_1^+$  states at 539(7) and 1253(10) = 539(7) + 714(7) keV, respectively.

## The 67-keV transition

The only possibility left for the 67 keV transition is to be placed on top of the 503 keV transition. The placement is supported by the  $\gamma\gamma$  coincidence analysis, where a peak at 67 keV showed up in coincidence with all the found transitions except the ones at 1250 and 1065 keV. The absence of a 67 keV coincident peak in these

two cases can be understood considering that the expected counts on a peak at  $E_x$  for the energy coincidence spectra of a transition at  $E_y$  are given by

$$I_{\text{gate } E_y}(E_x) = I_{\text{abs.}}(E_y) \times \epsilon(E_y) \times \epsilon(E_x) \times b_\gamma(E_y \leftrightarrow E_x), \quad (113)$$

with  $I_{\text{abs.}}(E_y)$  the absolute intensity of the transition at  $E_y$  (listed in

Table 10),  $\epsilon(E_x)$  and  $\epsilon(E_y)$  the EURICA efficiencies at the energies of  $E_x$  and  $E_y$ , and  $b_\gamma(E_y \leftrightarrow E_x)$  the branching ratio between the transitions involved. Therefore, for the transition at 1065 keV:

$$\begin{aligned} I_{g1065}(67) &= I_{\text{Abs.}}(1065) \times \epsilon(1065) \times \epsilon(67) \times b_{898} \times b_{1065} \times b_{503} \\ &= 122 \times 0.51 \times 1.18 \times \frac{I_{898}}{I_{503}} \times \frac{I_{1065}}{I_{898}} \times \frac{I_{67}}{I_{503}} \\ &= 122 \times 0.51 \times 1.18 \times 0.044 \approx 3 \text{ counts}, \end{aligned} \quad (114)$$

this value is not large enough to claim the existance of a peak in the remaining background nearby. For the transition at 1250 keV:

$$\begin{aligned} I_{g1250}(67) &= I_{\text{Abs.}}(1250) \times \epsilon(1250) \times \epsilon(67) \times b_{1250} \times b_{503} \\ &= 70 \times 0.46 \times 1.18 \times \frac{I_{1250}}{I_{503}} \times \frac{I_{67}}{I_{503}} \\ &= 70 \times 0.46 \times 1.18 \times 0.025 \approx 1 \text{ count}. \end{aligned} \quad (115)$$

The difference of  $\sim 74\%$  between the relative intensities of the transitions at 67 and 503 keV cannot be balanced by the intensity of additional non-identified transitions since the EURICA photo-peak efficiency was high enough to detect a transition with such a high intensity up to energies  $\sim 2$  MeV. Therefore, the discrepancy must be caused due to the decays of the 67 keV transition where internal conversion occurs instead of the emission of a  $\gamma$ -ray. In fact, the total intensity is given by

$$I_T(67) = I_{\text{I.C.}} + I_\gamma = (\alpha + 1) \cdot I_\gamma, \quad (116)$$

where  $\alpha$  corresponds to the internal conversion coefficient. Assuming that no transitions with a large intensity are missing then  $I_T(67) = I_{503}$ . Hence, the experimental conversion coefficient for this transition is

$$\alpha_{\text{exp}} = I_{503}/I_{67} - 1 = 2.95(68). \quad (117)$$

The dominant multipolarity of the 67 keV  $\gamma$ -ray was inferred from the comparison between the experimental conversion coefficient obtained and a theoretical evaluation performed with the BrICC conversion coefficient calculator tool [69]. The results obtained with BrICC are presented in Table 11. An agreement within less than  $1-\sigma$  difference is obtained for E2, so this is the multipolarity proposed.

Atomic Shells	Multipolarity		
	M1	E2	M2
All	0.31	3.62	4.58
K+L1+L2	0.30	3.38	4.42

**Table 11:** BrIcc Conversion coefficient obtained for a 67(1) keV of an atom with Z=34. Values for all and deepest atomic shells ( K+L1+L2 ) are shown.

Since the multipolar order and the conversion coefficient of the 67 keV transition are known, then the Weisskopf estimate of the Half-life of this transition yields:

$$\begin{aligned}\tau_\gamma &= \frac{1}{W_{\text{Weiss.}}(E2)} = \frac{1}{7.3 \times 10^7 (92)^{4/3} (67 \times 10^{-3})^5} \\ &= 2.44 \times 10^{-5} \text{ s.} \\ T_{1/2}^{\text{Weiss.}} &= \frac{\tau_\gamma \log(2)}{1 + \alpha_{Icc}} = \frac{2.44 \times 10^{-5} \times 0.693}{1 + 2.95} = 8.9 \mu\text{s.}\end{aligned}\quad (118)$$

This value is close and on the same order of magnitud of the experimental half-life measured (15.7(7)  $\mu\text{s}$ ) for the isomer state. Therefore, it is proposed that the 67 keV transition is in fact the isomeric decay observed for  $^{92}\text{Se}$ .

### Tentative spin-parity assignments and level scheme

The level scheme obtained is shown in Figure 7.13. Each level is represented by a horizontal line, the excitation energy in keV is indicated next to the level. The width of the arrows connecting different levels is proportional to the intensity observed of the transition, with the energy shown in blue. The fraction of the 67 keV transition observed via  $\gamma$ -ray decay corresponds to the black area of the arrow.

The excited state at 539 keV is assigned to the yrast  $2_1^+$ , following the systematics of the  $2_1$  lowest excited states identified for the isotopic chain [24, 35, 36]. This follows the known fact that for almost all even-even nuclei the lowest excited level connecting via  $\gamma$ -ray decay to the ground state has  $J^\pi = 2^+$  [103]. The level at 1252 keV decays exclusively to the  $2_1^+$  state and not to the 968-keV, which is lower in excitation energy. This behaviour is common of yrast states, so it is associated to the  $4_1^+$  level.

For the 968-keV state, a spin  $J = 0$  is excluded since transitions of the type  $0^+ \rightarrow 0^+$  do not occur via  $\gamma$ -ray decay. A  $J=1$  assignment does not match the intensities observed for the transitions to the  $2_1^+$  and  $0_1^+$  levels: The strength of a hypothetical  $M1$  968-keV over a  $M1$  429-keV transition would be, according to Section 4.2.3, several times stronger.  $J=3^+$  is ruled out since the transition connecting the ground-state  $0_1^+$  is rather prompt: it did not show a decay time relative to other transitions, which does not fit with a potential  $M3$  decay which is rather slow compared to an  $E2$ . The assignment  $J^\pi=2_2^+$  fits better the intensities ob-

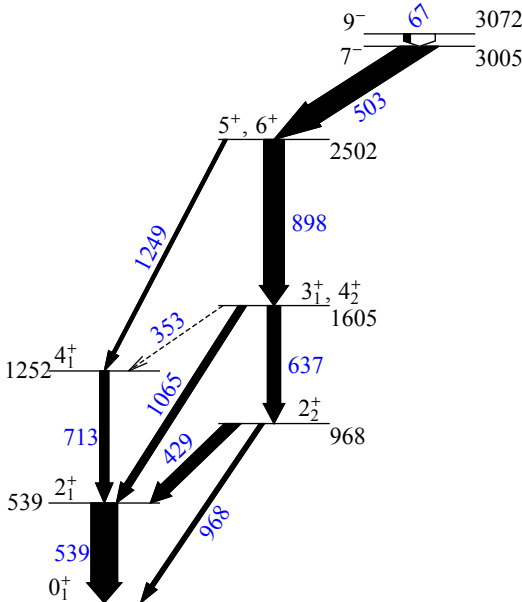


**Figure 7.13:**  $^{92}\text{Se}$  Level scheme obtained via isomeric decay  $\gamma$ -ray spectroscopy. Spin-parity assignments are tentative, see text for details.

served. In that case, this  $2_2^+$  would be below the  $4_1^+$  which is an indication of non-axial deformation. This hypothesis is qualitatively consistent with both models of Davydov and Wilet-Jeans where the decay strength is stronger for the  $2_2^+ \rightarrow 2_1^+$  in comparison to the  $2_2^+ \rightarrow 0_1^+$  transition.

The strong intensities of the 898 and 637 keV transitions compared to the 1250, 353, and 1065 keV ones suggest a band structure formed by the levels at 2502 and 1605 keV, nevertheless, presenting strong interband decays to the yrast-band. Therefore, they are likely to have the same parity as the 968 keV state, which is positive. The 1605 keV level can have spins  $(3_1^+, 4_2^+)$ , since the assignments  $J = 0, 1, 2, 5$  make not much sense with the intensities/transitions observed. For the 2502 keV level,  $J=4$  is ruled out since there is no  $E2$  decay to any of the  $2^+$  states (which would be strong due to the large energy gap). The lowest spins that match the decay pattern observed are  $(5^+, 6^+)$ .

The levels at 3005 and 3072 keV have the same parity and differ at least (and most likely) by two units of angular momentum, given the  $E2$  character of the transition connecting them (see Table 2). However,  $J_{3005}^\pi$  has to be such that transitions connecting to the 1605 or 1252 keV levels are not favoured, but only to the 2502 keV level. Similarly,  $J_{E=3072}^\pi$  is such that a decay to the 2502 keV state

is not competitive to the 67 keV transition (or does not exist at all). Given these constraints, positive-parity assignments where  $J_{3005}^+ \leq 6^+$  are not likely, the  $J^\pi = 6^+$  case would have a strong  $E2$  decay to the  $4_1^+$  (and the potential  $4_2^+$ ). Negative-parity assignments  $J_{3005}^- \leq 5^-$  are not likely to decay to a  $(5^+, 6^+)$  state instead of the lower spin ones. Moreover, the  $J_{3005}^- = 5^-$  case leads to  $J_{3072}^- = 7^-$  which would have a 570 keV  $M2(E1)$  decay to the  $5^+(6^+)$  state at 1605 keV with a half-life and decay strength much faster and stronger with respect to the intensity and half-life found for the 67-keV transition, but such prompt transition is not observed. The possible transitions with the lowest-spin assignments for these two levels are:

$$8^- \rightarrow 6^-, \quad 9^- \rightarrow 7^-, \quad 9^+ \rightarrow 7^+, \quad 10^+ \rightarrow 8^+ \quad (119)$$

In Section 8.1, it will be shown that the most likely option corresponds to  $9^- \rightarrow 7^-$ , which is the assignment used.

### Comparison with available spectroscopic information

The first spectroscopic information of  $^{92}\text{Se}$  was reported in 2012, see Ref. [104]. An experiment conducted by D. Kameda *et al.* found the isomeric  $\gamma$  decays at 503.4, 538.8, and 897.8 keV. These transitions were proposed to be emitted after the decay of an isomeric state with a half-life of  $T_{1/2} = 10.3_{2.8}^{5.5} \mu\text{s}$ . These results are consistent with the observations of the present thesis, for instance, the same transitions were observed with similar relative intensities and the half-life of the isomeric state agrees within error bars. Moreover, the level scheme proposed explains why only the transitions at 503, 539 and 898 keV were reported in Ref [104]: Their intensities are the only ones large enough to be clearly detected above the background despite the lower-statistics of the energy spectrum caused by a lower number of implanted fragments ( $\sim 6.4 \times 10^4$   $^{92}\text{Se}$ ), but also to a lower efficiency of the  $\gamma$ -ray clover detector used in that experiment when compared to EURICA.

In 2017, the results of the in-beam spectroscopy measurements conducted in the 2015 SEASTAR campaign have been published by S. Chen *et al.* [24]. The transitions at 429(7), 539(9), 624(13), 715(7), 958(22), and 1061(14) were reported and placed in a level scheme, see Appendix B. These results are consistent with the ones found in the present thesis.

Summarizing, all the spectroscopic information reported previously for  $^{92}\text{Se}$  has been confirmed in this thesis, with substantial improvements in the resolution of the transition energies and the isomeric state half-life. Additionally, three new transitions at 67, 352, and 1250 keV were found, and the level scheme has been extended in excitation energy from 1605 up to 3072 keV, placing the 898 and 503 keV transitions originally observed by Kameda. The branching ratios of the respective transitions have been found, together with the conversion coefficient of the 67 keV transition.

## 7.3 $^{94}\text{Se}$

### 7.3.1 Identification of isomeric transitions

The isomeric  $\gamma$ -decays were found from the energy spectrum in coincidence with  $^{94}\text{Se}$  for three different  $\gamma$ -ray detection time intervals of  $\sim 7 \mu\text{s}$  width each, see Figure 7.14. For detection times  $t_\gamma > 7 \mu\text{s}$  no peaks were visible, so in the analysis of this nucleus only  $\gamma$ -rays in the interval  $180 \leq t_\gamma \leq 7000 \text{ ns}$  are considered. Four peaks at 470(1), 495(1), 642(1), and 822(1) keV presented an intensity decreasing over time, so they are proposed to be  $^{94}\text{Se}$  isomeric transitions. The two peaks at 752 and 1180 keV with much weaker intensities are considered at this point as candidates of transitions as well.

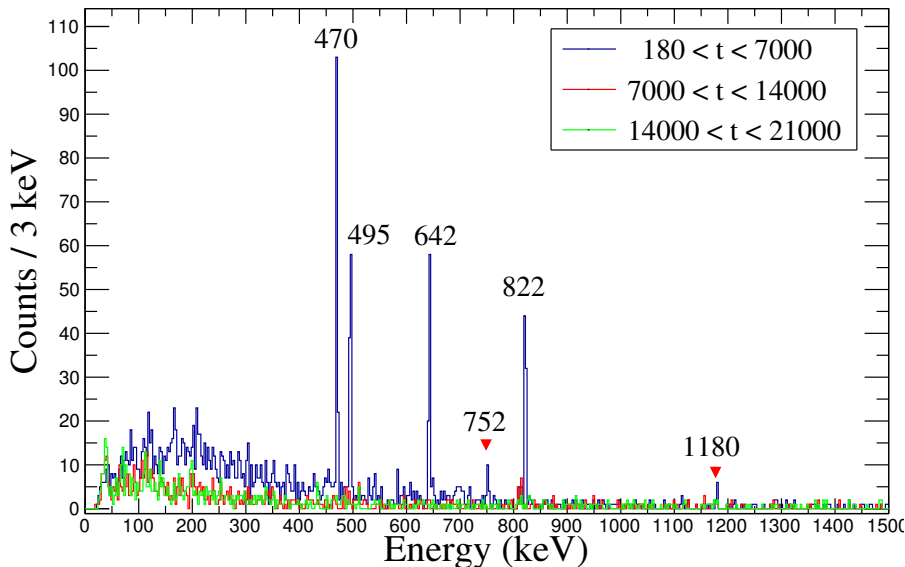


**Figure 7.14:** Energy spectra in coincidence with  $^{94}\text{Se}$  for different time intervals after ion implantation. The range of the intervals, of  $\sim 7\text{-}\mu\text{s}$  width each, are shown in the legend. The tagged peaks are new isomeric  $\gamma$  transitions as it can be seen in their decreasing intensity over time. The red triangles mark the additional peaks of possible weaker isomeric transitions.

### 7.3.2 Spectra of $\gamma\gamma$ coincidences

The energy spectra  $\gamma\gamma$ -rays in coincidence with the transitions previously identified are shown in Figure 7.15. The real coincidence condition, as well as

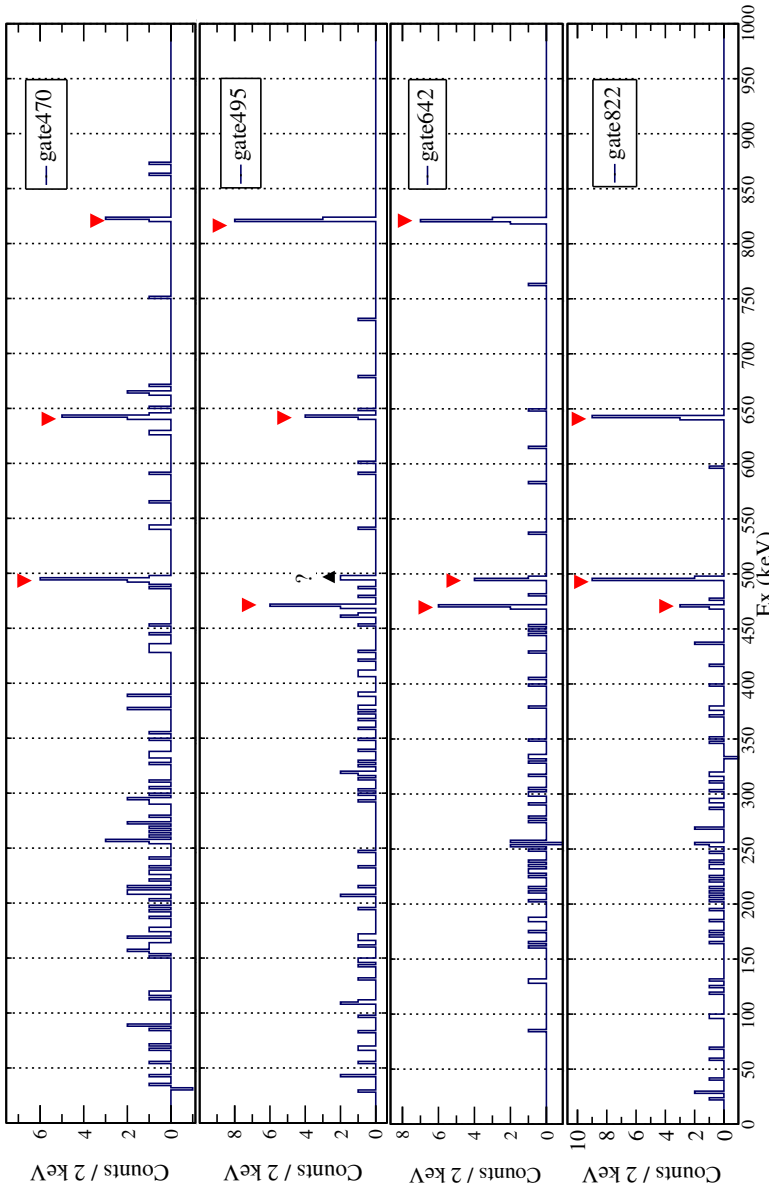


**Figure 7.15:** Energy spectra in coincidence with the 470, 495, 642, and 822 keV gates. Red triangles mark the coincident peaks. The conglomeration of 3(2) counts at 495 keV in the coincidence spectrum of the 495 keV transition is denoted with the '?' symbol. Part of the remaining background in the spectra correspond to coincidences with Compton-scattered photons of the isomeric transitions.

the random-coincidence background subtraction, have been applied following the similar procedure described in Section 7.2.2. The efficiency-corrected intensities of the coincident peaks observed are shown in Table 12.

$E_y$ gate (keV)	$E_x$ Peak intensity (counts)			
	470	495	642	822
470	-	11(4)	12(4)	7(3)
495	10(4)	3(2)	7(3)	19(6)
642	10(4)	7(3)	-	20(6)
822	5(3)	15(5)	18(5)	-

**Table 12:** Same as table 9, but for the  $^{94}\text{Se}$  case.

The four isomeric  $\gamma$ -rays identified are observed to be in coincidence with each other, so they are emitted in a cascade. On the other hand, no coincident peaks at 752 or 1180 keV were observed. In the coincidence spectrum with the 495 keV transition there are 3(2) counts at this same energy value. Given this low intensity, a transition with the same energy (implying the existence of a doublet of transitions both at 495 keV) is not proposed.

### 7.3.3 Half-life measurement

The time spectra of the isomeric  $\gamma$ -rays already identified plus the peaks at 752 and 1180 keV were obtained with the procedure described in Section 7.2.3. The preliminary time spectra and the random-coincidence background spectra are shown in Figure 7.16. The background-subtracted time spectra and the fits of the decay curves are shown in Figure 7.17.

The effective half-lives obtained for each energy can be found in Table 13. The values agree within error bars, including the 752 and 1180 keV peaks whose errors are the largest due to the low peak statistics. This suggests that all these transitions are emitted after the decay of the same isomeric state, so their time spectra were added to form a total time spectrum used to extract the half-life of the isomeric state, see Figure 7.18. The fit analysis leads to a value of  $0.68(5) \mu\text{s}$ .

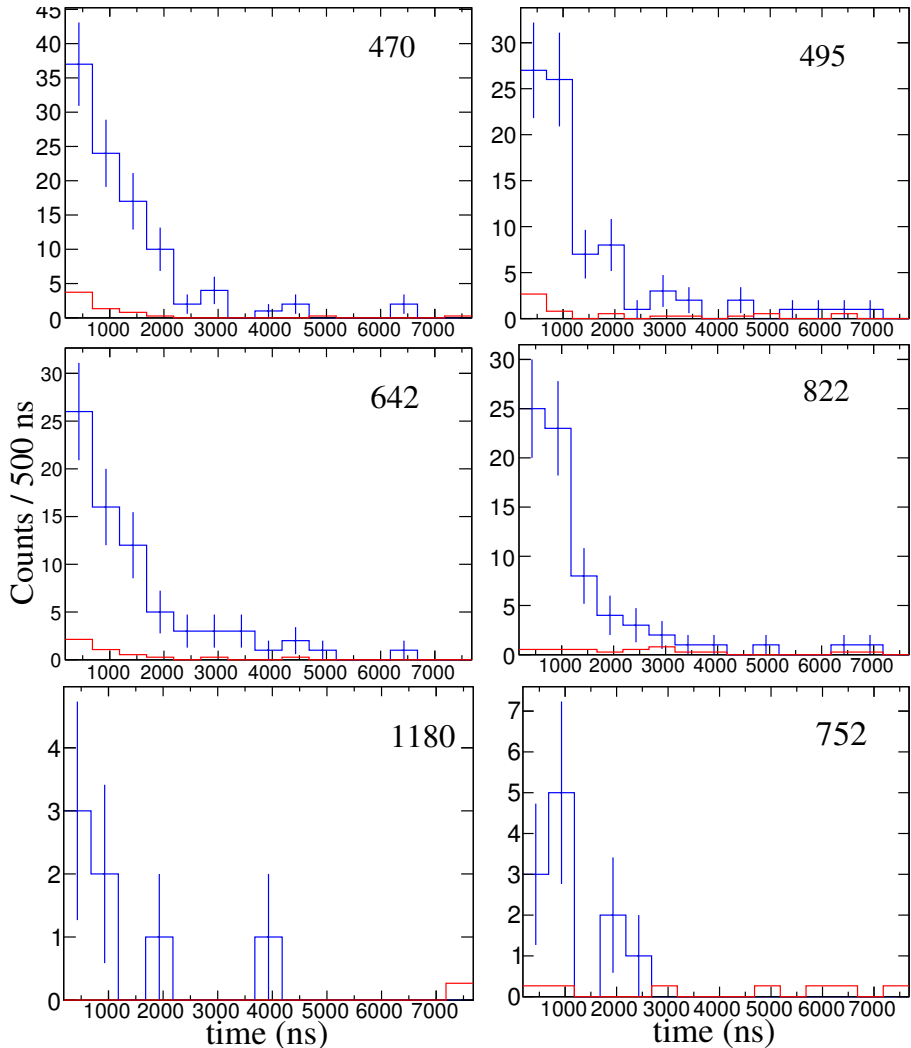


**Figure 7.16:** Blue: preliminary time spectrum of the isomeric  $\gamma$ -rays identified for  $^{94}\text{Se}$  and the additional peaks at 752 and 1180 keV. Red: Background time spectrum using energy intervals near the photo-peak, scaled accordingly to the width of the energy intervals used.

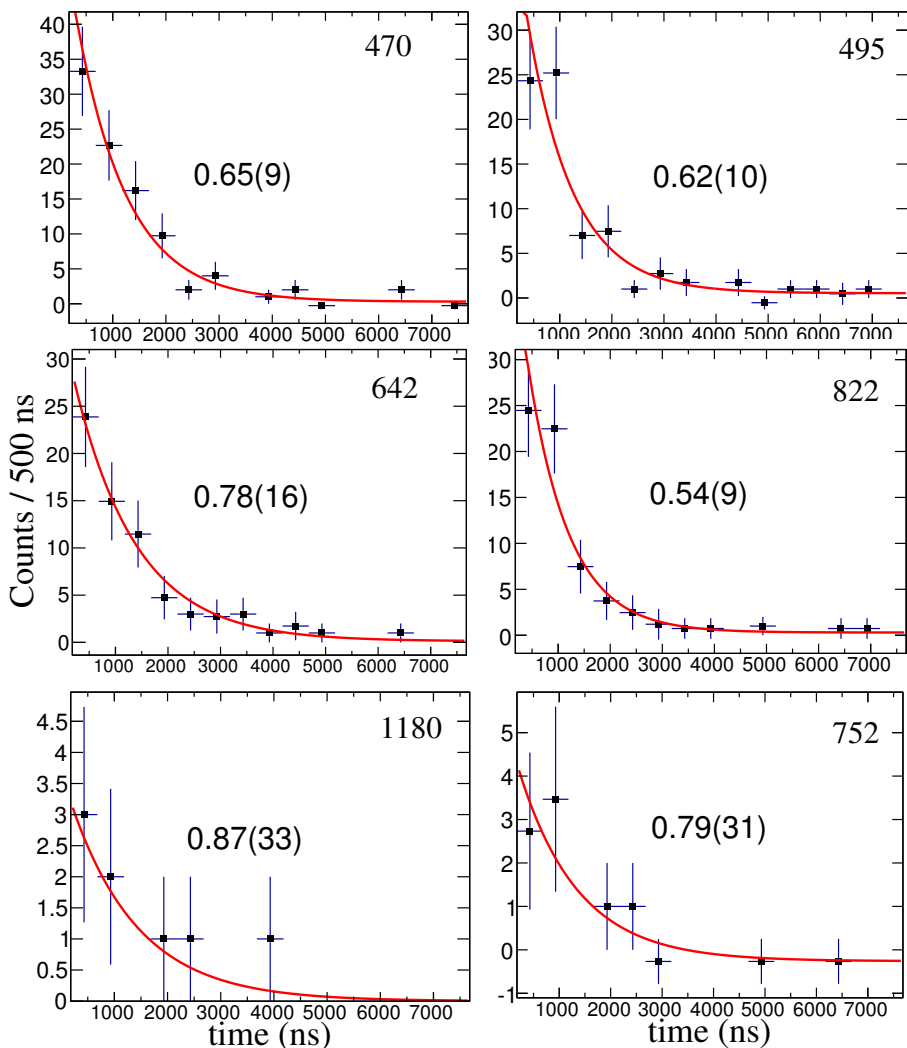


**Figure 7.17:** Background-subtracted time spectra of the peaks considered in Figure 7.16 (black), together with the fit functions used to deduce the half-life (red).

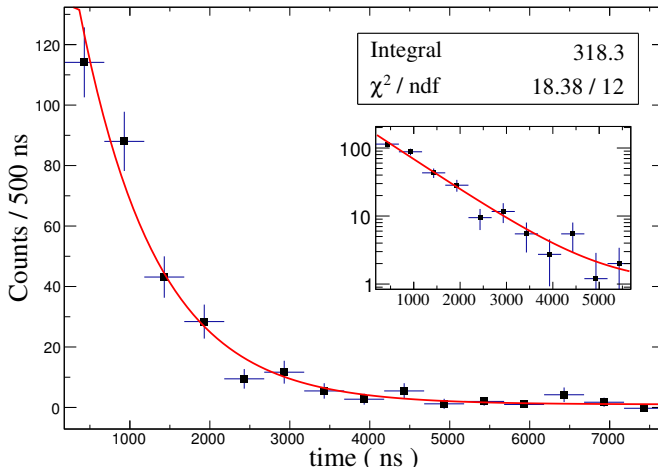


**Figure 7.18:** Background-subtracted total time spectrum of the  $^{94}\text{Se}$  isomeric decay. The inset shows the spectra in log scale.

### 7.3.4 Singles intensities

The efficiency-corrected intensities of each isomeric transition and the two peaks at 752 and 1180 keV were estimated in a similar way as in Section 7.2.4. The preliminary energy spectrum in the range of [180 ns, 7180 ns] was used to estimate the intensities, this interval corresponds to  $\sim 10.5 \cdot T_{1/2}(^{94}\text{Se}^*)$ , covering almost all the isomeric decays occurred. The background energy spectrum was obtained from the interval [9000 ns, 23000 ns] and it was subtracted to the preliminary energy spectrum after being scaled to the factor  $(180 - 7180)/(23000 - 9000) = 0.5$ , the ratio of the two time intervals. The singles energy spectra before/after background subtraction are shown in Figure 7.19 and the intensities listed in Table 13.

Transition energy (keV)	Intensity		Half-life ( $\mu\text{s}$ )
	Absolute (cts)	Relative (%)	
470	124(12)	100(9)	0.65(9)
495	105(11)	85(13)	0.62(10)
642	101(11)	82(13)	0.78(16)
752	13(4)	10(3)	0.79(31)
822	118(11)	91(12)	0.54(9)
1180	13(3)	10(3)	0.87(33)

**Table 13:**  $^{94}\text{Se}$  Efficiency-corrected singles intensities after background subtraction.

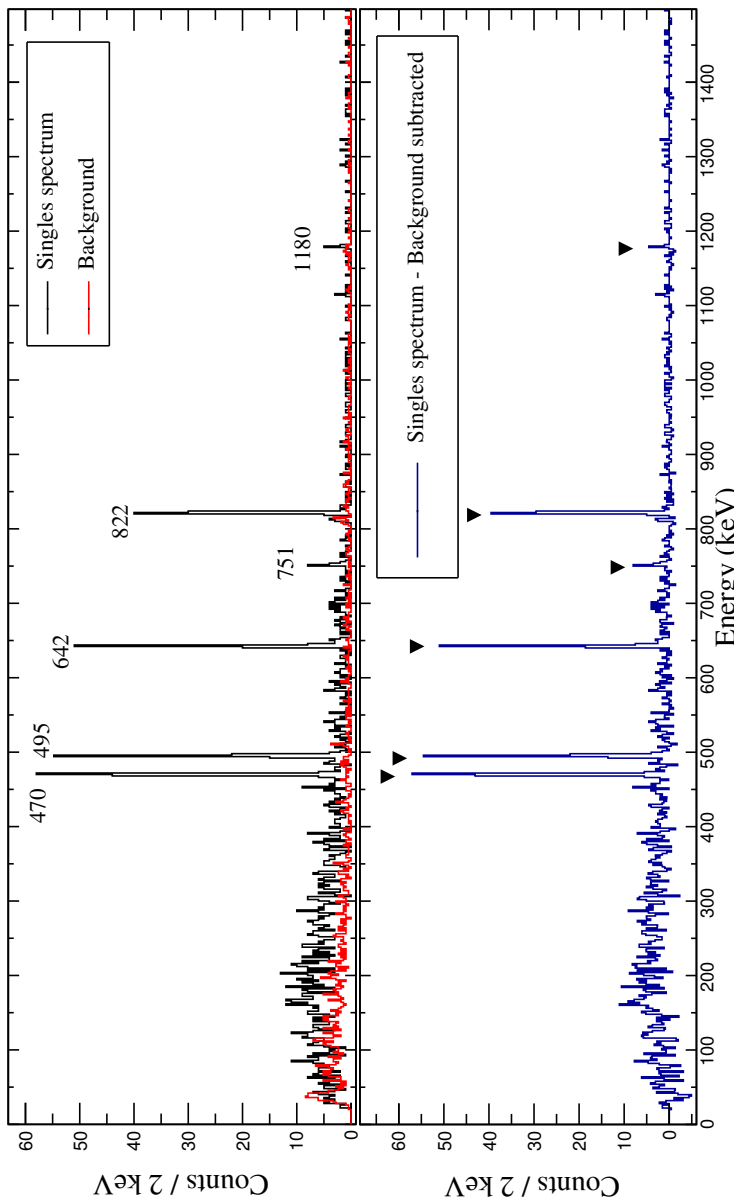


**Figure 7.19:** (Top) Singles energy spectrum in the range  $180 \leq t_{\gamma} \leq 7180$  ns, and the background spectrum obtained with  $\gamma$ -rays detected in the interval  $9000 \leq t_{\gamma} \leq 23000$  ns after being scaled accordingly to the ratio of the widths of both intervals considered. (Bottom) Background-subtracted singles energy spectrum used to compute the intensities of the peaks marked with black triangles.

A partial energy spectrum in the region [700,1200] keV is shown in Figure 7.20. The energy binning of 0.75 keV reduced the chance of adding remaining background to a transition peak, without spreading the peak over many counts. The presence of the 752 and 1180 keV transitions is rather clear.

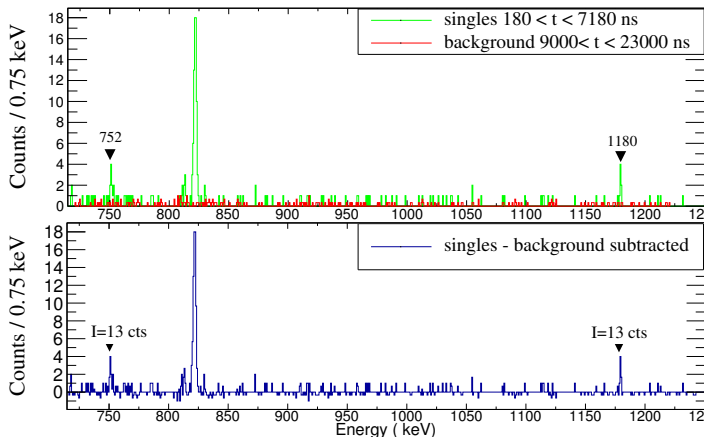


**Figure 7.20:** Same as Figure 7.19, for the range 640-1250 keV, with 0.75 keV/bin.

### 7.3.5 Level Scheme

The transitions at 470, 495, 642, and 822 keV must be placed in one cascade in the level scheme since they see all each other in the coincidence spectra. Furthermore, the relative intensities of the 495 and 642 keV transitions are the same and agree within error bars with the intensities of the transitions at 822 keV and 470 keV. However, these observations are not enough to rule out a unique placement of the transitions in a single cascade, as each of the  $4! = 24$  permutations lead to cascades consistent with the singles intensities and  $\gamma\gamma$  coincidences.

The in-beam spectroscopy measurements simultaneously conducted (see Appendix B) offer useful insights that allow reconstructing the  $^{94}\text{Se}$  low-lying level scheme: Two transitions at 475(10) and 640(7) keV were observed; the Doppler-corrected energy spectrum reveals that the peak at 475(10) keV presents the largest intensity and therefore should correspond to the transition from the first excited state (proposed to be the  $2_1^+$  level) to the ground state. Also, the peak at 640(7) keV was observed in coincidence with the one at 475(10) keV, consequently, it must correspond to a transition from a higher excited state decaying to the  $(2_1^+)$  which was proposed to be the  $4_1^+$  level. Additionally, three peak-like structures were observed at 830(30), 1290(30), and 1580(30) keV with a significance of  $3.6\sigma$ ,  $3.0\sigma$ , and  $3.7\sigma$ , respectively ( $5\sigma$  of significance was required to claim a new transition).

The combination of the results of both in-beam and decay spectroscopy led to the following conclusions:

1. Only one of the peaks at 470(1) or 495(1) keV was measured in the in-beam measurements since no self-coincidence was reported.
2. The pair of peaks 475(10)-640(7) keV found in the in-beam data correspond either to the pair 470(1)-642(1) keV or 495(1)-642(1) keV, of transitions observed in the isomeric decay
3. The peak at 642(1) keV must correspond to the transition from the second excited state to the first one.
4. One of the peaks at 470(1) or 495(1) keV must correspond to the transition of the first excited state to the ground state. The other transition was observed only in the isomer-decay data and therefore must be emitted from a state higher in excitation energy than the second excited state.
5. The peak-like structure at 830(30) keV observed with  $3.6\sigma$  significance on the in-beam data likely corresponds to the 822(1) keV peak of the isomer-decay data. It cannot correspond to a decay from the first or second excited states but from a state at least 822 keV higher in excitation energy than these two states.

Six out of the twenty four possible cascades satisfy the items (1), (2), and (3), but only four of them satisfy the item (5) in addition. Furthermore, the combination of items (4) and (5) favours the placement of the 822 keV transition on top of the 642 one, reducing the possible level schemes only to two, shown in Figure 7.21.

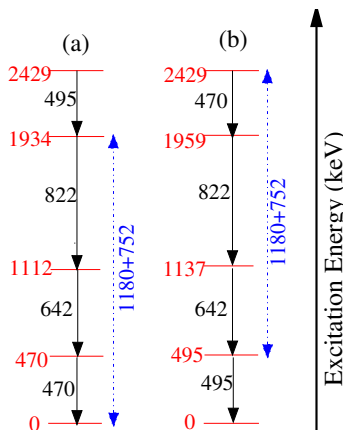


**Figure 7.21:** Possible level schemes of  $^{94}\text{Se}$  consistent with the combined in-beam and isomer decay results.

The peaks observed at 752 and 1180 keV are proposed to be transitions of  $^{94}\text{Se}$  given the fact that their relative intensities are similar, and their half-lives agree within error bars with the half-lives obtained for the isomeric transitions at 470, 495, 642, and 822 keV. Furthermore, the energy-sum relation  $470(1) + 822(1) + 642(1) = 1934(2)$  is within error bars equal to  $1932(2) \approx 752(1) + 1180(1)$ , so they could be placed as it is shown in Figure 7.21, revealing a second weakly populated cascade. Unfortunately, their singles intensities are not enough for a  $\gamma\gamma$ -coincidence analysis so they were not placed in the final level scheme.

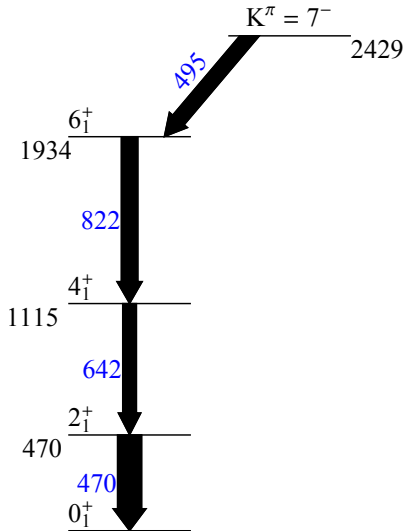


**Figure 7.22:** Level scheme proposed for  $^{94}\text{Se}$ . See text for details.

The level scheme proposed is shown in Figure 7.22. Recall that the 475(10) keV measured via in-beam spectroscopy is  $0.5\sigma$  and  $2\sigma$  away from the 470(1) and 495(1) keV obtained with decay spectroscopy, favouring option (a). For in-beam  $\gamma$ -ray spectroscopy it is known that the life-time of a decaying state shifts a transition photo-peak to a lower energy value [105], so it must be considered the possibility that the peak at 475(10) keV is in fact a shifted 495 keV. A lifetime shorter than 50 ps has been suggested for these states [24], which would lead to a shift  $\sim$  of 1.5% given the beam energies during the  $\gamma$ -ray emission ( $\sim 200$  MeV/nuc.), which corresponds to a detected energy of 487 keV, still more than  $1\sigma$  away from the reported value.

### Tentative spin-parity assignments

The  $2_1^+$  assignment is based on the systematics of the level schemes for the isotopic chain, and given the fact that it is the strongest peak detected via in-beam

spectroscopy. For the level at 1115 keV no transition was observed connecting to the ground state and the singles intensities of the 642 and 470 keV peaks agree within error bars, leading to a  $4_1^+$  assignment. For the state at 1934 keV, there is no  $\gamma$ -ray decaying to the  $2_1^+$  or ground state, ruling out possible  $J^\pi \leq 4^+$  and  $\leq 3^-$  assignments. Since there is an increasing energy gap between the states and the intensities are the same, a  $6_1^+$  assignment is suggested. For the state at 2429 keV an assignment  $J^\pi = 7^-$  is proposed, which will be discussed in Section 8.1.

---

## 8 Discussion

---

### 8.1 Origin of the isomeric states

---

#### $^{92}\text{Se}$ Isomeric state

Based on the experimental results presented in Section 7.2.5, the following assignments are proposed for the 67 keV transition:

$$8^- \rightarrow 6^-, \quad 9^- \rightarrow 7^-, \quad 9^+ \rightarrow 7^+, \quad 10^+ \rightarrow 8^+.$$

A seniority isomer is not likely in this region of the nuclide chart since there are no indications of shell closures in the closest even-even neighbouring nuclei. A spin-trap is also excluded, since there is no large spin difference between the states causing a long half-life. Instead, the single-particle character observed from the decay strength around 1 W.u., and the excitation energy of  $\sim 3$  MeV are consistent with the presence of a quasiparticle state (see Section 2.1.1). This hypothesis is further explored considering the Nilsson levels near the Fermi surface of this nucleus obtained from the different CHFB calculations, see Figures 3.2, 3.3 and 8.1. It has been identified a reduced set of levels there allowing the coupling of two quasi-neutrons into states with the large spins constrained for this transition. Namely,

$$K^\pi = 9^- = n \frac{11^-}{2}[505] \otimes \frac{7^+}{2}[404], \quad (120)$$

$$K^\pi = 7^- = n \frac{11^-}{2}[505] \otimes \frac{3^+}{2}[411], \quad (121)$$

both having moderate oblate deformations in the range  $\beta \sim (-0.28, -0.22)$ . On the prolate side, quasiparticle states with a spin of  $6^-$  can occur only for  $\beta \sim 0.47$ , which is rather large, and no combination yielding spin  $8^-$  can be formed. On the proton side, the highest spin combination is an oblate  $5^-$ , though in this case the energy gap to the first level above the Fermi surface is larger than for neutrons. These possible couplings lead to the conclusion that the most likely transition is the  $9^- \rightarrow 7^-$ , involving one of the  $K^\pi$  configurations above mentioned. The scattering of a coupled neutron from the  $\frac{7^+}{2}[404]$  to the  $\frac{3^+}{2}[411]$  orbital can be unfavoured in case of strongly coupled pairs due to the *blocking effect* [73, 106], that unfavours scattering of paired nucleons into single-occupied levels. At the same deformation, there is a possibility to form a  $9^-$  state with a four quasiparticle coupling at the orbitals  $\frac{11^-}{2}[505], \frac{7^+}{2}[404], \frac{3^+}{2}[411], \frac{3^+}{2}[402]$ , coupling the last two to zero. However, this option is just one of the possible couplings of these 4qp, since the final  $K^\pi$  can be any of between  $|K_1 \pm K_2 \pm K_3 \pm K_4|$ . A schematic picture of the quasiparticles discussed is shown in Figure 8.1.

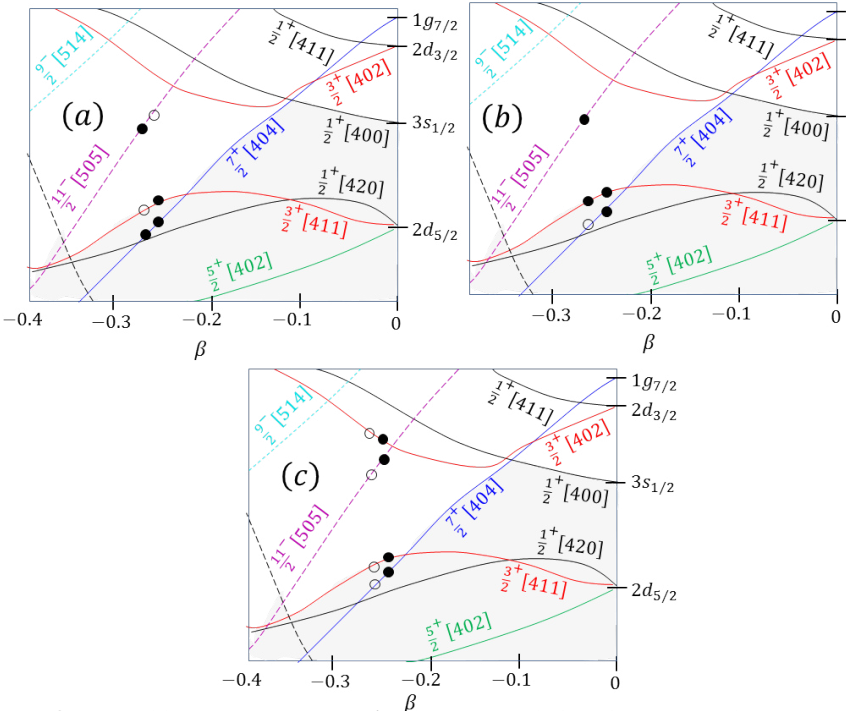


**Figure 8.1:** Possible quasi-neutron configurations coupled to the suggested spin-parity of the states involved in the isomeric decay of  $^{92}\text{Se}$ . The Nilsson levels shown are the same of Figure 3.2, expanded on the oblate side and near the Fermi surface, represented by the grey area. (a)  $K^\pi=7^-$ , from the two quasineutron  $n\frac{11}{2}^-[505] \otimes \frac{3}{2}^+[411]$  coupling. (b)  $K^\pi=9^-$ , from the two quasineutron  $n\frac{11}{2}^-[505] \otimes \frac{3}{2}^+[411]$  coupling. (c)  $K^\pi=9^-$ , from the four quasineutron coupling.

#### $^{94}\text{Se}$ Isomeric state

Considering the level scheme proposed, there are two possibilities for the  $\gamma$ -ray of the isomeric decay: it corresponds to a transition either stemming from or decaying into the 2429 keV level.

In case the isomeric transition decays into the 2429 keV then it was not detected. Therefore, its possible energy is constrained to a range where the EURICA detection efficiency is rather low so that the amount of  $\gamma$ -ray decays of such transition are below the *detection limit* of the setup. The number of decays of such hypothetical transition has to be -at least- similar to the singles intensities observed for the transitions of the yrast band, which is in average  $\sim 120$  counts (see Table 13). The efficiency at  $E_\gamma \sim 1500$  keV is such that  $\epsilon_{1500} \sim 0.75 \times \epsilon_{822}$ , so a new transition

would have been detected with  $\sim 90$  efficiency-corrected counts. For larger  $\gamma$ -ray energies the efficiency was not calibrated but it is clearly decreasing, so a reasonable detection limit can be proposed around  $\sim 2$  MeV. However, such option for the isomeric transition seems unlikely, not only because a state at  $\sim 4$  MeV would most likely have easier decay branches than a 2 MeV isomeric one, but also there are no counts in none of the  $\gamma\gamma$  coincident spectra after  $\sim 850$  keV (see Figure 7.15), indicating no coincidences between the yrast transitions with Compton-scattered hits of the hypothetical transition.

For  $E_\gamma \sim 50$  keV, the efficiency is higher than at 822-keV (see Figure 6.14), but the internal conversion reduces the amount of  $\gamma$ -decays considerably (see Figure 4.2) so that this is the lowest energy value where one can be sure that there is sensitivity enough to detect a potential transition. For instance, at  $E_\gamma \sim 40$  keV it happens that  $\epsilon_{40} \sim \epsilon_{822}$  but internal conversion becomes already very dominant over  $\gamma$ -ray decay by at least a factor of 10 (of course increasing strongly with the multipolar order), so a transition with an energy below this limit could have been missed. Furthermore, the threshold of the detectors was set between 25-30 keV to avoid excessive triggering of noise signals, so no transition below this limit could be detected.

The other possibility for the isomeric  $\gamma$ -ray corresponds to the 470 keV transition, stemming from the 2429 keV level and decaying mainly to the  $6_1^+$ . Since the current singles intensities are very similar and agree within error bars it is assumed that possible transitions from the 2429 keV level to the  $2_1^+$  or  $4_1^+$  are weak (given uncertainties in the intensities  $\sim 10\%$ , non-observed decay branches with weak branching ratios cannot be excluded. At 2429 keV a quasiparticle state is likely to occur, so the Nilsson diagrams are inspected to find if there are couplings that fit the decay pattern. Similarly to  $^{92}\text{Se}$ , the maximum coupling on the proton side is an oblate  $5^-$ , which would likely decay to the  $4_1^+$ . Furthermore, the energy gap of the closest level above the Fermi surface is larger for protons than neutrons, favouring the breaking of neutron pairs. On the neutron side, prolate deformations up to  $\beta \sim 0.4$  can only produce  $2^{+-}$ ,  $3^{+-}$ ,  $4^+$  but none of them are likely given the decay pattern. For oblate deformations, in the range  $\beta \sim (0, -0.2)$  the possible couplings are  $5^+$  or  $2^+$ , both disregarded since they favour a transition to the  $4_1^+$ . However, for  $\beta \sim (-0.3, -0.2)$  the configuration

$$K^\pi = 7^- = n \frac{11}{2}^- [505] \otimes \frac{3}{2}^+ [402], \quad (122)$$

is favoured, given the crossing of these two orbitals at around  $\beta \approx -0.25$ . This spin assignment indeed matches the decay pattern observed, since transitions to  $4_1^+$ ,  $2_1^+$  states are not favoured compared a transition to the  $6_1^+$ .

To understand why the  $7^- \rightarrow 6_1^+$   $E1$  decay would be in fact isomeric, recall the concepts of  $K$ -isomerism (see Section 4.3.4). If the decay had a single-particle

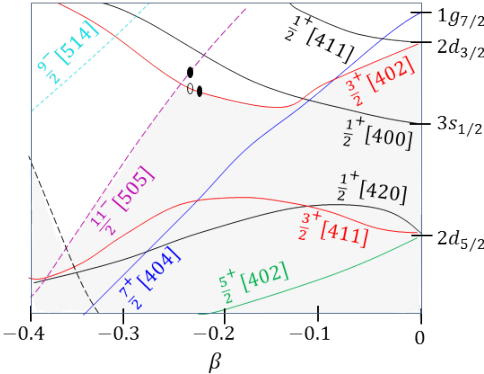


**Figure 8.2:** Possible  $K^\pi=7^-$  state involved in the isomeric decay of  $^{94}\text{Se}$ . It is formed as the two quasineutron coupling  $n\frac{11}{2}^-[505] \otimes \frac{3}{2}^+[402]$ . The grey area corresponds to the levels below (or at) the Fermi surface.

character (rather than collective) the experimental half-life is expected to have strengths typical of the observed ones for E1 transitions ( $B(\text{E1}) \approx 10^{-2}$  W.u.), leading to an estimate of  $T_{0.01\text{W.u.}}(\text{E1}) = 269.5$  fs. Nevertheless, the observed half-life of  $0.68(5)$   $\mu\text{s}$  indicates that the decay process is much slower. The *hindrance factor* ratio ( $\tau^\gamma/\tau^W$ ) leads to:

$$F_W = 0.68(5) \times 10^{-6} / 2.695 \times 10^{-15} \approx 2.52(18) \times 10^8 \gg 1. \quad (123)$$

Furthermore, the *K-forbiddenness* of the transition is  $\nu = \Delta K - \lambda = (7 - 0) - 1 = 6$ , which yields a *reduced hindrance* of

$$f_\nu = (F_W)^{1/\nu} = (2.52 \times 10^8)^{1/6} \approx 25.1(3). \quad (124)$$

A hindrance factor of  $F_W \gg 1$  and a reduced hindrance  $f_\nu \sim 10\text{-}300$  are in general indicators of *K*-forbidden decays [72, 73, 75]. The range of 10–300 is too broad though to be used as evidence of a specific type of *K*-hindrance, but more specific ranges have been identified for different values of forbiddenness. For instance, the  $\nu=6$  E1 transitions corresponding to the decay  $7^- \rightarrow 6^+$  known so far [76, 107], are mostly in the range of  $27 < f_\nu < 45$  regardless the nucleus mass. This interval is very close to the value obtained for  $^{94}\text{Se}$ , see Figure 8.3.

It is worth to recall that a *K*-hindered decay is a probe of the preservation in average of the axial deformation of both states involved in the transition, so that  $K^\pi$ , the projection on the symmetry axis, can be considered a good quantum number.

## 8.2 Comparison of excitation energies with BMF calculations

The BMF calculations considered here (Section 3.4) are of interest since they all consider a basis of states with quadrupolar deformations along the full triaxial map so they provide a more realistic description mean-field potential deformation in

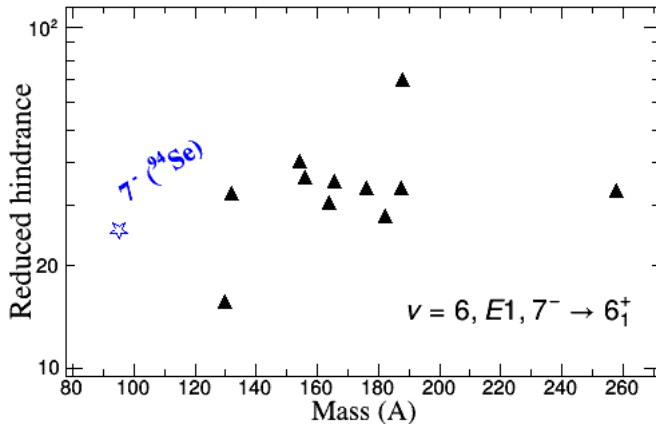


**Figure 8.3:**  $f_\nu$  for known  $\nu=6$ ,  $E1$  transitions from  $7^- \rightarrow 6^+$  isomers, compared to the proposed decay of  $^{94}\text{Se}$ . The highest value corresponds to  $^{186}\text{W}$ , the lowest to  $^{128}\text{Ba}$ , the highest mass to  $^{256}\text{Fm}$ .  $^{188,190,192}\text{Pt}$  cases are excluded. Source [76, 107].

comparison with calculations restricted to the basis of axially-symmetric shapes, more common in the past since they are much less computationally expensive. The prediction of the  $2_1^+$ ,  $2_2^+$ , and  $4_1^+$  excitation energies compared to the experimental values along the isotopic chain are shown in Figure 8.4.

In general, the CHFB+5DCH calculations show the better quantitative agreement with the experimental energies. Its predicted values overestimate systematically the excitation energies between 5-15%, and reproduce the energy-decreasing trends as a function of neutron number. At  $N=56$  the calculations predict a slightly increase of the excitation energies for the levels considered (suggesting a reminiscent sub-shell closure effect), however, this is not experimentally observed.

The CHFB+SCCM also predicts a systematics of decreasing excitation energies as a function of neutron number, and present good quantitative agreement between  $N=56-60$ . However, at  $N=52-54$  these calculations overestimate the experimental data in  $\sim 30\text{-}40\%$ . This effect is caused due to the absence of a *cranking* constraint on the angular momentum of the intrinsic basis-states used to describe a particular excited level [108] (see Equation 42). The implementation of the correction has proved to reach very good quantitative agreement with experimental spectra in a recent study of  $^{32}\text{Mg}$  [108]. However, this extension of the calculation method does not change considerably the Potential Energy Surfaces for the ground state (Figure 3.1) so that the shape evolution with neutron number predicted in the current calculations does not change.

The CHFB+IBM calculations reproduce the energy-decreasing systematics, and present good quantitative agreement for the yrast states at  $N=52$  and  $54$ , close

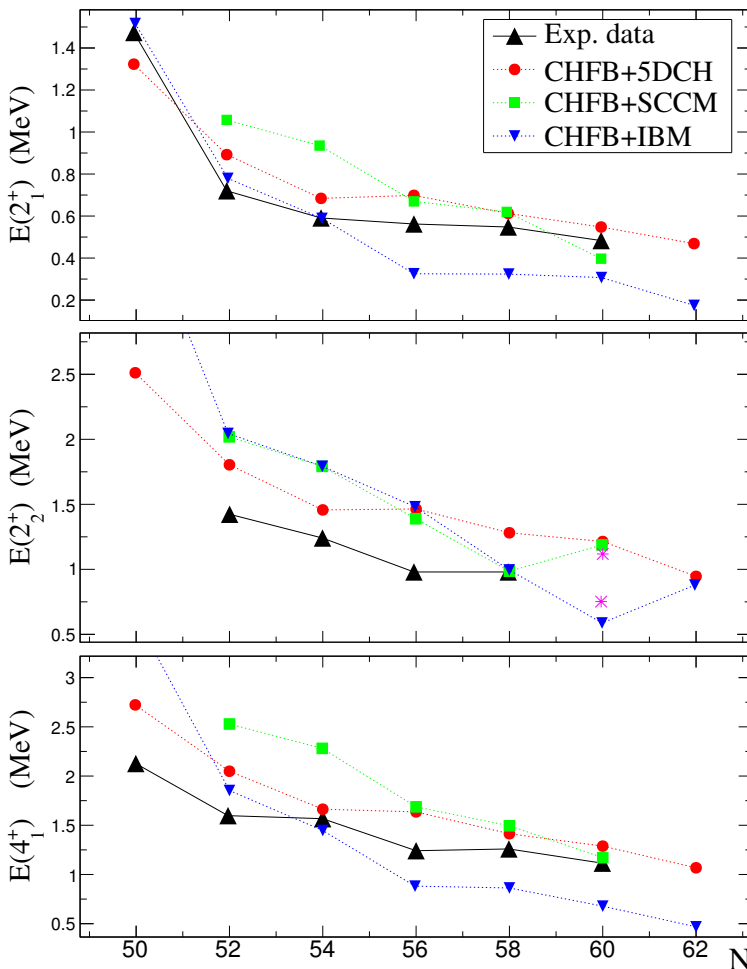


**Figure 8.4:** Excitation energies of lowest excited states for the Selenium isotopic chain between  $50 \leq N \leq 60$  compared to predictions of different state-of-the-art beyond mean field calculations.

to the shell closure. However, for  $N=56-60$ , the excitation energies are underestimated by  $\sim 50\%$ . In contrast, the prediction for the  $2_2^+$  overestimates the experimental value up to  $N=56$ , is the same at  $N=58$ , but continues decreasing up to  $N=60$  and does not stabilize after  $N=56$  like the experimental data. Moreover, for  $N=60$  it has a very different prediction compared to the 5DCH and SCCM methods: The excitation energy drops strongly, reaching a minimum along the isotopic chain.

Instead, the other two methods predict an increase in the energy to a value around 1200 keV.

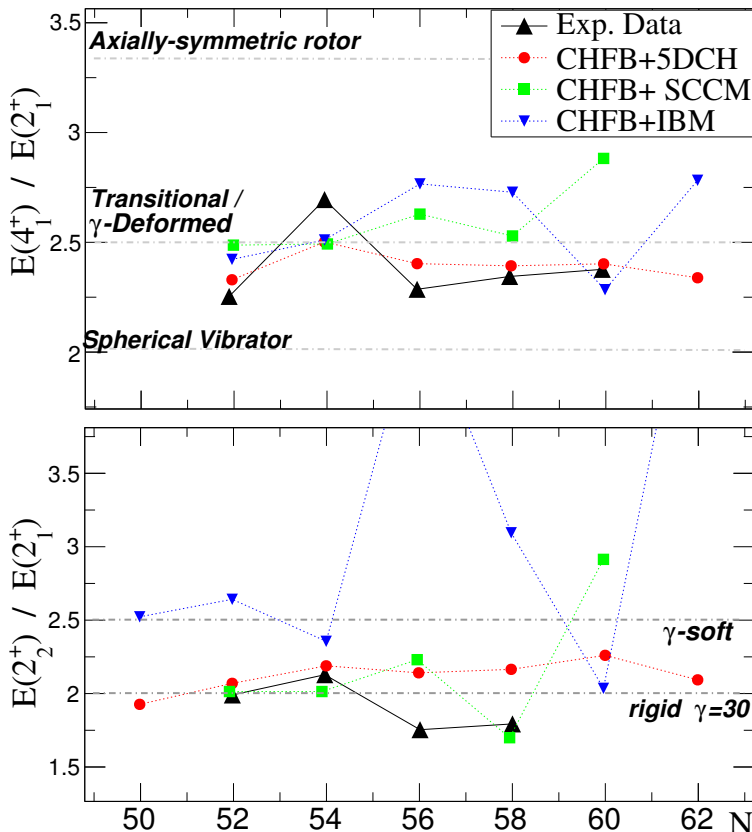


**Figure 8.5:**  $R_{4/2}$  and  $R_{2/2}$  ratios for neutron-rich Selenium isotopes between  $52 \leq N \leq 60$  compared to the calculations of the beyond mean-field methods considered in this work.

The comparison of the  $R_{4/2}$  and  $R_{2/2}$  ratios are shown in Figure 8.5. The different structural limits of quadrupolar deformations (Section 2.3.2) are highlighted. The experimental  $R_{4/2}$  values lie around 2.36, in the transitional /  $\gamma$ -deformed region. The 5DCH follows this trend closely, with a very flat behaviour. The SCCM values also remain in the same region, although they present higher values with an increasing trend between 2.5-2.7. The IBM values present fluctuations between 2.25-2.77 but remaining in the region as well.

Concerning the  $R_{2/2}$ , the experimental values are rather low with respect to the Wilets-Jean  $\gamma$ -soft limit. For  $N=52-54$  the experimental values resemble more the

rigid triaxial rotor having maximum degree of triaxiality, and are followed by the 5DCHM and SCCM calculations meanwhile the IBM values lie in a range of  $\gamma$ -soft behaviour / less pronounced triaxiality. At  $N=56$ - $58$  the experimental values are around  $\sim 1.77$ , below the minimum value possible for the rigid triaxial rotor, occurring at  $\gamma=30^\circ$ . In cases that oscillations are coupled to the rotations, lower values can be obtained in the Davydov model [55, 56], but in order to reproduce the experimental ratio it should occur that  $\gamma \geq 27.5^\circ$ , and the coupling to the vibrations is strong, see Ref. [109]. The BMF results have different trends at  $N=56$ - $58$ : A sharp increase-decrease (IBM), flat behaviour (5DCHM), and decreasing behaviour (SCCM). The SCCM has rather similar values than the experimental ratios except for  $N=56$  ( $^{90}\text{Se}$ ).

At  $N=60$  there is no experimental value for the  $2_2^+$  (and  $R_{2/2}$ ) yet. However it is noticed that a placement of the 752 keV transition on top of the 470 keV would lead to a possible  $E(2_2^+) = 1221$  keV, very close to the 1220 keV predicted by 5DCHM and SCCM.

### 8.3 Shape evolution around $N=58$

The previous comparisons reflect that non-axial deformations have a significant role in the low-excitation energy spectrum of the Selenium isotopes after the shell closure at  $N=50$ . Recently, the same influence has been observed for the neighbouring Ge and Kr nuclei [23, 26, 31]. However, the comparisons also put in evidence that the ideal non-axial models do not explain case by case all the features of each nucleus, specifically for  $N \geq 56$ , where the rather low  $2_2^+$  levels question their nature as  $\gamma$ -vibrations or as the band-head of a configuration with different intrinsic structure. Furthermore, the existence of  $0_2^+$  states below the  $2_2^+$  is predicted by the SCCM and IBM calculations but they have not been observed so far (they are also predicted in the 5DCH above, but not far, from the  $2_2^+$ ). For instance, in  $^{92}\text{Se}$  the intensity sum of the  $2_2^+ \rightarrow 2_1^+$  and  $2_2^+ \rightarrow 0_1^+$  transitions is equal to the intensity of the 637 keV transition feeding the  $2_2^+$  state (Table 10), disregarding the possibility of a strong  $2_2^+ \rightarrow 0_2^+$  decay and therefore of a  $0_2^+$  as potential band-head.

The existence of the quasiparticle isomers with oblate configurations provide a hint on the shape evolution at  $N=58$ - $60$ . To understand why, the level schemes for  $^{80-94}\text{Se}$  are shown in Figure 8.6. On top of them, the SCCM *collective wave functions* of the  $0_1^+$ ,  $2_1^+$ , and  $2_2^+$  states are shown. These triaxial plots represent in a colour scale the weight that each quadrupolar deformation has in the final state (red=0.15, blue=0.0, contour lines gap = 0.01).

The oblate deformed  $7^-$  state at  $N=58$  decays to the first-excited band instead of the ground-state band, opposite to the decay pattern of the  $7^-$  state at  $N=60$ , which decays to the  $6_1^+$  and not to any member of the first excited band that has

not been observed (or it presents a weak branching ratio, in case that the 752 and 1180 keV transitions correspond to that band).

The first question to clarify is whether the 503 keV transition in  $^{92}\text{Se}$  classifies as K-forbidden or not, like the 495 keV in  $^{94}\text{Se}$ . An estimation of the hindrance factor and forbiddenness yields  $F_W = 6.03 \times 10^4$ ,  $\nu = (7-2)-1=4$ , but the reduced hindrance is just  $f_\nu = 0.06$ , so the transition does not classify as K-forbidden since the decay to the  $K=2$  band is much less hindered.

A second question is why the isomer state at  $N=60$  decays to the yrast band instead of the first excited band. From the systematics of the level schemes along the isotopic chain (even at  $N=52$  which is not shown to keep simplicity) it is observed up to  $N=58$ , that the  $2_2^+$  states are always lower than the  $4_1^+$ , and the  $(3^+, 4_2^+)$  levels are  $\sim 30\%$  in energy above the  $4_1^+$ . Therefore, *if the excited band presents a similar behaviour at  $N=60$* , there must be an effect hindering the decay from the  $7^-$  to the potential  $(3^+, 4_2^+)$  level, which is in principle less forbidden due to the  $K=2$  value of the excited band. For instance, a hypothetical  $4_2^+$  placed likely between  $1429 \leq E_{4_2^+} \leq 1600$  would have an E3 decay branch with a Weisskopf half-life estimated in the range of  $1.5 \leq T_{1/2} \leq 5.8 \mu\text{s}$ , therefore being competitive to the  $E1$  observed decay with  $T_{1/2} = 0.68(5) \mu\text{s}$ . Looking at the collective wave functions, it can be seen that the deformation character of the ground and excited state bands in  $^{94}\text{Se}$  are predicted to be oblate and prolate, respectively. Therefore, the favouring of the decay to the ground state can be linked to a similarity between the structure of the isomer and ground state levels, but at the same time, a structural difference with respect to the excited band.

Another possibility that explains the decay pattern is that the excited band shifts high in energy so that the  $(3^+, 4_2^+)$  level lies close to the isomeric state or above, and only the  $2_2^+$  level would be lower than the  $K^\pi = 7^-$  so the decay is unfavoured given slow decay rate of a  $M5$  transition. Based on the good agreement between the BMF calculations and the experimental data, this option is not favoured. Even in that situation, it must be explained why the excitation energy of the band goes suddenly high in energy, which also hints to a structural change effect at  $N=60$ .

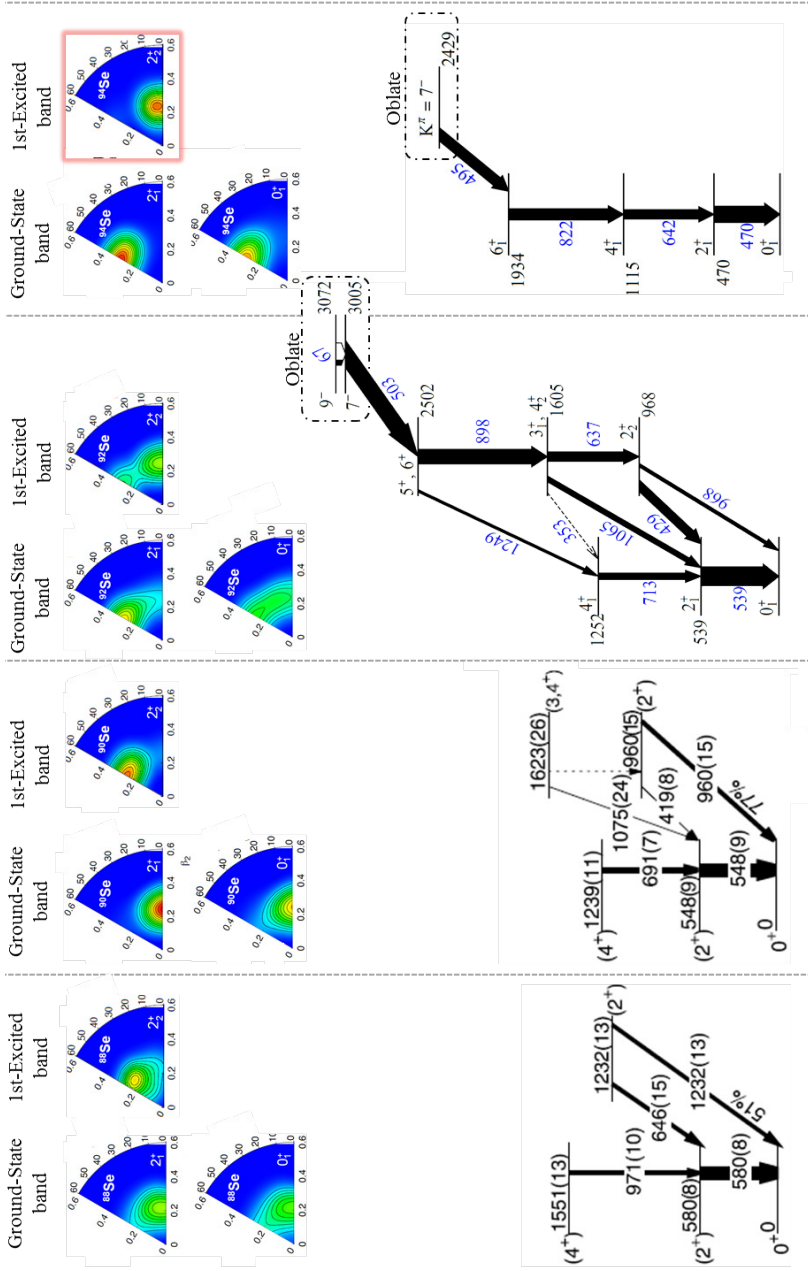


**Figure 8.6:** (Bottom) Low-lying level schemes for Selenium isotopes with  $N=54-60$ , including the results of this work and [24]. (Top) Collective wave functions for  $0_1^+$ ,  $2_1^+$  and  $2_2^+$  states obtained with the SPCM calculations [24, 110].

---

## 9 Conclusions and remarks

---

The study of the nuclear structure of exotic nuclei far from the stability is currently one of the most active fields in nuclear physics research due to the possibilities of exploring the evolution of the nuclear models in regions of the nuclear chart not accessible until the advent of Radioactive Ion Beams. In this thesis, the isomerism phenomena in the neutron-rich  $^{92,94}\text{Se}$  was studied by means of  $\gamma$ -ray spectroscopy, using the RIBF-RIKEN state-of-the-art facilities, and the EURICA HPGe detector. The analysis of the experimental data has allowed to extend the low-lying level scheme of these nuclei. The comparison of the results with the simplest models of non-axial deformation show that indeed the nuclei present features of axially-asymmetric quadrupolar deformation, but also put in evidence that the deformation is more complex than the represented in these models. The comparison with different Beyond-Mean-Field calculations has good agreement with the excitation spectra, though there are specific questions remaining not answered (such as the existence of low-lying  $0_2^+$  or the energy of the  $E(2_2^+)$  at  $N=60$ ). At the same time, the single particle character of the levels involved in the isomeric transitions is supported by potential couplings of quasiparticles obtained from single-particle levels obtained with the HFB calculations. In particular, the isomerism in  $^{92}\text{Se}$  corresponds to an E2 decay which is long-lived due to the small 67 keV gap between the states involved. The isomeric state of  $^{94}\text{Se}$ , observed for the first time in this work, corresponds to a  $K$ -hindered decay of an oblate state. The comparison between the decay patterns of isomeric decay at  $N=58$  and  $N=60$  with the low-lying level scheme of the neighbouring isotopes between  $N=52-58$ , as well as with the predictions of the BMF methods, leads to the conclusion that the observations are in agreement with a shape transition to an oblate ground-state deformation at  $N=60$ .

---

## A Error propagation of relevant quantities

---

In order to discuss the error propagation in some quantities of interest in this thesis, lets considered the error propagation of the following to cases:

**A.** The error of the quantity  $u = v/w$ , defined as the ratio of the two independent measurements  $v$  and  $w$ :

$$\begin{aligned}\Delta u &= \sqrt{\left(\frac{\partial u}{\partial v}\right)^2 \cdot (\Delta v)^2 + \left(\frac{\partial u}{\partial w}\right)^2 \cdot (\Delta w)^2} \\ &= \sqrt{\left(\frac{1}{w}\right)^2 \cdot (\Delta v)^2 + \left(\frac{-v}{w^2}\right)^2 \cdot (\Delta w)^2} \\ &= \sqrt{\left(\frac{v}{w}\right)^2 \cdot \left(\frac{\Delta v}{v}\right)^2 + \left(\frac{v}{w}\right)^2 \cdot \left(\frac{\Delta w}{w}\right)^2} \\ &= \left(\frac{v}{w}\right) \sqrt{\left(\frac{\Delta v}{v}\right)^2 + \left(\frac{\Delta w}{w}\right)^2} \\ &= u \cdot \sqrt{\left(\frac{\Delta v}{v}\right)^2 + \left(\frac{\Delta w}{w}\right)^2}.\end{aligned}\tag{125}$$

**B.** The error of the quantity  $u = v \pm w$ , defined as the sum/subtraction of the two independent measurements  $v$  and  $w$ :

$$\begin{aligned}\Delta u &= \sqrt{\left(\frac{\partial u}{\partial v}\right)^2 \cdot (\Delta v)^2 + \left(\frac{\partial u}{\partial w}\right)^2 \cdot (\Delta w)^2} \\ &= \sqrt{(1)^2 \cdot (\Delta v)^2 + (\pm 1)^2 \cdot (\Delta w)^2} \\ &= \sqrt{(\Delta v)^2 + (\Delta w)^2}\end{aligned}$$

**C.** When the quantity  $u = f(v, w)$ , depends of two measurements  $v$  and  $w$  not completely independent from each other:

$$\Delta u^2 = \left(\frac{\partial f}{\partial v}\right)^2 \cdot (\Delta v)^2 + \left(\frac{\partial f}{\partial w}\right)^2 \cdot (\Delta w)^2 + \frac{\partial f}{\partial v} \frac{\partial f}{\partial w} \Delta(u, v)$$

with  $\Delta(u, v)$  the correlation between the two measurements.

## A.1 Error of singles intensities

The singles intensities are important to evaluate the consistency of the level scheme observed in the isomeric decay. As it was explained in Section 7.2.4, the efficiency corrected intensities were estimated after a background subtraction of the ‘preliminary singles spectrum’. As an example, the spectra relevant for the singles intensities estimation are shown in Figure A.1, centred around the 713 keV transition of  $^{92}\text{Se}$ . The bin error of the background ( $h_{\text{bck}}$ ) and preliminary singles ( $h_a$ ) spectra is given by  $\sqrt{N}$ , with  $N$  the number of counts of each bin. The bin error of the background subtracted spectrum ( $h_{\text{subt}}$ ) is given by  $\sqrt{N_{\text{bck}} + N_a}$ , since the bin content corresponds to the subtraction  $N_{\text{subt}} = N_{\text{bck}} - N_a$ .

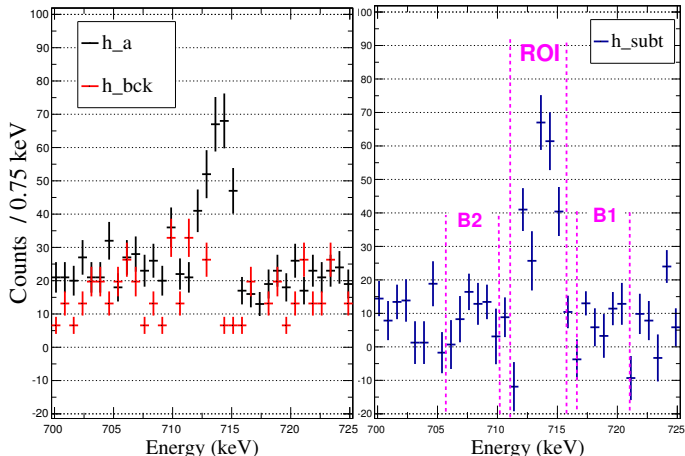


**Figure A.1:** Energy spectra involved in the singles intensities estimation, centred around the 713 keV transition of  $^{92}\text{Se}$ . See text for details.

The singles intensity of the transition with energy  $E_\gamma$  corresponds to the peak area of the background-subtracted spectrum, estimated as the integral of the counts in the region of interest (ROI) minus the average (remaining) background determined (and properly normalized) from energy intervals next to the photopeak. In simple terms:

$$\begin{aligned}
 i(E_\gamma) &= \sum_{k \in ROI} N_k - \frac{\Delta E_{ROI}}{\Delta E_{B2} + \Delta E_{B1}} \times \left( \sum_{j \in B1} N_j + \sum_{j \in B2} N_j \right) \\
 i(E_\gamma) &= N_p - R \times N_b,
 \end{aligned} \tag{126}$$

with the quantities  $N_p$ ,  $N_b$ ,  $R$ , and the corresponding uncertainties given by

$$\begin{aligned} R &= \frac{\Delta E_{ROI}}{\Delta E_{B2} + \Delta E_{B1}}, \\ N_p &= \sum_{k \in ROI} N_k \Rightarrow \Delta N_p = \sqrt{N_p^{bck} + N_p^a}, \\ N_b &= \sum_{j \in B1, B2} N_j \Rightarrow \Delta N_b = \sqrt{N_b^{bck} + N_b^a}. \end{aligned}$$

To obtain efficiency-corrected intensity, it is sufficient to divide by the EURICA efficiency:

$$I(E_\gamma) = i(E_\gamma)/\epsilon(E_\gamma), \quad (127)$$

and its uncertainty is given by:

$$\Delta I(E_\gamma) = I(E_\gamma) \sqrt{\left( \frac{\Delta i(E_\gamma)}{i(E_\gamma)} \right)^2 + \left( \frac{\Delta \epsilon(E_\gamma)}{\epsilon(E_\gamma)} \right)^2},$$

with

$$\Delta i(E_\gamma) = \sqrt{(\Delta N_p)^2 + R^2(\Delta N_b)^2}. \quad (128)$$

The efficiency uncertainty  $\Delta \epsilon(E_\gamma)$  was not considered in the error estimation since it is a variable highly dependent of the energy. For instance, at lower energies ( $\lesssim 100\text{keV}$ ) the  $\gamma$ -rays can be absorbed in AIDA leading to a larger uncertainty in the EURICA detection efficiency compared to higher energy values ( $\gtrsim 300\text{keV}$ ) that are less susceptible to be absorbed before reaching the Ge crystals.

## A.2 Error of relative intensities

The relative intensity of a transition with energy  $E_\gamma$  was defined as the ratio  $I_{rel}(E_\gamma) = I(E_\gamma)/I(E_0)$ , with  $I(E_\gamma)$  and  $I(E_0)$  the absolute singles intensities, and  $E_0$  the energy of the strongest transition observed, 539 and 470 keV for  $^{92,94}\text{Se}$ , respectively. Therefore, its error was computed as

$$\Delta I_{rel}(E_\gamma) = I_{rel}(E_\gamma) \sqrt{\left( \frac{\Delta I_\gamma}{I_\gamma} \right)^2 + \left( \frac{\Delta I_0}{I_0} \right)^2}, \quad (129)$$

with  $\Delta I_\gamma$  and  $\Delta I_0$  the error of the absolute singles intensities discussed in Section A.1.

## B Results of in-beam spectroscopy of $^{92,94}\text{Se}$ - SEASTAR 2015

The results of the in-beam spectroscopy measurements of  $^{92,94}\text{Se}$  conducted with the DALI2 array during the SEASTAR 2015 Campaign have been published in Ref. [24], and are shown in Figure B.1. The Doppler corrected energy spectra in coincidence with  $^{92,94}\text{Se}$  are shown. Each spectrum was obtained from a single reaction channel: (c)  $^{94}\text{Br}(p; 2pn)^{92}\text{Se}$ , (d)  $^{95}\text{Br}(p; 2p)^{94}\text{Se}$ . The spectra were fitted with simulated response functions (red) added on top of a two-exponential background (black). In the insets, examples of the  $\gamma\gamma$ -coincidence analysis and deduced level schemes are presented, the widths of the arrows reflect relative intensities of transitions, dashed lines are used for very weak transitions.

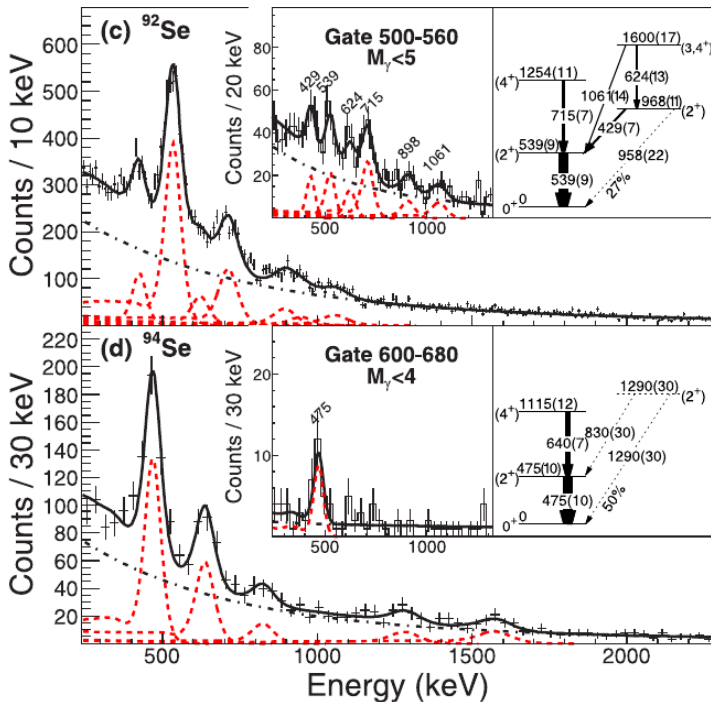


**Figure B.1:** Results of in-beam spectroscopy of  $^{92,94}\text{Se}$  obtained in the SEASTAR 2015 Campaign. Source: [24].

---

## Bibliography

---

- [1] K. S. Krane. *Introductory Nuclear Physics*. John Wiley & Sons, 1988.
- [2] <http://padakshep.org/otp/subjects/chemistry/physical-chemistry/discovery-of-electrons-protons-and-neutrons/>. Website.
- [3] -. *Nuclear Physics for Medicine*. Brochure. 2014.
- [4] <http://www.nndc.bnl.gov/chart/>. Official Website.
- [5] J. Erler et al. *The limits of the Nuclear Landscape*. In: *Nature* 486 (2012), pp. 509–512.
- [6] -. *Semi-empirical mass formula*. From Wikipedia, the free encyclopedia. -.
- [7] <http://people.physics.anu.edu.au/~ecs103/chart/>. Official Website.
- [8] E. Caurier et al. *The shell model as a unified view of nuclear structure*. In: *Rev. Mod. Phys.* 77 (2 June 2005), pp. 427–488. DOI: [10.1103/RevModPhys.77.427](https://doi.org/10.1103/RevModPhys.77.427).
- [9] Maria Goeppert Mayer. *Nuclear Configurations in the Spin-Orbit Coupling Model. I. Empirical Evidence*. In: *Phys. Rev.* 78 (1 Apr. 1950), pp. 16–21. DOI: [10.1103/PhysRev.78.16](https://doi.org/10.1103/PhysRev.78.16).
- [10] Otto Haxel, J. Hans D. Jensen and Hans E. Suess. *On the "Magic Numbers" in Nuclear Structure*. In: *Phys. Rev.* 75 (11 June 1949), pp. 1766–1766. DOI: [10.1103/PhysRev.75.1766.2](https://doi.org/10.1103/PhysRev.75.1766.2).
- [11] Richard F Casten. *Nuclear Structure from a Simple Perspective. Second Edition*. Oxford University Press, 2000.
- [12] S. G. Nilsson. *Binding states of individual nucleons in strong deformed nuclei*. In: *Mat. Fys. Medd. Dan. Vid. Selsk.* 29 (16 1955).
- [13] Takaharu Otsuka. *Exotic nuclei and nuclear forces*. In: *Physica Scripta* T152 (2013), p. 014007.
- [14] D. Steppenbeck et al. *Evidence for a new nuclear /'magic number/' from the level structure of  $^{54}\text{Ca}$* . In: *Nature* 502 (2013/10/10), pp. 207–210.
- [15] Z.Y. Xu. *Beta-decay spectroscopy on neutron-rich nuclei in a range of  $Z = 26 – 32$* . PhD thesis. University of Tokyo, 2014.
- [16] Magdalena Kowalska. *Mg isotopes and the disappearance of magic  $N=20$* . In: *Hyperfine Interactions* 171.1 (1st July 2006), pp. 167–172. ISSN: 1572-9540. DOI: [10.1007/s10751-007-9512-9](https://doi.org/10.1007/s10751-007-9512-9).
- [17] Y. Blumenfeld, T. Nilsson and P. Van Duppen. *Facilities and Methods for radioactive ion beam production*. In: *Physica Scripta* T152 (2013), p. 014023.

---

---

- [18] <https://www.phy.anl.gov/gammasphere/>. Website.
- [19] [http://web-docs.gsi.de/~gsgweb/proj/rising\\_project.html](http://web-docs.gsi.de/~gsgweb/proj/rising_project.html). Website.
- [20] M. Riley and J. Simpson. *Nuclear Gamma Spectroscopy and the Gamma Spheres*. In: *Encyclopedia of Nuclear Physics and its Applications*. Ed. by Reinhard Stock. John Wiley & Sons, 2013. Chap. 7.
- [21] Doornenbal, P. and Obertelli, A. *Shell evolution and search for two-plus states at the RIBF (SEASTAR)*. In: *RIKEN proposal for scientific program* (2013), unpublished.
- [22] <http://www.nishina.riken.jp/RIBF/>. Official Website.
- [23] M. Lettmann et al. *Triaxiality of neutron-rich  $^{84,86,88}\text{Ge}$  from low-energy nuclear spectra*. In: *Phys. Rev. C* 96 (1 July 2017), p. 011301. doi: [10.1103/PhysRevC.96.011301](https://doi.org/10.1103/PhysRevC.96.011301).
- [24] S. Chen et al. *Low-lying structure and shape evolution in neutron-rich Se isotopes*. In: *Phys. Rev. C* 95 (4 Apr. 2017), p. 041302. doi: [10.1103/PhysRevC.95.041302](https://doi.org/10.1103/PhysRevC.95.041302).
- [25] N. Paul et al. *Are There Signatures of Harmonic Oscillator Shells Far from Stability? First Spectroscopy of  $^{110}\text{Zr}$* . In: *Phys. Rev. Lett.* 118 (3 Jan. 2017), p. 032501. doi: [10.1103/PhysRevLett.118.032501](https://doi.org/10.1103/PhysRevLett.118.032501).
- [26] F. Flavigny et al. *Shape Evolution in Neutron-Rich Krypton Isotopes Beyond  $N = 60$ : First Spectroscopy of  $^{98,100}\text{Kr}$* . In: *Phys. Rev. Lett.* 118 (24 June 2017), p. 242501. doi: [10.1103/PhysRevLett.118.242501](https://doi.org/10.1103/PhysRevLett.118.242501).
- [27] W. Witt and et al. publication in preparation.
- [28] A. Gade et al. *Collectivity at  $N = 50$ :  $^{82}\text{Ge}$  and  $^{84}\text{Se}$* . In: *Phys. Rev. C* 81 (6 June 2010), p. 064326. doi: [10.1103/PhysRevC.81.064326](https://doi.org/10.1103/PhysRevC.81.064326).
- [29] Y Shiga and et al. *Investigating nuclear shell structure in the vicinity of  $^{78}\text{Zn}$ : Low-lying excited states in the neutron-rich isotopes  $^{80,82}\text{Zn}$* . In: *Phys. Rev. C* 93 (2016), p. 024320.
- [30] Kris Heyde and John L. Wood. *Shape coexistence in atomic nuclei*. In: *Rev. Mod. Phys.* 83 (4 Nov. 2011), pp. 1467–1521. doi: [10.1103/RevModPhys.83.1467](https://doi.org/10.1103/RevModPhys.83.1467).
- [31] Tomás R. Rodríguez. *Structure of krypton isotopes calculated with symmetry-conserving configuration-mixing methods*. In: *Phys. Rev. C* 90 (3 Sept. 2014), p. 034306. doi: [10.1103/PhysRevC.90.034306](https://doi.org/10.1103/PhysRevC.90.034306).
- [32] C. Kremer et al. *First Measurement of Collectivity of Coexisting Shapes Based on Type II Shell Evolution: The Case of  $^{96}\text{Zr}$* . In: *Phys. Rev. Lett.* 117 (17 Oct. 2016), p. 172503. doi: [10.1103/PhysRevLett.117.172503](https://doi.org/10.1103/PhysRevLett.117.172503).

[33] Tomoaki Togashi et al. *Quantum Phase Transition in the Shape of Zr isotopes*. In: *Phys. Rev. Lett.* 117 (2016), p. 172502.

[34] Takaharu Otsuka et al. *Novel Features of Nuclear Forces and Shell Evolution in Exotic Nuclei*. In: *Phys. Rev. Lett.* 104 (1 Jan. 2010), p. 012501. doi: [10.1103/PhysRevLett.104.012501](https://doi.org/10.1103/PhysRevLett.104.012501).

[35] J. Litzinger et al. *Transition probabilities in neutron-rich  $^{84,86}\text{Se}$* . In: *Phys. Rev. C* 92 (6 Dec. 2015), p. 064322. doi: [10.1103/PhysRevC.92.064322](https://doi.org/10.1103/PhysRevC.92.064322).

[36] T. Materna et al. *Low spin structure of  $^{86}\text{Se}$ : Confirmation of  $\gamma$  collectivity at  $N = 52$* . In: *Phys. Rev. C* 92 (3 Sept. 2015), p. 034305. doi: [10.1103/PhysRevC.92.034305](https://doi.org/10.1103/PhysRevC.92.034305).

[37] J. Dudouet et al.  $^{96}_{36}\text{Kr}_{60}$ . In: *Phys. Rev. Lett.* 118 (16 Apr. 2017), p. 162501. doi: [10.1103/PhysRevLett.118.162501](https://doi.org/10.1103/PhysRevLett.118.162501).

[38] J. -P Delaroche et al. *Structure of even-even nuclei using a mapped collective Hamiltonian and the D1S Gogny interaction*. In: *Phys. Rev. C* 81 (1 Jan. 2010), p. 014303. doi: [10.1103/PhysRevC.81.014303](https://doi.org/10.1103/PhysRevC.81.014303).

[39] P. Sarriuguren.  *$\beta$ -decay properties of neutron-rich Ge, Se, Kr, Sr, Ru, and Pd isotopes from deformed quasiparticle random-phase approximation*. In: *Phys. Rev. C* 91 (4 Apr. 2015), p. 044304. doi: [10.1103/PhysRevC.91.044304](https://doi.org/10.1103/PhysRevC.91.044304).

[40] LIU Ying, Xu Fu-rong and Zhong-bin CAO. *Shape Coexistence in Selenium Isotopes*. In: *Nuclear Physics Review - China* 27.2, 146 (2010), p. 146.

[41] K. Nomura, R. Rodríguez-Guzmán and L. M. Robledo. *Structural evolution in germanium and selenium nuclei within the mapped interacting boson model based on the Gogny energy density functional*. In: *Phys. Rev. C* 95 (6 June 2017), p. 064310. doi: [10.1103/PhysRevC.95.064310](https://doi.org/10.1103/PhysRevC.95.064310).

[42] A. Obertelli et al. *Shape evolution in self-conjugate nuclei, and the transitional nucleus  $^{68}\text{Se}$* . In: *Phys. Rev. C* 80 (3 Sept. 2009), p. 031304. doi: [10.1103/PhysRevC.80.031304](https://doi.org/10.1103/PhysRevC.80.031304).

[43] S. M. Fischer et al. *Evidence for Collective Oblate Rotation in  $N = Z = 68\text{Se}$* . In: *Phys. Rev. Lett.* 84 (18 May 2000), pp. 4064–4067. doi: [10.1103/PhysRevLett.84.4064](https://doi.org/10.1103/PhysRevLett.84.4064).

[44] A. M. Hurst et al. *Measurement of the Sign of the Spectroscopic Quadrupole Moment for the  $2^+_1$  State in  $^{70}\text{Se}$ : No Evidence for Oblate Shape*. In: *Phys. Rev. Lett.* 98 (7 Feb. 2007), p. 072501. doi: [10.1103/PhysRevLett.98.072501](https://doi.org/10.1103/PhysRevLett.98.072501).

[45] E. A. McCutchan et al. *Shape coexistence in  $^{72}\text{Se}$  investigated following the  $\beta$  decay of  $^{72}\text{Br}$* . In: *Phys. Rev. C* 83 (2 Feb. 2011), p. 024310. doi: [10.1103/PhysRevC.83.024310](https://doi.org/10.1103/PhysRevC.83.024310).

---

[46] S. Bacca. *Structure models: From shell model to ab initio methods*. In: *The European Physical Journal Plus* 131 (2016), p. 107.

[47] Walter Greiner. *Nuclear Models*. Springer, 2003.

[48] Denis Savran. <https://indico.gsi.de/event/1117/contribution/4/material/slides/0.pdf>

[49] D. Bohle et al. *New magnetic dipole excitation mode studied in the heavy deformed nucleus  $^{156}\text{Gd}$  by inelastic electron scattering*. In: *Physics Letters B* 137.1 (1984), pp. 27–31. ISSN: 0370-2693. DOI: [https://doi.org/10.1016/0370-2693\(84\)91099-2](https://doi.org/10.1016/0370-2693(84)91099-2).

[50] N. Pietralla et al. *Transition Rates between Mixed Symmetry States: First Measurement in  $^{94}\text{Mo}$* . In: *Phys. Rev. Lett.* 83 (7 Aug. 1999), pp. 1303–1306. DOI: [10.1103/PhysRevLett.83.1303](https://doi.org/10.1103/PhysRevLett.83.1303).

[51] L. P. Gaffney et al. *Studies of pear-shaped nuclei using accelerated radioactive beams*. In: *Nature* 497 (2013/05/09/print 2013), p. 199. DOI: [10.1038/nature12073](https://doi.org/10.1038/nature12073).

[52] Kenichi Matsuyanagi et al. *Microscopic derivation of the Bohr-Mottelson collective Hamiltonian and its application to quadrupole shape dynamics*. In: *Physica Scripta* 91.6 (2016), p. 063014.

[53] [https://www.nobelprize.org/nobel\\_prizes/physics/laureates/1975/bohr-lecture.pdf](https://www.nobelprize.org/nobel_prizes/physics/laureates/1975/bohr-lecture.pdf). Official Website.

[54] A. Bohr and B. Mottelson. *Nuclear Structure*. World Scientific, 1998.

[55] A.S. Davydov and G.F. Filippov. *Rotational states in even atomic nuclei*. In: *Nuclear Physics* 8 (1958), pp. 237–249.

[56] A.S. Davydov and V.S. Rostovsky. *Relative transition probabilities between rotational levels of non-axial nuclei*. In: *Nuclear Physics* 12 (1959), pp. 58–68.

[57] N.V. Zamfir and R.F. Casten. *Signatures of  $\gamma$  softness or triaxiality in low energy nuclear spectra*. In: *Physics Letters B* 260 N 3-4 (1991), pp. 265–270.

[58] L. Wilets and M. Jean. *Surface Oscillations in even-even nuclei*. In: *Physical Review* 102 N3 (1955), pp. 788–796.

[59] David Rowe. *Nuclear Collective Motion*. World Scientific, 2008.

[60] Zena Patel. *K Isomerism and Collectivity in Neutron-Rich Rare-Earth Isotopes*. PhD thesis. University of Surrey, 2015.

[61] J Luis Egido. *State-of-the-art of beyond mean field theories with nuclear density functionals*. In: *Physica Scripta* 91.7 (2016), p. 073003.

[62] J. Libert, M. Girod and J.-P. Delaroche. *Microscopic descriptions of superdeformed bands with the Gogny force: Configuration mixing calculations in the  $A \sim 190$  mass region*. In: *Phys. Rev. C* 60 (5 Sept. 1999), p. 054301. doi: [10.1103/PhysRevC.60.054301](https://doi.org/10.1103/PhysRevC.60.054301).

[63] J. Dechargé and D. Gogny. *Hartree-Fock-Bogolyubov calculations with the D1 effective interaction on spherical nuclei*. In: *Phys. Rev. C* 21 (4 Apr. 1980), pp. 1568–1593. doi: [10.1103/PhysRevC.21.1568](https://doi.org/10.1103/PhysRevC.21.1568).

[64] Rosh Sellahewa. *Isovector and Pairing properties of the Gogny force in the context of neutron stars*. PhD thesis. University of Surrey, United Kingdom, 2015.

[65] J.J Griffin and J.A. Wheeler. *Collective Motions in Nuclei by the Method of Generator Coordinates*. In: *Physical Review* 108 N2 (1957), pp. 311–327.

[66] M. Girod et al. *The role of triaxiality for the coexistence and evolution of shapes in light krypton isotopes*. In: *Physics Letters B* 676.1–3 (2009), pp. 39–43. ISSN: 0370-2693. doi: <http://doi.org/10.1016/j.physletb.2009.04.077>.

[67] [http://www-phynu.cea.fr/science\\_en\\_ligne/carte\\_potentiels\\_microscopiques/noyaux/zz34/niveaux/zz34nn56niveaux\\_eng.html](http://www-phynu.cea.fr/science_en_ligne/carte_potentiels_microscopiques/noyaux/zz34/niveaux/zz34nn56niveaux_eng.html). Website.

[68] D. Pelte and D. Schwalm. *In-beam gamma-ray spectroscopy with heavy ions*. Ed. by R. Bock. North-holland publishing company, 1982.

[69] T. Kibédi et al. *Evaluation of theoretical conversion coefficients using BrIcc*. In: *Nuclear Instruments and Methods in Physics Research Section A: Accelerators, Spectrometers, Detectors and Associated Equipment* 589.2 (2008), pp. 202–229. ISSN: 0168-9002. doi: <https://doi.org/10.1016/j.nima.2008.02.051>.

[70] G D Dracoulis. *Isomers, nuclear structure and spectroscopy*. In: *Physica Scripta* 2013.T152 (2013), p. 014015.

[71] G D Dracoulis, P M Walker and F G Kondev. *Review of metastable states in heavy nuclei*. In: *Reports on Progress in Physics* 79.7 (2016), p. 076301.

[72] P.M. Walker and G. Dracoulis. *Energy traps in atomic nuclei*. In: *Nature* 399 (1999), pp. 35–40. ISSN: 6731.

[73] P M Walker and F R Xu. *High-  $K$  isomerism in rotational nuclei*. In: *Physica Scripta* 91.1 (2016), p. 013010.

[74] *Seniority isomers in nuclei*. Vol. 322. *Journal of Physics: Conference Series* - page 012003. IOP Publishing, 2011.

---

[75] G D Dracoulis. *High- K states as a probe of nuclear structure*. In: *Physica Scripta* 2000.T88 (2000), p. 54.

[76] F.G. Kondev, G.D. Dracoulis and T. Kibédi. *Configurations and hindered decays of isomers in deformed nuclei with*. In: *Atomic Data and Nuclear Data Tables* 103–104 (2015), pp. 50–105. ISSN: 0092-640X. DOI: <https://doi.org/10.1016/j.adt.2015.01.001>.

[77] G.F. Knoll. *Radiation Detection and Measurement*. John Wiley and Sons, 2010.

[78] C.L. Davisson. *Interaction of gamma radiation with matter*. I. North-Holland Publishing Company, 1965.

[79] R.D Evans. *The atomic nucleus*. McGraw-Hill Book Company, 1955.

[80] Toshiyuki Kubo et al. *BigRIPS separator and ZeroDegree spectrometer at RIKEN RI Beam Factory*. In: *Prog. Theor. Exp. Phys.* (2012), p. 03C003.

[81] N. Fukuda et al. *Identification and separation of radioactive isotope beams by the BigRIPS separator at the RIKEN RI Beam Factory*. In: *Nucl. Instrum. Methods Phys. Res. B* 317 (2013), pp. 323–332.

[82] S. Takeuchi et al. *DALI2: A NaI(Tl) detector array for measurements of  $\gamma$ -rays from fast nuclei*. In: *Nucl. Instrum. Methods Phys. Res. A* 763 (2014), pp. 596–603.

[83] <http://www2.ph.ed.ac.uk/~td/DSSD/>. Official Website.

[84] P.-A. Söderström et al. *Installation and commissioning of EURICA - Euroball-RIKEN Cluster Array*. In: *Nuclear Instruments and Methods in Physics Research B* 317 (Dec. 2013), pp. 649–652. DOI: [10.1016/j.nimb.2013.03.018](https://doi.org/10.1016/j.nimb.2013.03.018).

[85] [http://www.nishina.riken.jp/facility/RILAC\\_e.html](http://www.nishina.riken.jp/facility/RILAC_e.html). Official Website.

[86] [http://www.nishina.riken.jp/facility/SRC\\_e.html](http://www.nishina.riken.jp/facility/SRC_e.html). Official Website.

[87] D.J. Morrisey and B.M. Sherril. *In-flight Separation of Projectile Fragments*. In: I. The Euroschool Lectures on Physics with exotic Beams. Springer, 2004.

[88] Toshiyuki Kubo. *In-flight RI beam separator BigRIPS at RIKEN and elsewhere in Japan*. In: *Nuclear Instruments and Methods in Physics Research Section B: Beam Interactions with Materials and Atoms* 204 (2003). 14th International Conference on Electromagnetic Isotope Separators and Techniques Related to their Applications, pp. 97–113. ISSN: 0168-583X. DOI: [http://dx.doi.org/10.1016/S0168-583X\(02\)01896-7](http://dx.doi.org/10.1016/S0168-583X(02)01896-7).

[89] T. Motobayashi. *RIKEN RI Beam Factory – Recent Results and Perspectives*. In: *Nuclear Physics A* 834.1 (2010). The 10th International Conference on Nucleus-Nucleus Collisions (NN2009), pp. 707c–712c. ISSN: 0375-9474. doi: <http://dx.doi.org/10.1016/j.nuclphysa.2010.01.128>.

[90] K.-H. Schmidt et al. *The momentum-loss achromat — A new method for the isotopical separation of relativistic heavy ions*. In: *Nuclear Instruments and Methods in Physics Research Section A: Accelerators, Spectrometers, Detectors and Associated Equipment* 260.2 (1987), pp. 287–303. ISSN: 0168-9002. doi: [http://dx.doi.org/10.1016/0168-9002\(87\)90092-1](http://dx.doi.org/10.1016/0168-9002(87)90092-1).

[91] H. Kumagai et al. *Development of Parallel Plate Avalanche Counter (PPAC) for BigRIPS fragment separator*. In: *Nuclear Instruments and Methods in Physics Research Section B: Beam Interactions with Materials and Atoms* 317 (2013). XVIth International Conference on ElectroMagnetic Isotope Separators and Techniques Related to their Applications, December 2–7, 2012 at Matsue, Japan, pp. 717–727. ISSN: 0168-583X. doi: <http://dx.doi.org/10.1016/j.nimb.2013.08.050>.

[92] K. Kimura et al. *High-rate particle identification of high-energy heavy ions using a tilted electrode gas ionisation chamber*. In: *Nuclear Instruments and Methods in Physics Research Section A: Accelerators, Spectrometers, Detectors and Associated Equipment* 538.1 (2005), pp. 608–614. ISSN: 0168-9002. doi: <http://dx.doi.org/10.1016/j.nima.2004.08.100>.

[93] Callum Shand. *Shell Evolution beyond N=50 and Z=28: Spectroscopy of  $^{81-84}\text{Zn}$* . PhD thesis. University of Surrey, 2016.

[94] Liliana Cortés. *Inelastic Scattering of Ni and Zn Isotopes off a proton target*. PhD thesis. Technische Universität Darmstadt, 2016.

[95] A. Obertelli et al. *MINOS: A vertex tracker coupled to a thick liquid-hydrogen target for in-beam spectroscopy of exotic nuclei*. In: *Eur. Phys. J. A* 50 (2014), p. 8.

[96] P. Doornenbal. *In-beam gamma-ray spectroscopy at the RIBF*. In: *Prog. Theor. Exp. Phys.* (2012), p. 03C004.

[97] C. Santamaria et al. *Extension of the N = 40 island of inversion towards N = 50: Spectroscopy of  $^{66}\text{Cr}$ ,  $^{70,72}\text{Fe}$* . In: *Phys. Rev. Lett.* 115 (2015), p. 192501.

[98] [http://www.xia.com/Manuals/DGF\\_UserManual.pdf](http://www.xia.com/Manuals/DGF_UserManual.pdf). Official Website.

[99] <http://www.caen.it/csite/ProductList.jsp?parent6&Type=product>. Official Website.

---

[100] IAEA. *Update of X-rays and Gamma Ray Decay Data Standards for Detector Calibrations and Other Applications*. Tech. rep. International Atomic Energy Agency, 2007.

[101] D.C. Radford. *Radware FA.Q version 0.02 - Notes on the use of the program gf3*. Tech. rep. Physics Division - Oak Ridge National Laboratory, 2000.

[102] R. Anholt et al. *Atomic collisions with relativistic heavy-ions. VI. Radiative processes*. In: *Physical Review A* 33 (1986), p. 4.

[103] Gertrude Scharff-Goldhaber. *Excited States of Even-Even Nuclei*. In: *Phys. Rev.* 90 (4 May 1953), pp. 587–602. doi: [10.1103/PhysRev.90.587](https://doi.org/10.1103/PhysRev.90.587).

[104] D. Kameda et al. *Observation of new microsecond isomers among fission products from in-flight fission of 345 MeV/nucleon  $^{238}\text{U}$* . In: *Phys. Rev. C* 86 (5 Nov. 2012), p. 054319. doi: [10.1103/PhysRevC.86.054319](https://doi.org/10.1103/PhysRevC.86.054319).

[105] P. Doornenbal et al. *Lifetime effects for high-resolution gamma-ray spectroscopy at relativistic energies and their implications for the RISING spectrometer*. In: *Nuclear Instruments and Methods in Physics Research Section A: Accelerators, Spectrometers, Detectors and Associated Equipment* 613.2 (2010), pp. 218–225. issn: 0168-9002. doi: <https://doi.org/10.1016/j.nima.2009.11.017>.

[106] M. Dasgupta et al. *Yrast isomers, multi-quasiparticle states and blocking in  $^{176}\text{Ta}$  and  $^{177}\text{Ta}$* . In: *Physics Letters B* 328.1 (1994), pp. 16–21. issn: 0370-2693. doi: [https://doi.org/10.1016/0370-2693\(94\)90421-9](https://doi.org/10.1016/0370-2693(94)90421-9).

[107] P. M. Walker. private communication.

[108] M. Borrajo, T.R. Rodriguez and J.L. Egido. *Symmetry conserving configuration mixing method with cranked states*. In: *Physics Letters B* 746 (2015), pp. 341–346.

[109] <https://web-docs.gsi.de/~wolle/TELEKOLLEG/KERN/index-s.html>. Website.

[110] T.R. Rodríguez. private communication.



---

## Scientific Production during Doctoral studies

---

### Publications in preparation

- Evidence of oblate shape-transition between neutron-rich  $^{92,94}\text{Se}$ . C. Lizarazo, P.-A. Söderström, V. Werner, N. Pietralla, et al.
- Simulated characteristics of the DEGAS  $\gamma$ -detector array. G.S. Li, C. Lizarazo, J. Gerl, N. Pietralla et al. *Submitted to Nuclear Inst. and Methods in Physics Research, A*.
- Isomer spectroscopy of  $^{92,94}\text{Se}$  at the SEASTAR 2015 experiment. C. Lizarazo P.-A. Söderström, V. Werner, N. Pietralla, et al. RIKEN Accelerator Progress Report 2017.

### Technical Reports

- Geant4 Simulations of the novel  $\gamma$ -ray detector array DEGAS. C. Lizarazo, G. Li et al. GSI Scientific Report 2016. [DOI:10.15120/GR-2017-1].
- Shielding and compton suppression capabilities of the EUROBALL BGO back-catchers. C. Lizarazo, G. Li et al. GSI Scientific Report 2014. [10.15120/GR-2015-1-MU-NUSTAR-GS-07].

### Publications as co-author

- Fast-timing lifetime measurement of  $^{152}\text{Gd}$ . J. Wiederhold et al. Phys. Rev. C 94, 044302 (2016) - Published 3 October 2016
- Role of the  $\Delta$  Resonance in the Population of a Four-Nucleon State in the  $^{56}\text{Fe} \rightarrow ^{54}\text{Fe}$  Reaction at Relativistic Energies. Zs. Podolyák et al. Phys. Rev. Lett. 117, 222302 (2016) - Published 23 November 2016
- Are There Signatures of Harmonic Oscillator Shells Far from Stability? First Spectroscopy of  $^{110}\text{Zr}$  N. Paul et al. Phys. Rev. Lett. 118, 032501 (2017) - Published 18 January 2017.
- $^{96}_{36}\text{Kr}$ -Low-Z Boundary of the Island of Deformation at N=60. J. Dudouet et al. Phys. Rev. Lett. 118, 162501 (2017) - Published 17 April 2017.
- Low-lying structure and shape evolution in neutron-rich Se isotopes. S. Chen et al. Phys. Rev. C 95, 041302(R) (2017) - Published 27 April 2017
- Shape Evolution in Neutron-Rich Krypton Isotopes Beyond N=60: First Spectroscopy of  $^{98,100}\text{Kr}$ . F. Flavigny et al. Phys. Rev. Lett. 118, 242501 (2017) - Published 14 June 2017

---

- Triaxiality of neutron-rich  $^{84,86,88}\text{Ge}$  from low-energy nuclear spectra. M. Lettmann et al. Phys. Rev. C 96, 011301(R) (2017) - Published 5 July 2017.
- Shell evolution beyond  $Z = 28$  and  $N = 50$ : Spectroscopy of  $^{81,82,83,84}\text{Zn}$ . C. M. Shand et al. Phys. Lett. B. 773, 492-497 - Published 10 October 2017.

#### **Scientific events attended with oral presentations**

- 2nd Workshop of the Nuclear Spectroscopy Instrumentation Network of EN-SAR2 (NUSPIN), Darmstadt, Germany. 06.2017.
- 81 Jahrestagung der Deutsche Physikalische Gesellschaft, Münster, Germany. 03.2017.
- 5th Sunflower Workshop, Hong-Kong, China. 09.2016.
- 8th Workshop on Quantum Phase Transitions in Nuclei and Many-Body Systems, Prague, Czech Republic. 06.2016.
- Annual conference of the 'Nuclear Structure, Astrophysics and Reactions Collaboration (NUSTAR Week), Warsaw, Poland. 10.2015.

---

## Personal Information

---

### Basic Information

Full Name: Cesar Yesid Lizarazo Sabogal

Date of Birth: 17.08.1989

Place of Birth: Bogotá D.C. - Colombia

Address: Große Eschenheimerstraße, 41, 60313 Frankfurt am Main

Email: cesarliz10@gmail.com.

### Education Background

- **PhD, Physics.** Technische Universität Darmstadt, Germany. 02.2014 - 01.2018.
- **MSc, Physics.** Universidad Nacional de Colombia, Colombia. 02.2012 - 01.2014. Marks: 4.7/5.0 (94%)
- **Summer school on Nuclear Physics.** Universidade de São Paulo, Brazil. 01.2012 - 02.2012.
- **BSc, Physics.** Universidad Nacional de Colombia, Colombia. 02.2006 - 11.2011. Marks: 4.0/5.0 (80%).